NAVAL POSTGRADUATE SCHOOL

MONTEREY, CALIFORNIA

THESIS

PROTOTYPING OF AN OPEN-ARCHITECTURE CMG SYSTEM

by

Kerri L. Ackman

December 2012

Co-Thesis Advisors: Mark Karpenko
I. M Ross

Approved for public release; distribution is unlimited

THIS PAGE INTENTIONALLY LEFT BLANK

REPORT DOCUMENTATION PAGE			Form Approved OMB No. 0704–0188
Public reporting burden for this collection of information is estimated to average 1 hour per response, including the time for reviewing instruction, searching existing data sources, gathering and maintaining the data needed, and completing and reviewing the collection of information. Send comments regarding this burden estimate or any other aspect of this collection of information, including suggestions for reducing this burden, to Washington headquarters Services, Directorate for Information Operations and Reports, 1215 Jefferson Davis Highway, Suite 1204, Arlington, VA 22202–4302, and to the Office of Management and Budget, Paperwork Reduction Project (0704–0188) Washington DC 20503.			
1. AGENCY USE ONLY ***(Leave blank)***	**2. REPORT DATE** December 2012	**3. REPORT TYPE AND DATES COVERED** Master's Thesis	
4. TITLE AND SUBTITLE PROTOTYPING OF AN OPEN-ARCHITECTURE CMG SYSTEM		**5. FUNDING NUMBERS**	
6. AUTHOR(S) Kerri L. Ackman			
7. PERFORMING ORGANIZATION NAME(S) AND ADDRESS(ES) Naval Postgraduate School Monterey, CA 93943–5000		**8. PERFORMING ORGANIZATION REPORT NUMBER**	
9. SPONSORING /MONITORING AGENCY NAME(S) AND ADDRESS(ES) N/A		**10. SPONSORING/MONITORING AGENCY REPORT NUMBER**	
11. SUPPLEMENTARY NOTES The views expressed in this thesis are those of the author and do not reflect the official policy or position of the Department of Defense or the U.S. Government. IRB Protocol number _____N/A_____.			
12a. DISTRIBUTION / AVAILABILITY STATEMENT Approved for public release; distribution is unlimited		**12b. DISTRIBUTION CODE**	

13. ABSTRACT (maximum 200 words)

The purpose of this thesis is to contribute to the development of the next generation of spacecraft attitude control systems by designing and building a prototype open-architecture control moment gyroscope (CMG). The focus is on the CMG mechanism, with emphasis on the momentum wheel assembly. An open-architecture system enables customizable software configuration and allows for future system upgrades, component swapping and integration with other systems. This technical objective was approached through an iterative design process in which several mechanical design configurations were explored prior to the manufacturing of the final prototype. Issues related to the CMG mechanical design, the details of the CMG manufacturing process, including balancing requirements, and integration of the CMG components are discussed. Several experiments illustrate the performance of the CMG prototype. This newly designed CMG prototype will extend the capabilities of the NPS Reconfigurable Spacecraft Autonomy Testbed (R-SAT) simulator and enable demonstrations of advanced attitude control concepts for CMG spacecraft.

14. SUBJECT TERMS CMG, Control Moment Gyroscope, Control Moment Gyro, gimbal, momentum wheel, momentum wheel assembly,			**15. NUMBER OF PAGES** 129
			16. PRICE CODE
17. SECURITY CLASSIFICATION OF REPORT Unclassified	**18. SECURITY CLASSIFICATION OF THIS PAGE** Unclassified	**19. SECURITY CLASSIFICATION OF ABSTRACT** Unclassified	**20. LIMITATION OF ABSTRACT** UU

NSN 7540–01–280–5500

Standard Form 298 (Rev. 2–89)
Prescribed by ANSI Std. 239–18

THIS PAGE INTENTIONALLY LEFT BLANK

Approved for public release; distribution is unlimited

PROTOTYPING OF AN OPEN-ARCHITECTURE CMG SYSTEM

Kerri L. Ackman
Lieutenant, United States Navy
B.S., United States Naval Academy, 2008

Submitted in partial fulfillment of the
requirements for the degree of

MASTER OF SCIENCE IN ASTRONAUTICAL ENGINEERING

from the

NAVAL POSTGRADUATE SCHOOL
December 2012

Author: Kerri L. Ackman

Approved by: Mark Karpenko
Thesis Co-Advisor

I. Michael Ross
Thesis Co-Advisor

Knox T. Millsaps
Chair, Department of Mechanical and Aerospace Engineering

THIS PAGE INTENTIONALLY LEFT BLANK

ABSTRACT

The purpose of this thesis is to contribute to the development of the next generation of spacecraft attitude control systems by designing and building a prototype open-architecture control moment gyroscope (CMG). The focus is on the CMG mechanism, with emphasis on the momentum wheel assembly. An open-architecture system enables customizable software configuration and allows for future system upgrades, component swapping and integration with other systems. This technical objective was approached through an iterative design process in which several mechanical design configurations were explored prior to the manufacturing of the final prototype. Issues related to the CMG mechanical design, the details of the CMG manufacturing process, including balancing requirements, and integration of the CMG components are discussed. Several experiments illustrate the performance of the CMG prototype. This newly designed CMG prototype will extend the capabilities of the NPS Reconfigurable Spacecraft Autonomy Testbed (R-SAT) simulator and enable demonstrations of advanced attitude control concepts for CMG spacecraft.

THIS PAGE INTENTIONALLY LEFT BLANK

TABLE OF CONTENTS

LIST OF FIGURES

LIST OF TABLES

THIS PAGE INTENTIONALLY LEFT BLANK

LIST OF ACRONYMS AND ABBREVIATIONS

ACRONYMS

3-D	three-dimensional
ADCS	attitude determination and control system
ATM	Apollo telescope mount
BEMF	back electromotive force
BDC	brushed DC
BLDC	brushless DC
CAD	computer-aided design
CMG	control moment gyroscope
CNC	computer numerical control
COL	control and optimization laboratories
COTS	commercial-off-the-shelf
DC	direct current
DOF	degree-of-freedom
FOS	factor of safety
ISO	International Organization for Standardization
LEO	low Earth orbit
MOI	moment of inertia
NPS	Naval Postgraduate School
PMSM	permanent magnetic synchronous machine
PSR	perturbed SR inverse steering law
R-SAT	reconfigurable spacecraft autonomy testbed
rpm	revolutions per minute
SPI	singular pseudoinverse
VAC	voltage alternating current
VDC	voltage direct current

SYMBOLS	**DESCRIPTION**
B	Earth's magnetic field (Tesla)
B_L	viscous load friction of the load (Nm/(rad/sec))
B_M	viscous load friction of the motor (Nm/(rad/sec))
B_s	inner damping coeffient of the shaft (Nm/(rad/sec))
C	basic dynamic load rating (N)
d	distance from the unbalance mass to the centerline (in)
D	diameter (in)
F	force (N)
g	gravitation acceleration of Earth (9.81 m/s^2)
G	balance quality grade (Unitless)
F_a	applied axial load (N)

F_r	applied radial load (N)
H	angular momentum (N·m·sec)
h_{cmg}	CMG angular momentum (N·m·sec)
$\bar{H}_{CMG}$	CMG angular momentum vector (N·m·sec)
$\bar{H}_{spacecraft}$	spacecraft angular momentum vector (N·m·sec)
$\dot{\bar{H}}_{total}$	angular momentum rate vector of the combined spacecraft and CMG system (N·m)
i	gimbal motor current (A)
I_{sp}	specific impulse (sec)
J	moment of inertia (kg-m^2)
J_{sc}	spacecraft moment of inertia along its spin axis (kg-m^2)
J_g	moment of inertia for the gimbal along it spin axis (kg-m^2)
$\tilde{J}_{cmg}$	inertia matrix of the CMG (kg-m^2)
J_L	load inertia (kg-m^2)
J_m	motor rotor inertia (kg-m^2)
J_p	polar moment of inertia (kg-m^2)
$\bar{J}_{spacecraft}$	inertia matrix of the main body of the spacecraft (kg-m^2)
K_T	ratio of applied axial load to basic dynamic load rating (Unitless)
K_s	shaft elasticity (Nm/rad)
L_s	length of shaft (mm)
L_{10}	basic rated life (in millions of revolutions)
m	mass (kg)
$m_{unbalance}$	unbalance mass (g)
m_{rotor}	rotor mass (kg)
M	magnetic moment (A·m^2)
n	maximum angular velocity for which the object is rotated (rpm)
P	equivalent dynamic bearing load (N)
p	power (W)
q	exponent in life equation (Unitless)
Q	shear modulus (GPa)
r	radius (mm)
R	gear ratio (Unitless)
R_{Earth}	radius from the center of the Earth to the spacecraft (km)

R^2	coefficient of determination (Unitless)
T	Torque (Nm)
T_M	motor torque (Nm)
T_L	load torque (Nm)
T_s	torque transmitted through the shaft (Nm)
T_{sb}	torque removed from the system due to backlash (Nm)
T_{sc}	nominal transmitted shaft torque (Nm)
$\vec{T}_{ext}$	external torque vector (Nm)
t_f	final time (sec)
U_{per}	permissible residual unbalance (gram-inches)
u	control variable (Units depend on choice of control variable)
$\vec{u}$	internal control torque (Nm)
W_{lbs}	weight of the object being balanced (lbs)
X	radial load factor (Unitless)
Y	axial load factor (Unitless)
Y_2	duplex bearing load factor (Unitless)
α	angle between the applied load and the rolling element (deg)
Ω	spin rate CMG wheel (deg/sec)
$\dot{\delta}$	gimbal rate (deg/sec)
δ	gimbal angle (deg)
δ_v	gimbal rate (deg/sec)
$\dot{\theta}$	rotation rate of the reference axis (deg/sec)
θ_D , $\dot{\theta}_D$	motor shaft displacement angle (deg), angular velocity (deg/sec)
$\dot{\theta}_L$, $\ddot{\theta}_L$	angular velocity of the load (deg/sec), angular acceleration (deg/sec^2)
$\dot{\theta}_M$, $\ddot{\theta}_M$	motor rotor angular velocity(deg/sec), angular acceleration (deg/sec^2)
θ_{sc} , $\dot{\theta}_{sc}$	spacecraft attitude angle (deg), angular velocity (deg/sec),
ϕ	maximum twist angle in radians (deg)
$\dot{\phi}$	rotation rate of the Quad axis (deg/sec)
τ_g	gimbal torque (Nm)

ω	angular velocity (deg/sec)
ω_{sc} , $\dot{\omega}_{sc}$	spacecraft body rate (deg/sec), acceleration (deg/sec^2)
$\vec{\omega}_{cmg}$	gimbal angular velocity vector (deg/sec)
$\vec{\omega}_{spacecraft}$	angular velocity vector of the main body of the spacecraft (deg/sec)
Ψ	shaft elasticity ((Nm/rad))
$x(\bullet)$	state function or trajectory in state space
$u(\bullet)$	control function or trajectory

Units

Hz	hertz
deg	degree
A	ampere
arc sec	arcsecond
mm	millimeter
N	Newton
in	inch
kg	kilogram
km	kilometer
rad	radians
lbs	pounds
lbsf	pounds force
m	meter
Pa	Pascal
sec	second
V	volts
W	watts

ACKNOWLEDGMENTS

First and foremost, I need to thank the Naval Postgraduate School and my thesis advisors Dr. Mark Karpenko and Dr. I. M. Ross for allowing me to conduct this thesis. Without continuous mentorship, guidance and patience of Dr. Karpenko none of this would have been possible. I have learned a lot over the past 18 months and I found this project to be both challenging and rewarding.

Although I am receiving my master's degree in astronautical engineering, my thesis work exposed me to numerous different types of engineering: control engineering, mechanical engineering, material engineering, electrical engineering, manufacturing engineering, design engineering and systems engineering. I am honored that the Naval Postgraduate School, the Optimal Control Laboratories, Dr. Karpenko and Dr. Ross gave me this opportunity to complete this thesis work and I am extremely grateful.

To my dear friend, Rachel Silvestrini, thank you for spending countless hours helping me perfect my thesis writing skills. To all of the employees at Inter-City Manufacturing in Sand City, CA, especially Doug Sr., Doug Jr. and Karen, for all of the assistance over the past year of my thesis. Thank you to Dan Sakoda for helping me learn how to use the CAD modeling software and printing my the 3-D plastic components. I would like to thank George Cox at Cox & Sprague Machinists for sharing his knowledge and expertise with me and allowing me to observe the balancing of my components. To Dan Chisholm, thank you for helping me order all of parts and for your mentorship. I would like to also thank David Mann for assisting me during my thesis work.

To the Williams Family, thank you for always making me feel at home in Monterey and welcoming me into your family. To my boyfriend, Chris, thank you very much for your continuous words of encouragement, patience and supporting me throughout this journey. To my family, thank you for supporting me over the past 11 years in the military and through my time at NPS. This list is not inclusive and I am sure that I am omitting some people, but it was not done intentionally. I sincerely appreciate all of the help that I received from everyone and I could have never done this alone.

THIS PAGE INTENTIONALLY LEFT BLANK

I. INTRODUCTION

A. BACKGROUND

Although humans have been fascinated with space since the 2nd century, it was not until October 4, 1957 that both aeronautical and rocket propulsion technologies were advanced enough to successfully launch Sputnik I into space [1]. Not long after, the United States began launching a series of satellites beginning with Explorer I, whose onboard scientific equipment allowed researchers their first glimpse at the space environment. The onboard scientific equipment measured the level of charged particles, radiation, micrometeorites and perturbations in the geomagnetic field [2], [3], [4], [5], [6]. The data obtained by the scientific equipment, showed that all of the spacecraft experienced some kind of adverse effect after being exposed to the space environment. After many years of research, scientists have divided the space environment into nine categories: the neutral thermosphere, thermal environment, plasma, meteoroids and orbital debris, solar environment, ionizing radiation, geomagnetic field, gravitation field and the mesosphere [7]. In addition to environmental effects, spacecraft also experience disturbances and uncertainties caused by appendages, inaccuracies in center of gravity approximation and mass properties, thruster misalignment, rotating machinery, dynamics of flexible bodies and liquid sloshing [8].

In order to conduct maneuvers and minimize the effects of external and internal disturbances, most spacecraft are equipped with an attitude determination and control systems (ADCS) [9]. An ADCS consists of multiple components which include sensors (e.g. GPS, star trackers, sun sensors, and rate gyros) and actuators (e.g., thrusters, magnetic torque rods, reaction/momentum wheels or control moment gyroscopes.) An ADCS also needs software control logic to coordinate all of the sensor and actuator functions. The components are chosen by an attitude determination control engineer who uses performance parameters such as accuracy, weight and power in order to choose components; these performance parameters are usually set by spacecraft's payload or mission requirements. Accuracy is the measure of how well the spacecraft attitude can be controlled with respect to a commanded direction, weight is the value of additional mass

the ADCS will add to the spacecraft, and power is the additional power draw the ADCS requires to operate [8]. Table 1 shows the accuracy, weight and power performance parameters for common ADCS actuators.

Actuator	Pointing Accuracy	Weight	Power	Output Torque
Chemical Thrusters	±0.1 to ±5 deg	Variable	Variable⋆	0.5 to 9,000 N*
Magnetic Torque Rods	±5 deg	0.4 to 50 kg	0.6 to 16 W	$4.5X10^{-5}$ to 0.18 Nm
Reaction Wheels/ Momentum Wheels	±0.001 to ±1 deg	2 to 20 kg	10 to 110 W	0.01 to 1 Nm
CMGs	±0.001 to ±1 deg	>10 kg	90 to 150 W	25 to 500 Nm
*multiple by moment arm to obtain torque			⋆Expendable Propellant Required	

Table 1. Typical performance of typical ADCS actuators (After [8])

Prior to selecting the final components for the ADCS, the control engineer will perform a trade study using all of the performance parameters described as well as evaluating the pros and cons. In order to highlight the importance of CMGs with respect to spacecraft control and reiterating the motivation behind this thesis, this section compares four common ADCS actuators: chemical thruster, magnetic torque rod, reaction and momentum wheel, and control moment gyroscope (CMG).

A chemical thruster is one common actuator system for space applications. A chemical thruster creates a high control impulse torque by expelling propellant, which allows for large instantaneous torques [8]. There are several different classes of chemical thrusters and they are classified according to the physical state of the propellant [10]. The most commonly used types of chemical propellant thrusters are liquid, solid, gaseous, and hybrid. All chemical thrusters require the same combustion reaction in order to produce thrust, but they each have very different performance characteristics. The key parameter that is used to determine a thruster's performance is the specific impulse (I_{sp}), which is a measure of total impulse per unit weight of propellant [10]. The performance of a thruster

increases with an increase in the I_{sp}. Typical I_{sp} values range from 30 seconds for a cold gas thruster to 340 seconds for a hybrid thruster [8].

Although each type of chemical thruster has its own performance characteristics, they all require expendable propellant which increases the initial wet mass of the spacecraft and the overall cost of the mission. A thruster also contaminates surfaces and can damage sensitive equipment with its plumes [8]. Despite these disadvantages, a high instantaneous torque is needed for certain spacecraft missions, such as interplanetary and deep space missions, so the tradeoff can be acceptable.

A magnetic torque rod is another kind of actuator that uses magnetic coils or electromagnetics and the Earth's magnetic field to produce torque and electrical current to operate [8],[9]. A magnetic torque rod uses electrical current to operate and produces a resultant torque perpendicular to the Earth's magnetic field (see Figure 1) [9]. Because of this, multiple torque rods are required for three axis attitude control.

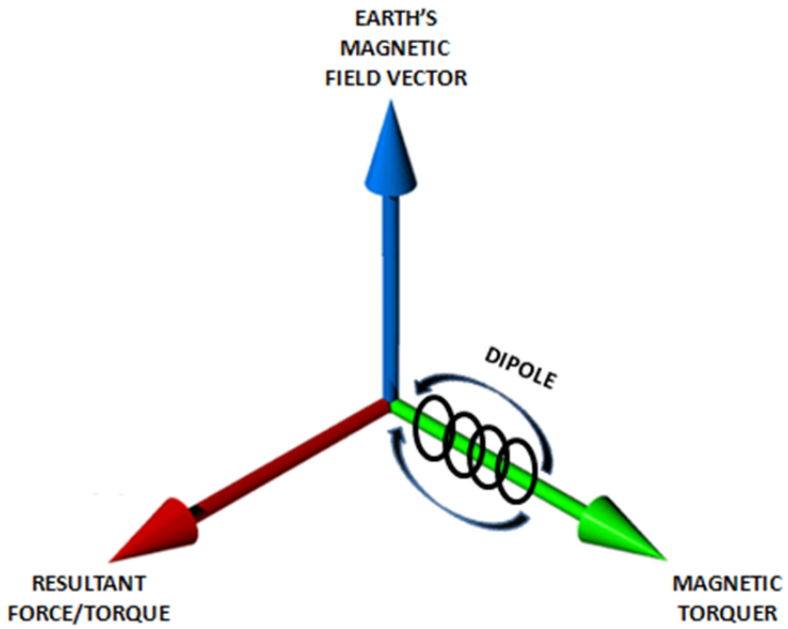

Figure 1. Torque output direction of a magnetic torque rod

Magnetic torque rods are also limited by the region of space where they are applicable; they can only be utilized on missions well below synchronous orbit (< 35,000 km) because the strength of Earth's magnetic field decreases as a function distance from the center of the Earth according to

$$B = 2M \Big/ R_{Earth}^{\ 3} \tag{1.1}$$

where B is Earth's magnetic field, M represents the magnetic moment of the Earth and R_{Earth} is the radius from the center of the Earth to the spacecraft [8], [11]. Because of their characteristics, magnetic torque rods are primarily used in low Earth orbit (LEO) to correct for small periodic disturbances and to desaturate momentum exchange devices.

Momentum exchange devices are actuators that create momentum by rotating a mass and are governed by the Law of Conservation of Angular Momentum; which states that the total momentum of a system must be conserved in the absence of an external torque. The angular momentum for a device can be calculated using:

$$H = J\omega \tag{1.2}$$

where H is the angular momentum, ω is the angular spin rate and J is the moment of inertia (MOI) of the spinning rotor. For example, if a momentum exchange device creates momentum in one direction, a spacecraft must conserve momentum by moving in the opposite direction. Momentum exchange devices are highly desirable because they allow for continuous control, enable reversible momentum exchange, and do not require any propellant to operate [12]. For these reasons, they are commonly used for large spacecraft with stringent requirements on accuracy, long duration missions and large slew maneuvers [12]. The most common momentum exchange devices used in space applications are reaction and momentum wheels and CMGs.

Reaction and momentum wheels are rotating masses that are permanently oriented along a fixed axis and provide a low torque to the spacecraft. Reaction wheels have the ability to change spin rate and direction; this allows them to generate any desired torque within limits. In contrast to a reaction wheel, a momentum wheel rotates at a constant speed in only one direction and is intended to generate gyroscopic rigidity about a given axis, not for attitude control.

In the presence of disturbances, momentum exchange devices continue to buildup stored momentum until they reach a maximum capacity and become saturated. Once this occurs, the excess momentum must be released through momentum dumping, also known as desaturation. Desaturation is the process of applying an external torque to the system in order to force the speed of momentum wheel to zero or another desired value [8], [12]. Both reaction and momentum wheels are an excellent devices for controlling the cyclic torques created by the space environment and to add rigidity or gyroscopic stiffness to an axis. This is why they are often selected when a rapid slewing and high output torques are not mission requirements [13].

A CMG is a constant speed momentum wheel mounted on a pivoted support structure also known as a gimbal [14], [15]. Since the CMG wheel runs at a constant speed, it can be optimized based on the driving motor parameters. The gimbal allows the CMG's momentum vector to change direction, thus inducing an exchange of momentum between the CMG and the spacecraft along more than one axis [12]. CMGs create high output torques by facilitating torque multiplication with minimum power usage. Similar to a reaction wheel, however, they are limited by saturation speed and desaturation requirements [16], [13], [15], [17]. CMGs have become the actuator of choice for large spacecraft which may require fast slew maneuvers or precise pointing accuracy [17], [18]. The principle dynamics and mathematics for a CMG are discussed in further detail later in this thesis.

B. CONTROL MOMENT GYROSCOPES

By the mid 1960's CMGs had already been used in numerous space applications and were expected to have a bright future due to the growing demand for spacecraft with long duration missions and precision attitude control [17], [19]. In 1967, O'Connor and Morine examined the dynamics of a CMG and its feasibility for use as a primary actuator for spacecraft vehicle control. They noted that CMGs had better efficiency, larger maximum moments and increased dynamic range of moments, better bandwidth characteristics, and a more linear approach toward saturation than many other actuators. CMGs, however, have additional cross coupling terms which requires a more complex

control laws [12]. Also in 1967, CMGs were selected as the attitude control actuator for the Apollo Telescope Mount (ATM) Skylab.

Since Apollo was the first manned United States space station, every precaution was taken to ensure that the CMGs would be successful. By 1969, Klye and Keckler performed a real-time digital computer-hardware simulation on a full-scale CMG cluster system prototype and discovered a system-related problem in which the spacecraft would lose control; today we know this issue as CMG singularity [20]. They also noted that there were problems with gimbal position feedback and recommended that future gimbal designs should have minimal backlash and high stiffness [20]. Their report concluded with a suggested list of follow-on simulations. Further tests and simulations were conducted by numerous scientists including scientists at NASA Langley Research Center [21], [22].

In 1970, Auclair and Wells studied the performance, reliability and life of multiple CMGs in order to synthesize the designs of the then current state-of-the-art CMGs [13]. Their work was aimed primarily at helping the control engineer to select the appropriate CMG for an ADCS and not as a design document. In 1973 Rybak et al., Osborne and Liden focused on improving CMG pointing accuracy [23], [24], [25]. Subsequently in 1974, the Bendix Corporation prepared a summary report of advanced CMG detailing lessoned learned from the Skylab ATM CMG. The report contained detailed suggestions improvements for almost all of the subassemblies of the CMG, to include: inner and outer gimbal assemblies, frame, actuator pivot assemblies, electronics, and wheel and gimbal control [26]. The report highlights the complications that were encountered while designing the CMG prototype for the Skylab ATM [26]. In 1976, Colburn and White emphasis was on the importance of was on improving steering logic and control laws for CMGs [27].

In the 1980s, space vehicles were growing larger, required higher torques, more attitude control authority and momentum capability. With this trend in mind, researchers began to focus on developing an improved momentum management scheme for the space station [28]. Shortly after, scientists at NASA Marshall Space Flight Center recognized that technologies needed to be developed to support large spacecraft structures such as

the Space Station [29]. In support of this effort they decided design, fabricate and test a CMG using existing technologies and lessoned learned from the ATM Skylab mission for their prototype [29]. By 1989, scientists began to explore alternative ways of mounting CMGs; Kito, Kanki and Ishii examined the possibility of magnetically suspending a single- gimbal CMG and their work showed satisfactory results [30].

In the 1990s, Yang et al. recognized that large structures, such as the spacecraft, are subject to vibrations and they created a controller that would help suppress vibrations during a constant slew maneuver. Their analytical and numerical results showed that they controller was very effective [31]. Subsequently in 1997, Heiberg and Bailey again highlighted the importance of improving CMG pointing precision of an agile spacecraft examining nonlinear disturbance control and discussing different CMG configurations with respect to singularity and momentum exchange [32].

In 2000, Heiberg's research focused primarily on finding a proper way to model a CMG to include the loading at the mechanical interface, angular rotation of the spacecraft couples and how his modeling approach can be used on a CMG array [16]. Subsequently. Lappas and Wie and Kurokawa attempted to improve steering logic and control laws for CMGs; their work highlights the effects of singularities on a CMG system [14], [33]. Lappas and Wie suggest that a mechanical gimbal angle constraint be added to a CMG to prevent it from reaching a singularity [14]. Kurokawa on the other hand, argues that CMG singularities can be avoided using steering laws and presents a few different variations [33].

C. NPS R-SAT

The rich history of CMG related research demonstrates that CMGs have been extensively studied for over six decades and that advances in ADCS technologies have helped to further space exploration. However, it also indicated that there is still a lot to learn about building, developing and controlling CMGs.

The Control and Optimization Laboratories (COL) at the Naval Postgraduate School (NPS) is continuing this research by examining new ways of looking at old problems and exploring how CMG technology can be improved. In 2009, the COL

purchased a 3 degree-of-freedom (DOF) satellite simulator from Andrews Space (see Figure 2); which is being reworked and redesigned to a Reconfigurable Spacecraft Autonomy Testbed (R-SAT).

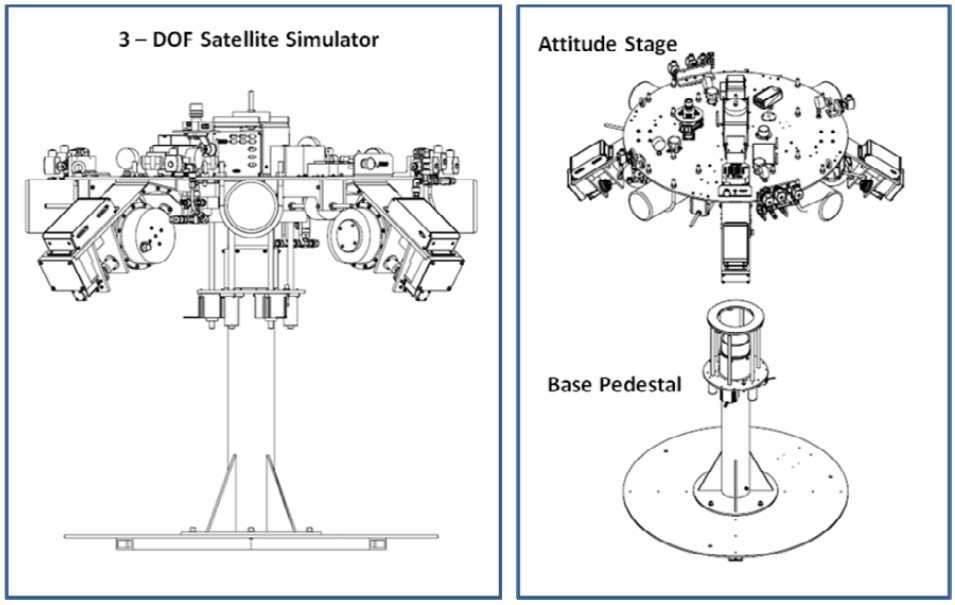

Figure 2. Andrews 3 DOF satellite simulator illustration (From [34])

The Andrews simulator was intended to allow students and researchers to validate and test spacecraft control algorithms on actual hardware. Even though the simulator has become an invaluable asset to advancing research it is limited by its closed-architectural design. The lack of ability to reconfigure the simulator limits the ability of NPS researchers to conduct high level research because it does not allow for upgrades to components and/or software, makes maintenance and repairs virtually impossible and does not allow for easy interoperability with other systems.

Although the simulator has its limitations, it became the baseline configuration from which to design the next generation R-SAT simulator. The new simulator will have improved modules, which includes an ADCS module, a mass balancing module and improved software/hardware integration module. The purpose of this thesis is to contribute to the development of the next generation R-SAT by designing and building an open-architecture CMG. An open-architecture system enables customizable software

configuration and allows for future system upgrades, component swapping and integration with other systems. Open-architecture systems are often built using commercial-off-the-shelf (COTS) components. COTS components can save a program time and money because they have already been used in an applications which reduces the requirement for testing. In addition, COTS components are usually built in larger quantities than a test article which reduces the overall cost. COTS components are also usually more readily available which reduces the time between purchasing and shipment [35].

D. OBJECTIVES AND SCOPE

The purpose of this thesis is to contribute to the development of the next generation of spacecraft attitude control systems by designing and building a prototype open-architecture control moment gyroscope (CMG). The focus is on the CMG mechanism, with emphasis on the momentum wheel assembly. An open-architecture system enables customizable software configuration and allows for future system upgrades, component swapping and integration with other systems. This technical objective was approached through an iterative design process in which several mechanical design configurations were explored prior to the manufacturing of the final prototype.

Chapter II describes the mathematical principles for a rigid spacecraft with CMGs. It also briefs describes CMG mounting configurations. Chapter III describes issues related to the CMG mechanical design, the momentum wheel assembly requirements and design process utilized during this thesis. Chapter IV describes the gimbal assembly requirements, the design process developed during this thesis and issues related to gimbal performance, such as backlash.

Chapter V describes the details of the CMG manufacturing process, including balancing requirements, and integration of the CMG components. Chapter VI discusses the testing and experiments completed on the CMG and the results. Chapter VII presents some final remarks, challenges faced during this thesis and outlines possible areas future work.

THIS PAGE INTENTIONALLY LEFT BLANK

II. MATHEMATICAL MODEL FOR A RIGID SPACECRAFT WITH CMGS

This chapter will discuss the mathematical model and attitude dynamics for rigid spacecraft with CMGs. The equations in this chapter were used to derive the simplified double integrator spacecraft problem discussed in Chapter IV. This chapter also contains a brief discussion of CMG steering logic and the factors that affect the control of a spacecraft with CMGs. All of the CMG equations in this chapter are based on the coordinates and notation shown in Figure 3.

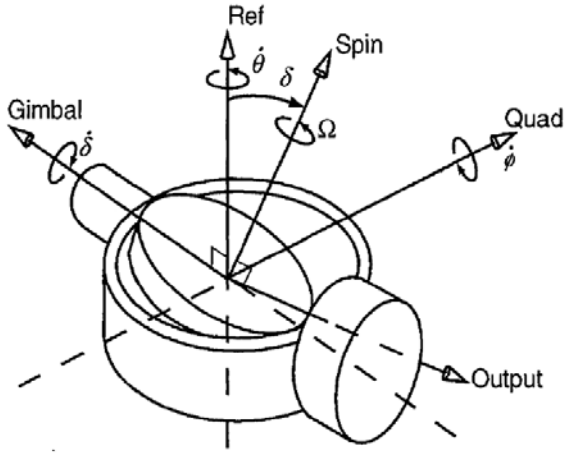

Figure 3. CMG coordinates and notation (After [16])

The CMG in Figure 3 has a total of five important axes: Gimbal, Ref, Spin, Quad, and Output. The Gimbal axis is the axis around which the CMG is rotated. The Ref axis represents the reference spin axis for which the gimbal angle is equal to zero. The Spin axis represents the new spin axis after the gimbal has been rotated by an amount equal to δ . The Output axis is the axis for which the output torque will act. The output torque direction is a function of the gimbal angle rotation and can be in the positive or negative direction along the output axis. The Quad axis is the quadrature formed by taking the cross product of the Gimbal and Ref axes [16].

A. MATHEMATICAL MODELING AND ATTITUDE DYANMICS

The rotational equation of motion for a rigid spacecraft with external torques can be written as:

$$\dot{\vec{H}}_{total} + \vec{\omega}_{spacecraft} \times \vec{H}_{total} = \vec{T}_{ext} \tag{2.1}$$

where $\dot{\vec{H}}_{total}$ is the angular momentum rate vector of the total system which includes the main body of the spacecraft and CMGs and external torques, $\vec{\omega}_{spacecraft}$ is the angular velocity vector of the system, $\vec{H}_{total}$ is angular momentum vector for the system and $\vec{T}_{ext}$ is the external torque vector [36]. The total system's angular momentum value $\vec{H}_{system}$ can be written as:

$$\vec{H}_{total} = \vec{H}_{CMG} + \vec{H}_{spacecraft} \tag{1.1}$$

where $\vec{H}_{CMG}$ is the CMG angular momentum vector and $\vec{H}_{spacecraft}$ is the spacecraft angular momentum vector with respect to spacecraft body-fixed frame. The spacecraft angular momentum vector can be written as:

$$\vec{H}_{spacecraft} = \tilde{J}_{spacecraft} \vec{\omega}_{spacecraft} \tag{1.2}$$

where $\tilde{J}_{spacecraft}$ is the inertia matrix of the spacecraft and $\vec{\omega}_{spacecraft}$ is the angular velocity vector of the spacecraft in the body-fixed frame. Combining Equation (2.2) and Equation (2.3), we obtain the total angular momentum of the system:

$$\vec{H}_{system} = \tilde{J}_{spacecraft} \vec{\omega}_{spacecraft} + \vec{H}_{cmg} \tag{1.3}$$

After combining Equation (2.1) and Equation (2.4), the total external torque of the system can be written:

$$\tilde{J}_{spacecraft} \dot{\vec{\omega}}_{spacecraft} + \dot{\vec{H}}_{cmg} + \vec{\omega}_{spacecraft} \times (\tilde{J}_{spacecraft} \vec{\omega}_{spacecraft} + \vec{H}_{cmg}) = \vec{T}_{ext} \tag{1.4}$$

In order to conserve the angular momentum of the system and maintain its current attitude, the left hand side must equal the external torque vector on the right hand side of Equation (2.5). By creating a CMG control torque vector denoted as $\vec{u}$, Equation (2.5) can be written as:

$$\tilde{J}_{spacecraft}\dot{\vec{\omega}}_{spacecraft} + \vec{\omega}_{spacecraft} \times (\tilde{J}_{spacecraft}\vec{\omega}_{spacecraft}) = \vec{T}_{ext} - \vec{u} \qquad (1.5)$$

where $\vec{u} = \dot{\vec{H}}_{cmg} + \vec{\omega}_{spacecraft} \times \vec{H}_{cmg}$, which is the internal control torque generated by the spacecraft CMGs. Each CMG in an array of CMGs can contribute to the production of this desired torque vector by changing the direction of their angular momentum vectors about their spin axes (see Figure 4) [36].

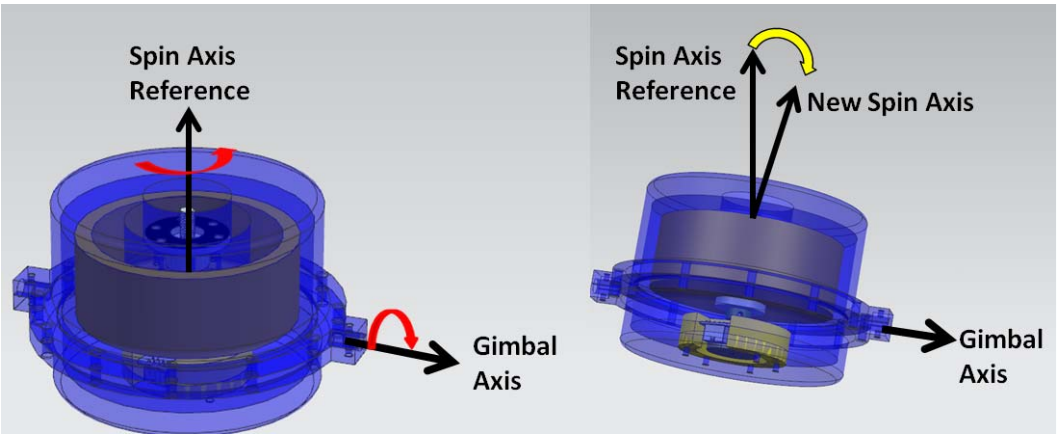

Figure 4. CMG rotation illustration

The output torque of each CMG is defined as a rate of change of angular momentum, where the CMG angular momentum can be calculated in the CMG frame coordinates (reference Figure 3) as:

$$\vec{H}_{CMG} = \tilde{J}_{cmg}\vec{\omega}_{cmg} = \begin{bmatrix} I_{gimbal} & 0 & 0 \\ 0 & I_{spin} & 0 \\ 0 & 0 & I_{ouput} \end{bmatrix} \begin{bmatrix} \dot{\delta} \\ \Omega + \dot{\theta}\cos\delta + \dot{\phi}\sin\delta \\ \dot{\phi}\cos\delta - \dot{\theta}\sin\delta \end{bmatrix} \qquad (2.7)$$

where $\tilde{J}_{cmg}$ is the inertia matrix of the gimbal, $\vec{\omega}_{cmg}$ is the angular velocity vector in the CMG frame, $\dot{\delta}$ is the rotation rate of the gimbal axis or gimbal rate, Ω represents the spin rate CMG wheel, $\dot{\theta}$ is rotation rate of the Ref axis, δ is the gimbal angle and $\dot{\phi}$ is the rotation rate of the Quad axis [16].

B. CMG STEERING LOGIC

There are many approaches to controlling CMGs and the mathematical model derived above. Steering logic for CMGs often depends on the mounting arrangement of the CMGs with respect to the spacecraft, the number of CMGs and the control algorithm used [16],[36]. Due to singularities, momentum desaturation requirements, vast choices in CMG configurations and mounting, there is no industry standard steering logic [33]. In fact there are numerous approaches and methods that are being implemented to control a spacecraft's attitude with CMGs such as singularity avoidance, proportional-plus-integral, time optimal, perturbed SR inverse steering law (PSR) and singular pseudoinverse (SPI) [25], [32], [33],[36].

There are also many CMG mounting choices to include, parallel, skewed and orthogonal mounting [36]. One typical arrangement for a spacecraft is to have four CMGs mounted in a tetrahedral configuration with a skew angle of 54.73 degrees (see Figure 5). This arrangement is quite efficient in the sense that if one the CMGs fails then the three remaining CMGs share the work in more homogeneous way [14], [32].

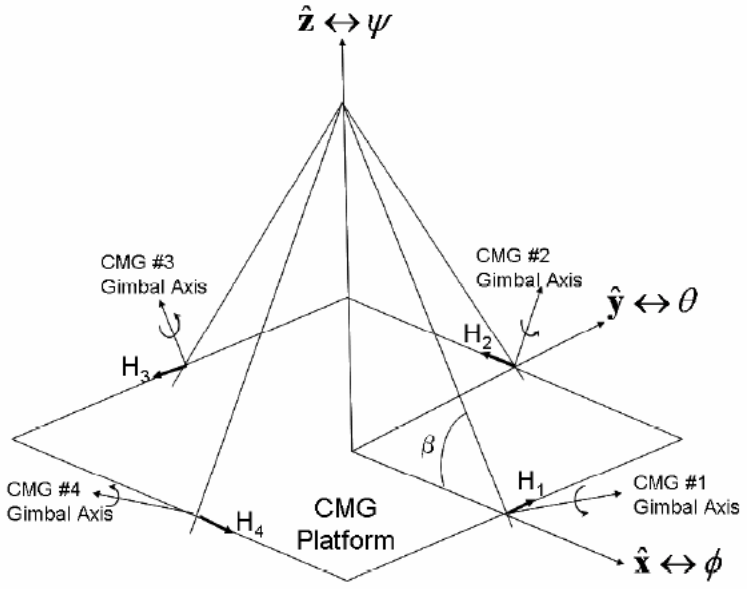

Figure 5. Tetrahedral CMG mounting arrangement (After [32])

In addition to the mounting arrangement choices, CMGs may also be mounted with one-, two- or multiple-DOFs [13]. A double gimbal mounting configuration is shown Figure 6. The two DOF gimbal configuration allows for two axes control. This is accomplished by using two gimbal motors and allowing the momentum wheel assembly to move freely in along two axes [37]. This configuration has inherent redundancy since it has two motors and will be able to control the spacecraft even if one of the motors fails. It also allows for a better distribution of the angular momentum vectors when in working with other CMGs [18]. The addition of the second DOF, however, creates a more complex mechanical system which means there are more components that could fail.

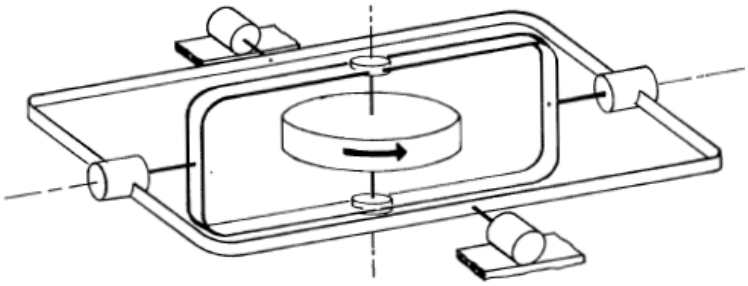

b. Two Degrees of Freedom

Figure 6. Example of a double gimbal CMG mounting configurations (After [37])

The CMG developed in this thesis is a single DOF configuration, also known as a single gimbal CMG. This CMG is a simple design and therefore has fewer moving parts. This makes it is highly desirable to fly in space where it is nearly impossible to performance maintenance or repair a piece of equipment. The one DOF system adds complexity to the CMG system and makes it more challenging to control due to the singularities when CMGs are operated in an array. However, as stated above, there are a variety of different approaches available to overcome this issue.

THIS PAGE INTENTIONALLY LEFT BLANK

III. MOMENTUM WHEEL ASSEMBLY

This chapter discusses the parameters and the mechanical characteristics of the momentum wheel assembly including the design process methodology used to develop the new CMG system. It also describes the momentum wheel assembly design and its components which include: the momentum wheel, the motor, the duplex bearing, the shaft and motor connector and the cases. The development and analysis of the gimbal assembly is discussed in the next chapter.

A. DESIGN PROCESS METHODOLOGY

When engineering design components are coupled they often lead to multiple iterations, this is especially true in a large engineering project, when there is a convergence of many projects or when many features are coupled [38]. In the case of the momentum wheel assembly, all of the components are coupled and making even a small change in one component can cause a ripple effect through the entire assembly, i.e., the casing size, the shaft size, bearing diameter choice. Because of this challenge the momentum wheel assembly was designed using an iterative design methodology (see Figure 7).

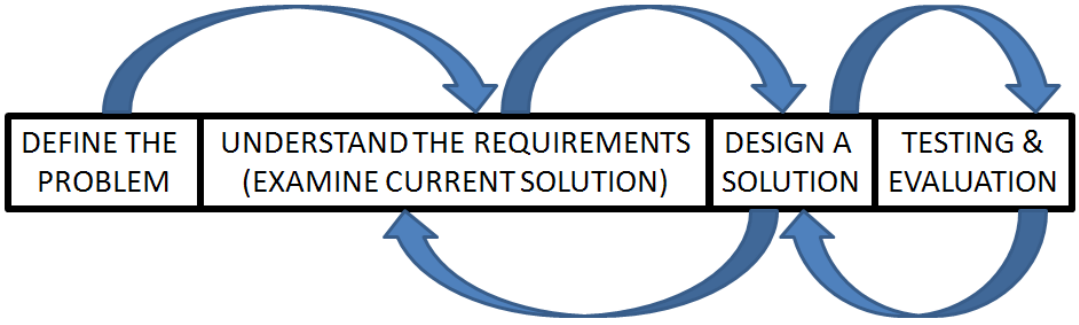

Figure 7. Iterative engineering design process

The iterative engineering design process begins once the problem has been defined. The problem in this thesis is how to design a prototype CMG. The next step in

the design process is to understand the requirements, which can be done by examining the current solution. The requirements for this thesis were derived by examining the current R-SAT specifications and the desired performance parameters. The next step in the engineering design process is to use the lessons learned from the prior phase to create a solution for the defined problem. This is the phase where the CMG prototype was designed. The testing and evaluation phase begins once the design solution is complete. The testing and evaluation phase is where the performance of the CMG prototype was analyzed. If the evaluation results show that the solution does not meet the requirements, then a new solution may need to be designed.

The process followed in Figure 7 resulted in 13 different design configurations. In iterating through the various concepts, some design changes were made because the current design would be impossible to manufacture. Other designs were found to be too difficult to assemble and some that had too many parts and would therefore be hard to maintain or repair. The final design configuration leading to the mechanical prototype is shown in Figure 8.

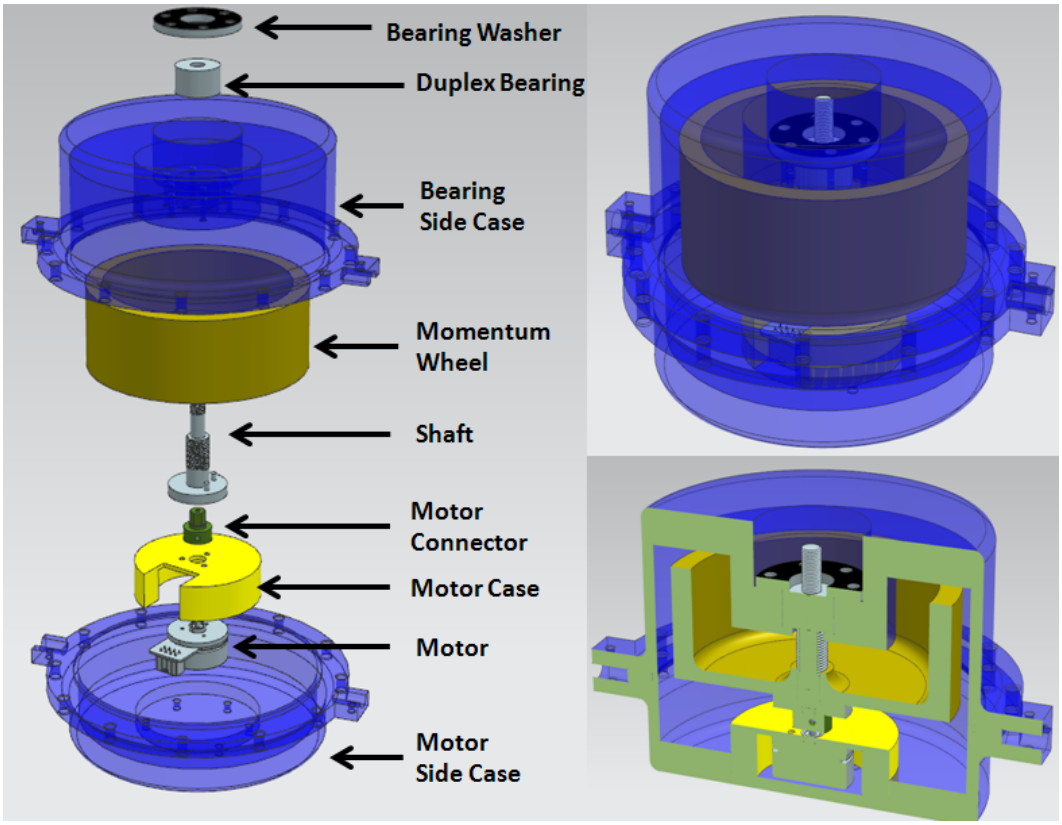

Figure 8. Final prototype momentum wheel assembly

The final prototype design reduced the number of components to 9, allowed for more clearance between components and has various locating registers to ensure precise alignment of the rotating components.

The preliminary design of the prototype momentum wheel assembly began with a close examination of the current R-SAT momentum wheel assembly and each of its components which included: a motor, a momentum wheel, two outer casings, a needle bearing, a shaft, and bearing shaft adapter. The results of the examination were then used as the baseline for the new momentum wheel assembly design. Although not all of the components needed to a be redesigned, the complex coupling of the components required that each component be examined thoroughly. A detailed discussion of the results for each component is provided in the following sections.

The design solution phase began with countless hand drawn paper designs. When a realistic hand drawing was complete, the components, excluding the COTS components

(such as the motor and the duplex bearing), were then designed and modeled using Siemens NX 7.5 computer-aided design (CAD) modeling tool. The CAD modeling tool was also used to create technical drawings which were used during the prototyping and manufacturing process. The 11th design configuration produced an acceptable CAD model which appeared to meet all of the requirements; this design will now be referred to as the 1st prototype. The 1st prototype design is shown in Figure 9 and was comprised of 12 parts. The CAD model was exported to a three dimensional (3-D) printer to produce a plastic model of the momentum wheel assembly. The 3-D printer allowed for a cheap and quick way to test and evaluate the placement, fit and assembly prior to finalizing the design (see Figure 10).

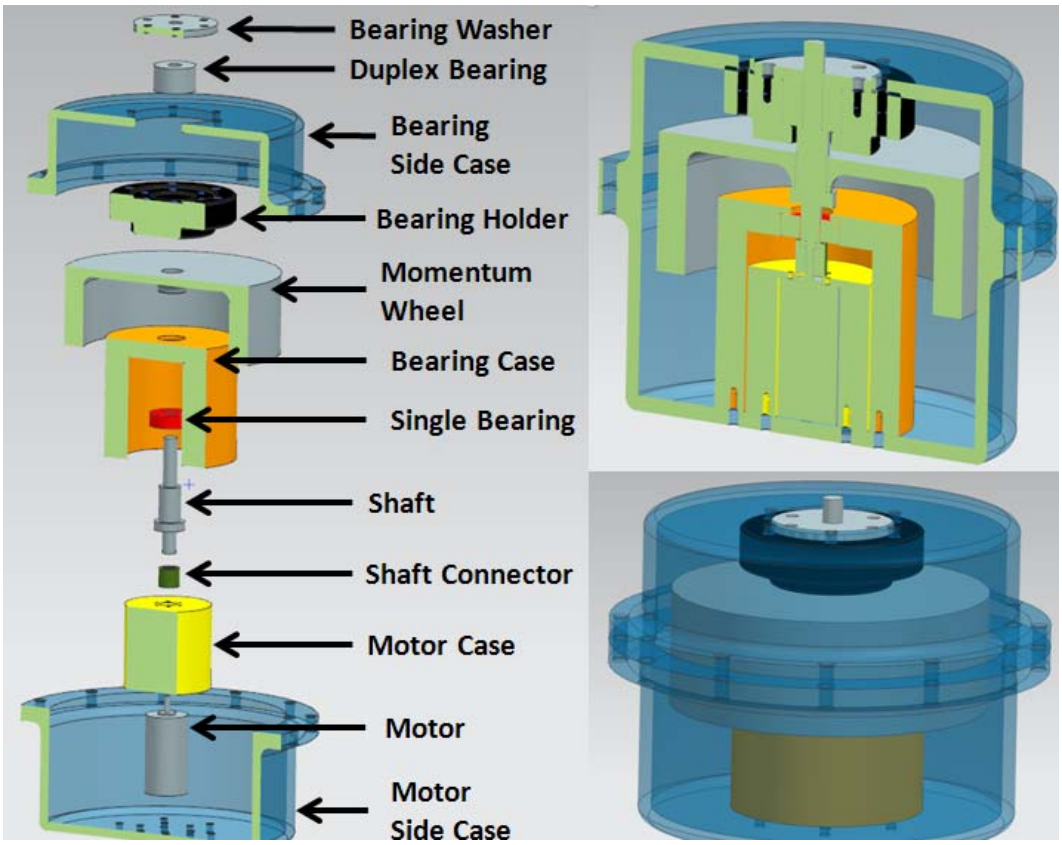

Figure 9. First prototype CAD model

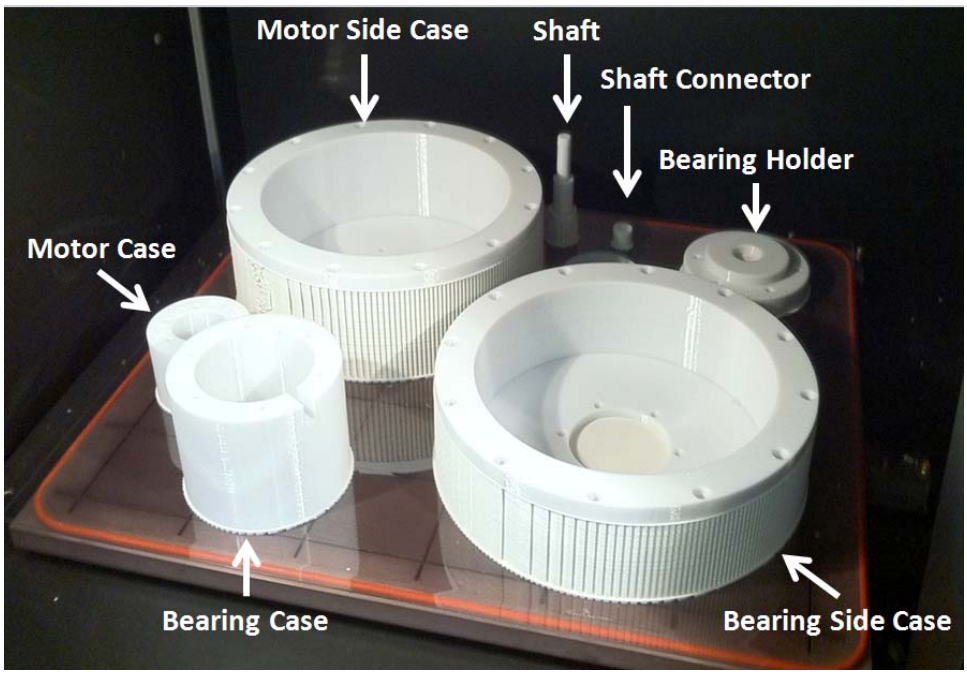

Figure 10. First prototype 3-D printer components

The 3-D model highlighted that the 1st prototype design had two major flaws. The large number of components made it hard to assemble and made it nearly impossible to keep the alignment of the rotating parts accurate. Since the momentum wheel is spinning at a high angular velocity, it is very important that the alignment of all of the components be accurate. Locating registers were added to the design to help keep the components aligned. A locating register creates a space or footprint for the component which allows it to be perfectly placed every time. These changes were applied to the momentum wheel assembly creating the 12th design configuration, which will now be referred to as the 2nd prototype (see Figure 11).

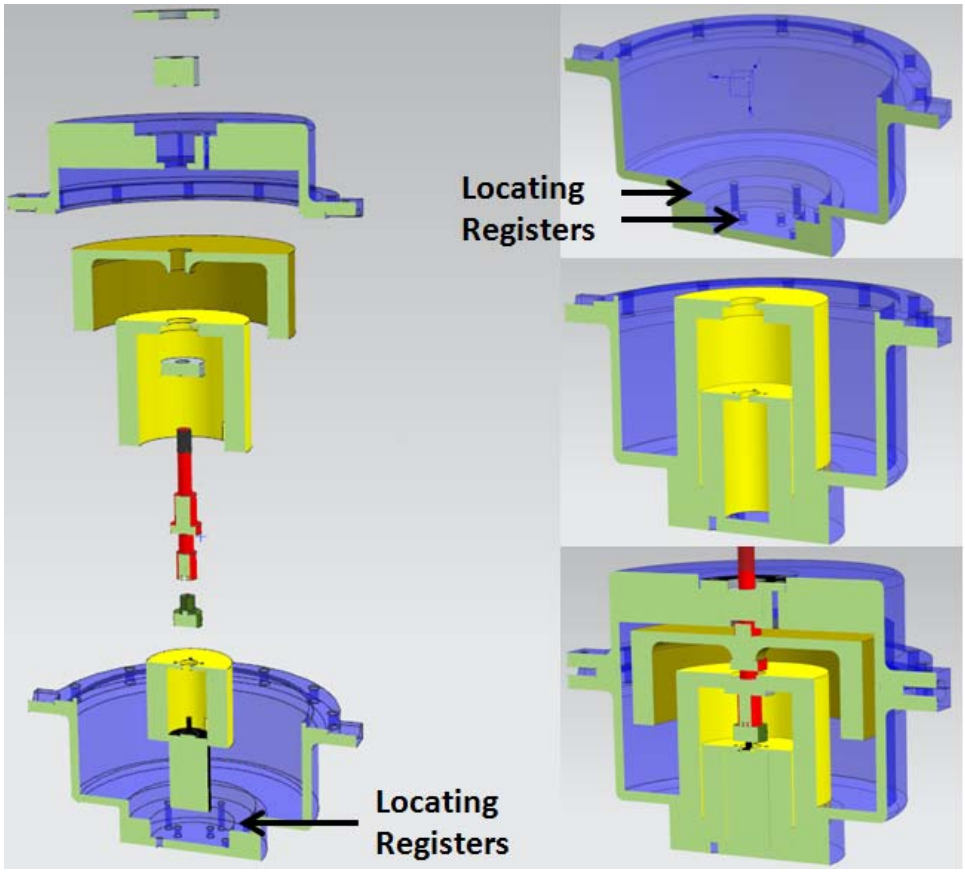

Figure 11. Second prototype CAD model

Although the 2nd prototype design shown in Figure 11 had minimal alignment issues, the momentum wheel assembly still consisted of 11 components each having a very small clearance between the next component. These tolerances would make it hard to assemble, required more parts to be manufactured and would make it hard to get the vertical placement of all of the pieces exact. Therefore, the design was modified in order to reduce the number components. This involved removal the single bearing (see Figure 9) and replacing the originally selected motor with a smaller form factor component. This was the final set of modifications and the end result was the final prototype momentum wheel assembly (see Figure 8).

B. MOMENTUM WHEEL ASSEMBLY COMPONENTS

In this section the five main components of the momentum wheel assembly are discussed: the momentum wheel, the motor, the duplex bearing, the shaft and motor

connector and the cases. The purpose of each momentum wheel assembly component, a discussion of the current R-SAT components, the key performance parameters and the component specifications of the final prototype are provided. The motor and duplex bearing sections provide a trade study prior to the discussing the final component specifications. The momentum wheel, the shaft including the motor connector and the cases were all custom components and therefore did not require COTS trade studies. The individual CAD illustrations shown in this section are intended to be used for visual aid purposes and are not to scale.

1. Momentum Wheel

The momentum wheel is the primary rotating mass that is used to induce the angular momentum which allows the momentum wheel assembly to operate. Therefore, the current momentum wheel moment of inertia (MOI) and angular momentum was evaluated to determine if it was suitable for the new R-SAT momentum wheel (see Figure 12).

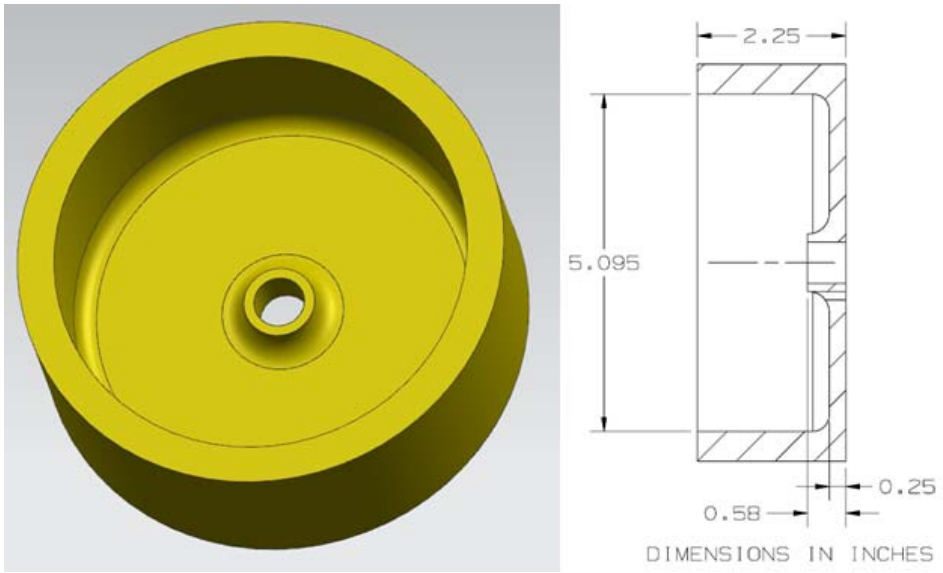

Figure 12. Current momentum wheel CAD model and dimensions

The MOI of the momentum wheel was obtained NX I-DEAS 6.1. The maximum angular momentum was calculated using Equation (1.2). The moment of inertia and

maximum angular momentum values for the current momentum wheel are shown in Table 2.

Parameter	Unit	Value
Maximum Angular Velocity	rpm	6,500
Maximum Angular Velocity	rad/sec	680.1
MOI of the Wheel	kg-m^2	0.00875
Maximum Wheel Angular Momentum	N·m·sec	5.96

Table 2. Current momentum wheel performance parameters

Since the current momentum wheel has been shown to be sufficient to control the R-SAT, there is no reason to make any significant design changes to the dimensions or wheel material. There was an addition, for the new wheel, of two dowel pin holes in order to make a more secure connection to the shaft and to maintain the alignment between the shaft and wheel while rotating (see Figure 13). Balancing requirements and procedures are discussed further in Chapter V.

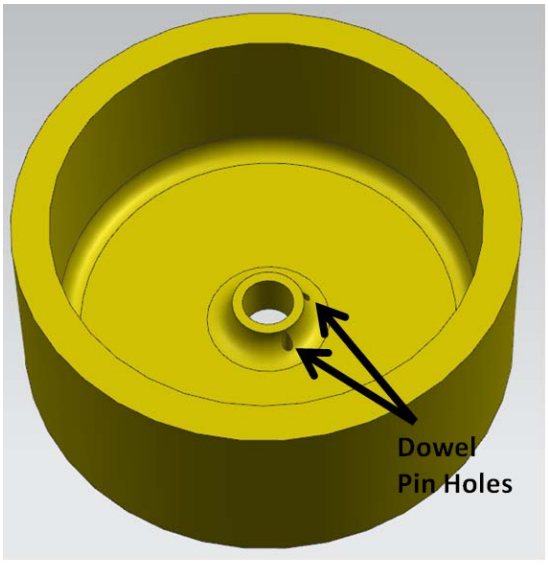

Figure 13. Final prototype momentum wheel CAD model and dimensions

2. Motor

The purpose of the motor is to rotate the momentum wheel at a nominally constant desired speed. The current momentum wheel assembly (Andrews Space) is powered by Emoteq Brushless DC motors, whose performance parameters and picture are shown in Table 3 and Figure 14, respectively [34].

Parameter	Unit	Value
Supply Voltage	V	24
No Load Speed	rpm	12,775
Stall Torque	Nm	0.08
Weight	kg	0.22
Peak Current	A	36

Table 3. Emoteq QB01700 brushless DC motor parameters (After [39])

Figure 14. Emoteq QB01700 brushless DC motor

Although the Emoteq motor is rated for 12,775 rpm, the current requirement for the R-SAT CMG is a maximum momentum wheel speed of 6,500 rpm [34]. Prior to

deciding on the motor component, a trade study was conducted in order to assess the capabilities and limitations of multiple types of motor options such as brushless direct current (DC) motors and brushed DC motors as well as frameless motors and housed motors.

Brushless DC motors (BLDC motors) produce torque using a permanent magnetic synchronous machine (PMSM) and use source inverters to alternate the current amongst the windings. Rotor position is sensed using such as Hall Effect sensors or an optical encoder. A common configuration for a BLDC is a three phase motor in which the inverters (poles) are positioned at 120 degrees apart (see Figure 15).

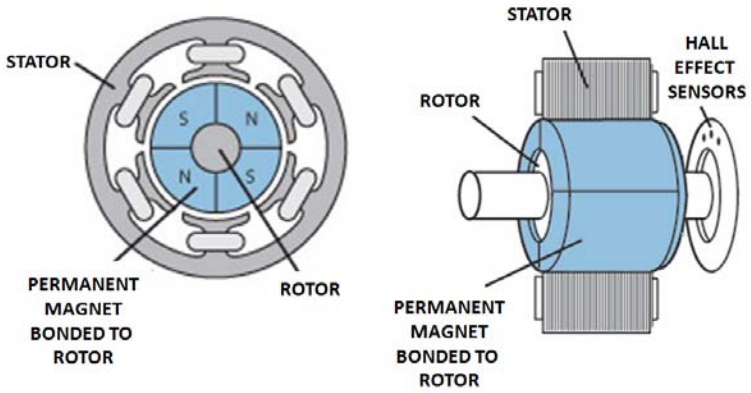

Figure 15. BLDC motor illustration (After [40])

As the PMSM is rotated, the magnetic attractive forces allow electrical energy to be converted to mechanical energy and thus producing the output torque of the motor [41]. Since BLDC motors rely on rotating mechanism to operate, they are subject to speed limitations, maximum current values, sinusoidal BEMF and are highly affected by temperature changes. Extreme temperature changes can cause a loss in magnetic flux density; which reduces the overall performance of the motor [42]. Despite these disadvantages, BLDC motors are reliable, provide high torque-to-inertia values, and require little maintenance [43], [44].

Brushed DC motors (BDC motor) consist of a stator, rotor, coiled windings, communtator, magnetics and brushes. The stator is stationary and has two magnets, while

the rotor rotates and consists of windings, output shaft and a commutator. The brushes are used to transfer current from the stationary stator to the spinning rotor (see Figure 16) [43], [45].

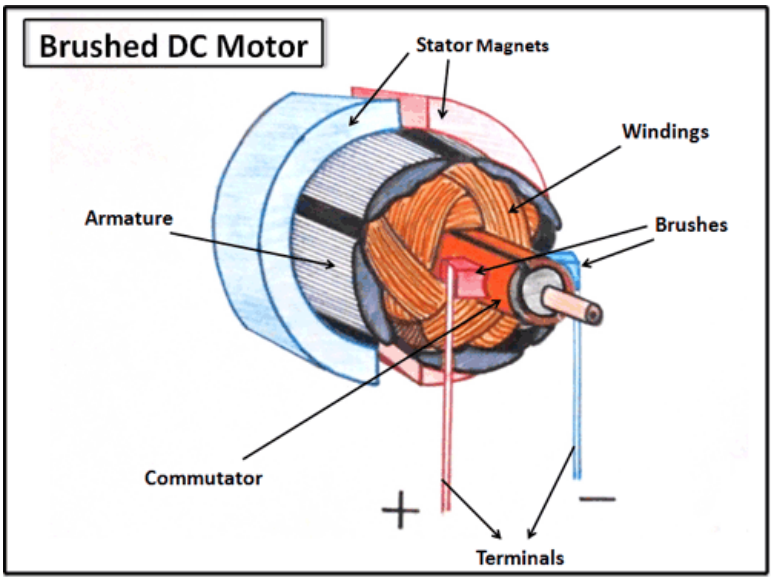

Figure 16. BDC motor illustration (From [45])

As current is applied to the motor the polarity of the windings change while the polarity of the stator magnets remains unchanged. The induced polarity change causes a magnetic misalignment between the rotor and the stator, which causes the rotor and the output shaft to rotate. The rotor will continue to rotate until it becomes aligned with a winding of the correct polarity. However, the motor is designed to continuously change the polarity of the windings in order to maintain the misalignment and so rotation will be continuous as long as there is power being supplied to the motor. BDC motors are one of the commonly used motor because of their simplicity and inexpensive. Since the output torque is proportional to the current, they tend to be large in size and require a fair amount of maintenance due to the fact that the brushes can wear [43], [45].

BLDC and BDC motors are offered with both frameless and housed motor configurations. Regardless of the configuration, the fundamental characteristics described

above remains unchanged, the configuration choices affect the type of application for which the motor can be utilized and how the motor will integrate with the system or load (see Figure 17).

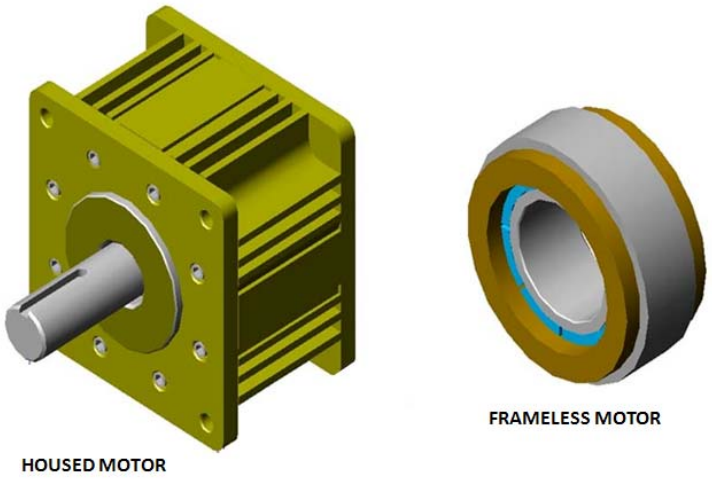

Figure 17. Illustration of a housed motor and a frameless motor (From [46])

Frameless motors do not include a shaft, bearings or endballs and are designed to be integrated directly into the system. This requires a more specialized mounting of the motor in order to be utilized. The absence of an external structure minimizes the motor's overall size and weight, but it also reduces the available support for key motor components [47], [48]. Housed motors have all essential parts of the motor inside an external structure. They often encompass the bearings, shaft connector and feedback devices within the housing. This allows for protection of the motor and for easy integration or coupling with existing systems. Housed motors are then mechanically linked to the load or shaft and are subject to torsional play [47]. Therefore, it is important to consider the published shaft play of a motor before integrating it into a design.

A housed BLDC motor was chosen for the momentum wheel motor. The BLDC housed motor allowed for an easy integration into the overall momentum wheel design are reliable, provide high torque-to-inertia values, and require little maintenance In addition to the parameters examined during the trade study, the final motor was also

selected based on other factors such as supply voltage, overall size, no load speed, stall torque, weight and current, cost including cables, attachments and software, shipment date, and manufacturer customer support availability.

The motor choices were narrowed down to the Emtoeq QB01700, the Faulhaber series 3056–024B and Maxon EC-45 Flat Motor. The performance parameters for all three motors are shown in Table 4.

		Emoteq QB01700	**Faulhaber 3056–024B**	**Maxon EC-45**
Parameter	**Unit**	**Value**	**Value**	**Value**
Supply Voltage	V	24	24	24
No Load Speed	rpm	12,775	8,200	6,700
Stall Torque	Nm	0.08	0.098	0.822
Weight	kg	0.22	0.19	0.11
Length	mm	54	56	21.3
Diameter/Width	mm	41.7	30	62.1

Table 4. Possible motor options

The Emoteq QB01700 brushless DC motor was decidedly not the best choice for the new momentum wheel assembly. The overall motor size is too large for the new design, is considerably more expensive than motors of its caliber, and at the time of this thesis was not readily available for purchase. The Faulhaber motor was used in the 2nd prototype (see Figure 11), but was not selected for the final prototype due to its extensive length. The overall size of the momentum wheel assembly is a function of the components inside, therefore the size of the assembly is affected by the size of the motor. The final motor chosen for the momentum wheel assembly was the Maxon EC-45 (see Figure 18). Not only does the Maxon motor meet all the required parameters, but is

readily in stock for future purchases and is considerably smaller than the other motor choices. The change in the motor selection reduced the height of momentum wheel housing assembly by 34 mm (1.3 inches).

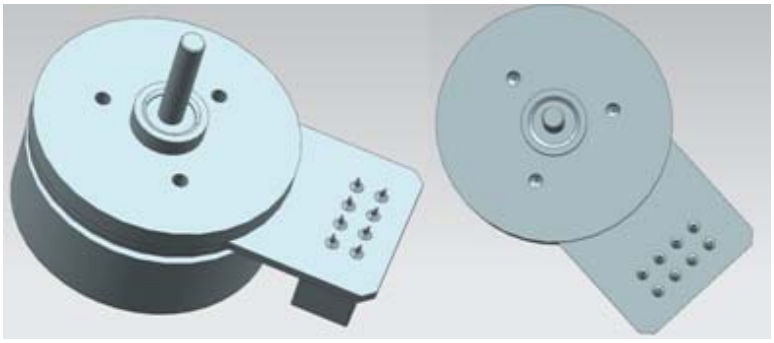

Figure 18. Maxon EC 45 flat motor

3. Bearing Selection

The bearing is used to support the rotation of the wheel by reducing the friction of the rotating mass [49]. Bearings are essential for this application since the momentum wheel is rotating at high speeds. The current momentum wheel assembly utilizes a McMaster-Carr flange-mounted needle roller bearing 1434k6 whose performance parameters and dimensions are shown in Table 5 and Figure 19, respectively.

Parameter	Unit	Value
Bore	in	1/2
Dynamic Load Rating, Radial	lbs	1,040
Maximum rpm	rpm	22,000

Table 5. Current needle bearing performance parameters (After [50])

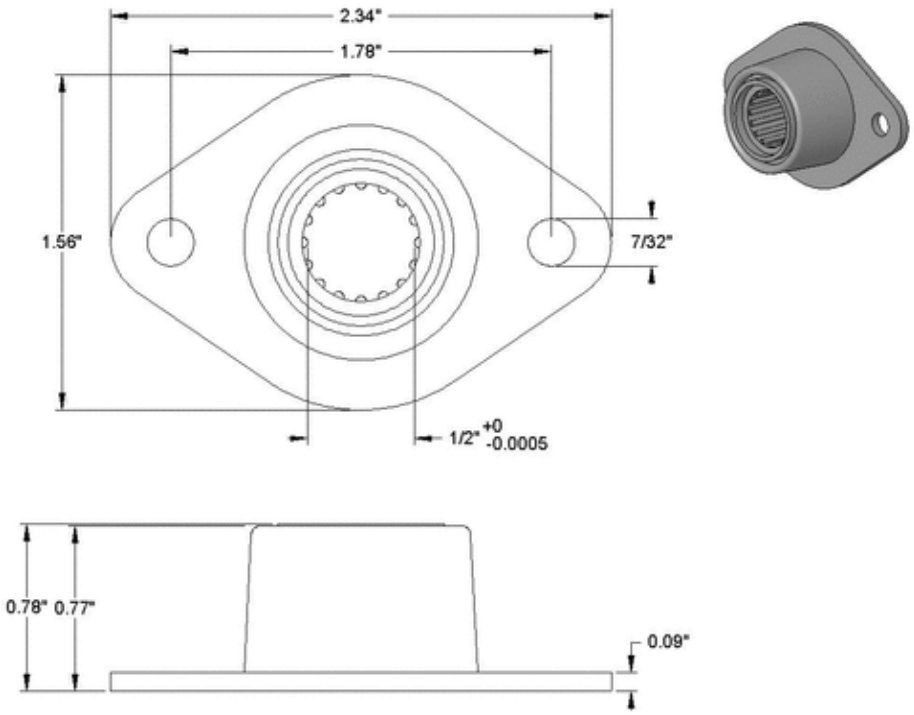

Figure 19. Dimensions of needle bearing in current momentum wheel assembly (From [50])

A trade study was conducted for multiple types of bearings such as ball bearings and roller bearings in order to determine the best bearing type for the final prototype. In addition to the different bearings types, the following bearing configurations were also examined: single row and duplex. The trade study focused on the mechanical design principles behind each bearing and key performance parameters such as installation space, bore diameter, bearing life rating, maximum speed and preloading requirements [51].

Ball bearings come in three main types: radial contact angle ball bearings, thrust bearings and radial deep groove bearings; each of these bearing provides a smooth, low friction surface for a load, but they differ greatly in their applications. Radial contact angle ball bearings can handle heavy axial loads and moderate radial loads. Contact bearings also require a specific amount of axial force, also known as preload, in order to

achieve the proper contact angle or clearance for the rolling elements. Contact angle is defined as the angle formed between the applied load and the rolling element (see Figure 20).

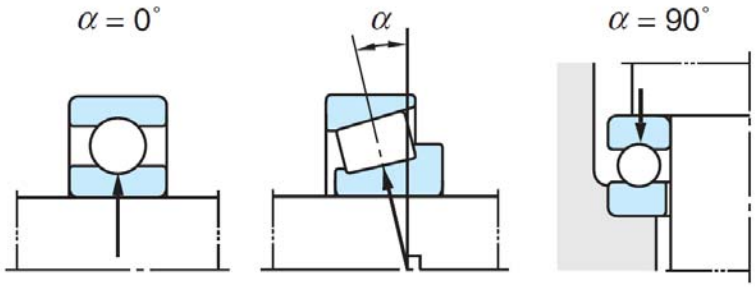

Figure 20. Contact angle illustration (From [51])

Preloading a bearing also increases the stiffness which helps to reduce bearing play (see Figure 21) and increases the quality of the bearings output [52]. This aspect is very useful in an application that requires high precision such as a momentum wheel.

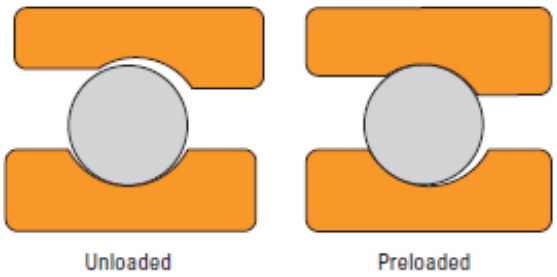

Figure 21. Effect of preloading on ball bearings (From [52])

Thrust bearings are designed to handle very high axial loads, but cannot support radial loads. Radial deep groove bearings are designed to handle radial loads, but can also handle a varying degree of axial loads. The load handling capability of a bearing, however, depends on the specific performance parameters of the bearing and its application [53]. Ball bearings are some of the most common bearings used today, but they are often known for having problems with lubrication and bearing life due to fatigue [51], [54].

Roller bearings are available in multiple variations such as needle roller, cylindrical roller and tapered roller bearings. Roller bearings have a line contact area between the roller and the load (shaft). This allows them to have more contact area with the load. They are commonly used in application where space is limited and where a high load capacity is required. Roller bearings also have the disadvantage of higher friction since more needles are in contact with the shaft [55]. Needle roller bearings are rollers whose length are at least 4 times their diameter and are capable of carrying high radial loads with a small section height [56]. Cylindrical roller bearings are designed to accommodate an axial load in one direction. They have a high axial rigidity, but are not designed to carry radial loads. Tapered roller bearings are designed for heavy loads, vibration or impact applications and carry axial loads.

Duplex bearings have an advantage over a single row bearing in an application where axial and radial deflections must be at a minimum, both single and reversing thrust loads must be supported, moment loading may be present, and the shaft location is critical. The placement of each bearing in the duplex pair is also critical and can affect the way the bearings behave. For example, the bearings can be mounted face-to-face, back-to-back or tandem (see Figure 22). Back-to-back mounting positions the contact angle lines are diverging inwardly, face-to-face mounting positions the contact angle lines are converging inwardly, and tandem mounting positions the contract angle lines are parallel (see Figure 22) [57].

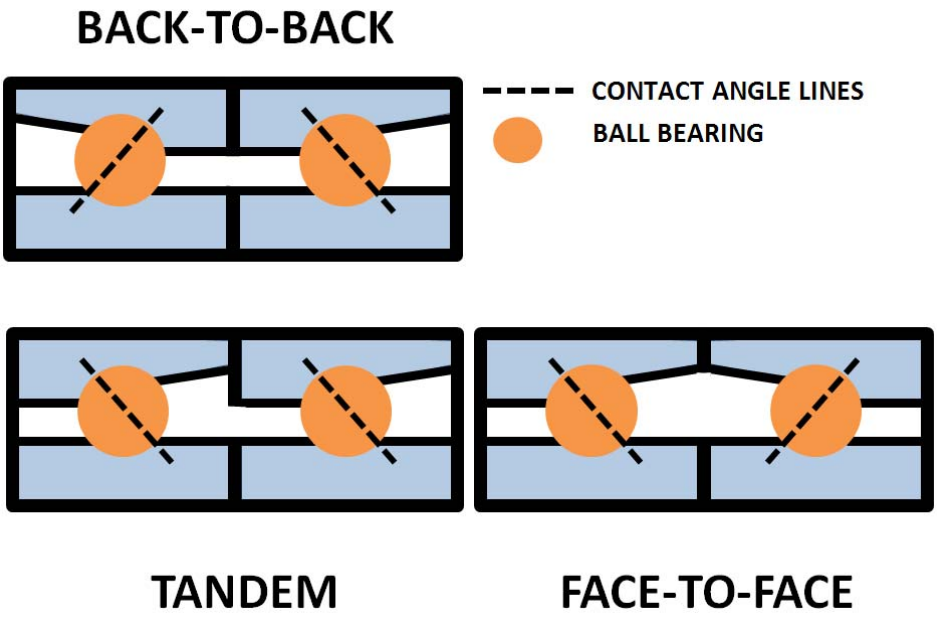

Figure 22. Duplex bearing placement illustration

Back-to-back mounting allows the bearings to carry radial, axial and moment loads and is utilized for applications where shaft is rotating in one direction and misalignment is a high priority. Face-to-face mounting allows the bearings to carry radial, axial loads and allows a shaft to change directions. Tandem mounting allows the bearings to carry very large thrust loads and are used when the shaft is only moving on direction [57].

Although both the contact angular ball bearings and the tapered roller bearing seem to have similar performance parameters, a closer look at each of their capabilities reviles that contact angular ball bearing is the best choice for the momentum wheel assembly because they have high accuracy and are excellent at high speed adaptability (see Table 6).

	Angular Contact Ball Bearing		Tapered Roller Bearing	
Parameter	**Single Row**	**Duplex**	**Single Row**	**Duplex**
Radial Load	Good	Excellent	Excellent	Excellent
Axial Load	Excellent	Excellent	Excellent	Excellent
Combined Load	Good	Excellent	Excellent	Excellent
Vibration or Impact Load	Fair	Fair	Excellent	Excellent
High Speed Adaptability	Excellent	Excellent	Good	Good
High Accuracy	Excellent	Excellent	Good	N/A

Table 6. Bearing performance parameters (After [51])

In addition to the parameters listed in the trade study, the bearing must be able to handle the static loads and dynamic loads of the momentum wheel assembly. The static load is the defined as the maximum permissible load that will produce a permanent deformation when it is applied to a non-rotating bearing and can be calculated using Equation 3.1. [55], [52].

$$F = mg \tag{3.1}$$

where F is the force, m is the of the load and g is the value of gravity on the Earth's surface. The static load for the bearing is a function of the rotor assembly mass of 3.39 kg, therefore the bearing is subject to a static load of about 33 N load. The complete rotor assembly will be discussed in further detailer later in this thesis. The load value of 33 is for a purely axial or radial load.

In general, a static factor of safety (FOS) of 3–4 is used to determine the total bearing capacity where the static FOS is defined as the ratio between the basic static load rating and the equivalent dynamic bearing load [58]. Therefore, the bearing with a FOS of 4 must be able to handle both radial and axial loads equal to 133 N. The dynamic load rating is used to estimate life of a rotating bearing. It is also known as basic rated life and

is often defined as the load value that the bearing can while surviving 1 million revolutions. The basic rated life in millions of revolutions is:

$$L_{10} = \left(\frac{C}{P}\right)^{q} \tag{3.2}$$

where L_{10} is basic rated life, C is basic dynamic load rating, P is the equivalent dynamic bearing load and q is the exponent in life equation and is equal to 3 for ball bearings [55], [52]. The dynamic equivalent bearing load is:

$$P = XF_r + XF_a \tag{3.3}$$

where X is the radial load factor, F_r is the applied radial load, Y is the axial load factor and F_a is the applied axial load. The dynamic load calculation cannot be completed until the bearing in chosen and the basic dynamic load rating and equivalent dynamic load factors are known.

Based on all of the information listed above, the Timken 2MM200WI contact angle ball bearing with a back-to-back duplex mounting configuration was chosen. This bearing and configuration allows the bearing to support more than 18 times the calculated static axial and radial loads (see Table 7).

Parameter	**Unit**	**Value**
Bore	mm	10
Outside Diameter	mm	30
Width	mm	9
Static Load Rating	N	2,550
Extended Dynamic Load Rating	N	7,100
Contact Angle	deg	15
Preload Requirement	N	20

Table 7. Timken 2MM200WI duplex bearing performance parameters (After [52])

Once the bearing choice was been made, the dynamic equivalent bearing load calculation shown in Equation (3.3) was modified for the Timken 2MM200WI duplex bearing:

$$P = 0.72F_r + 1.625Y_2F_a \tag{3.4}$$

where F_r is the applied radial load, Y_2 is the duplex bearing load factor and F_a is the applied axial load. The duplex bearing load factor is a function the ratio of the applied axial load and the basic dynamic load rating, $K_T = \frac{F_a}{C}$, and was obtained by using Table 8. The value of K_T was found to be 0.036, so the final value of Y_2 was found through interpolation to be 1.37. Using Equation (3.5) and the static loads calculated above, the maximum dynamic equivalent bearing load without a FOS is 23.95 N which occurs when the bearing is subject to a purely radial load. The minimum dynamic equivalent bearing load is 1.95 N which occurs when the bearing is subject to a purely axial load. The basic rated life in millions of revolutions was calculated using Equation (3.3) and maximum dynamic equivalent bearing load of 23.95 N and was found to be $2.6e10^7$ revolutions (26 million revolutions). The analysis of the dynamic and static loads values showed that the Timken 2MM200WI duplex bearing would be sufficient for the final momentum assembly.

K_T	Y_1	Y_2	Y_3
0.015	2.30	1.47	1.60
0.020	2.22	1.44	1.59
0.025	2.10	1.41	1.57
0.030	2.00	1.39	1.56
0.040	1.86	1.35	1.55
0.050	1.76	1.32	1.53
0.060	1.68	1.29	1.51
0.080	1.57	1.25	1.49
0.100	1.48	1.21	1.47
0.120	1.42	1.19	1.45
0.150	1.34	1.14	1.42
0.200	1.25	1.09	1.39
0.250	1.18	1.05	1.35
0.300	1.13	1.02	1.33
0.400	1.05	1.00	1.29
0.500	1.00	1.00	1.25
0.600	—	—	1.22
0.800	—	—	1.17
1.000	—	—	1.13
1.200	—	—	1.10

Table 8. Duplex bearing load factors for Timken bearings (From [52])

4. Shaft and Motor Connector

The shaft and the motor connector is the primary coupling device that transmits torque from the motor to the load (momentum wheel). The current (Andrews) shaft cannot be used for the final prototype, since all components have been altered. Therefore, a new shaft was designed. The final shaft design was also dependent on what it is supporting and the arrangement of the bearings and the motor connector. For example, the current shaft has a cantilevered design because the bearing is mounted inside the outer casing of the momentum wheel assembly and the load is concentrated at the end of the shaft. The position of the bearing only allows it to support only one side of the shaft (see Figure 23).

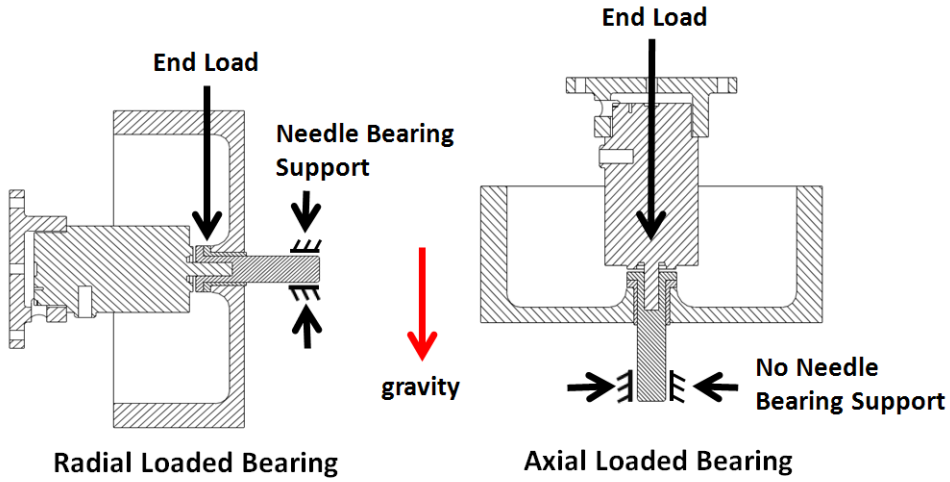

Figure 23. Radial and axial loading of the Andrews shaft configuration (After [59])

Although the other side of the motor is securely mounted to the other side of the casing, there is no other support between the load and the motor. In addition, the current bearing dynamic load rating is for radial loads only and cannot carry any axial loads on the shaft. Therefore, the motor shaft is subject to axial and radial loads created by the momentum wheel which have led to motor to failures because the motor shaft and the bearing assembly is not designed to handle these kinds of loads.

In addition to the supporting arrangement, the final shaft dimensions are also dependent on the other components. Therefore, the following shaft parameters were set based on the momentum wheel and duplex bearing specifications:

1. Shaft diameter through the wheel 0.6270 inches (15.9258 mm)
2. Shaft diameter through the bearings 10 mm
3. Shoulder required for mounting the momentum wheel
4. Shoulder required for duplex bearing

The final prototype shaft (see Figure 24) was designed with two shoulders which help to keep the alignment of the assembly and to keep the vertical spacing of the

components accurate. The first shoulder is used to hold the inner races of the duplex bearing and to maintain the bearing placement while the preloading torque is applied to the torqueing nut.

The second shoulder is used to hold the momentum wheel and is used to align the wheel and the shaft. The momentum wheel shoulder is wider and thicker than the first shoulder since it needs to distribute the mass of the wheel and to accommodate for the addition of two dowel pins. The shaft also has threads to accommodate a locking nut for the momentum wheel and for the bearing nut required for preloading. The overall length of the shaft and the thread parameters are a function of the momentum wheel case design and depends on the dimensions of every other component; therefore, these parameters were decided upon as one of the final steps in the design process.

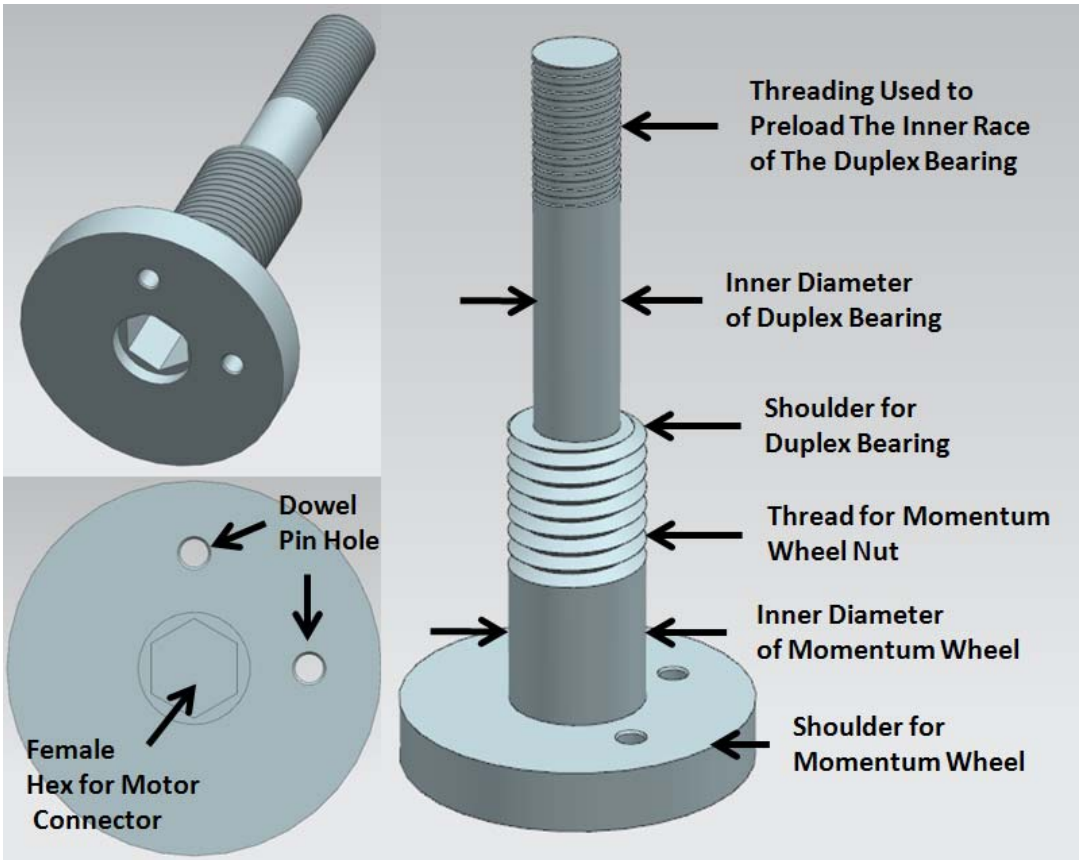

Figure 24. Final prototype shaft CAD model

The final prototype shaft also has a cantilevered shaft where one side is supported by a the Timken 2MM200WI duplex bearing and the load is concentrated at the end (see Figure 25 and Figure 24). However, because the bearing is positioned closer to the center of mass of the wheel, the moment loading is significantly less. Also, unlike the needle bearing, the Timken 2MM200WI duplex bearing is designed to handle both axial and radial loads (see the previous section). So the wheel is support properly in any orientation.

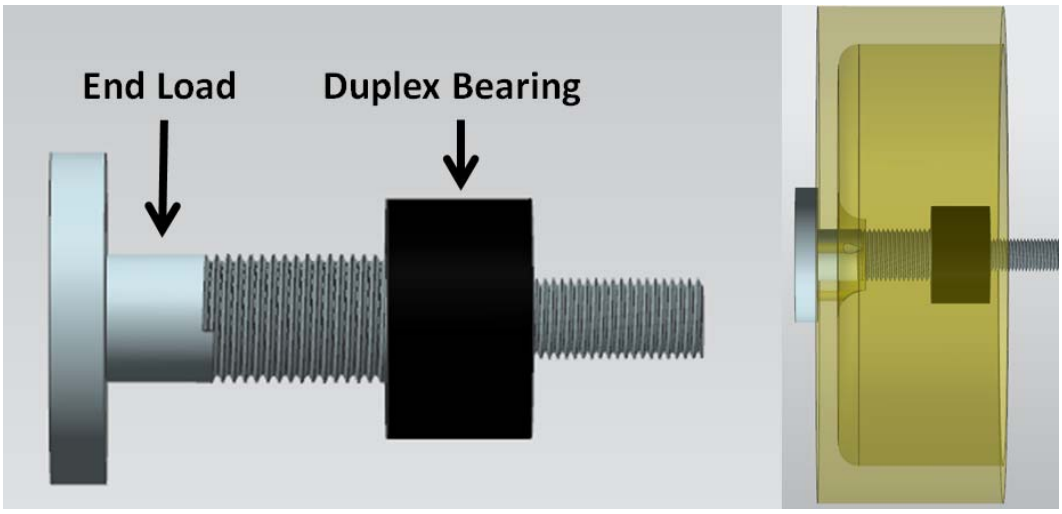

Figure 25. Final prototype cantilevered shaft

The final prototype shaft (see Figure 24) was manufactured using stainless steel 304 (SST-304) whose material properties for are shown in Table 9.

Parameter	Units	Value
Tensile Strength, Ultimate	MPa	505
Tensile Strength, Yield	MPa	215
Modules of Elasticity	GPa	193–200
Poisson's Ratio	GPa	0.29
Shear Modulus	GPa	86

Table 9. Material properties for SST-304 (After [60])

The shaft elasticity also referred to as stiffness is defined by:

$$K_s = \frac{QJ_p}{L_s} \tag{3.5}$$

where K_s is the shaft stiffness, Q is the shear modulus, J_p is the polar moment of inertia of the shaft, and L_s is the length of the shaft. The polar moment of inertia of the shaft is defined as:

$$J_p = \frac{\pi}{32} D^4 \tag{3.6}$$

where D is the diameter of the shaft. The maximum shear stress, which occurs on the outermost surface of the shaft, is defined as:

$$\tau_{\max} = \frac{Tr}{J_p} \tag{3.7}$$

where $\tau_{\max}$ is the maximum shear stress, r distance from the center of the shaft to the outermost surface and T is the maximum torque that the shaft is subject to; which is equal to the maximum torque value of 822 mNm from the Maxon EC-45 Flat motor. The radians is the maximum angle that the shaft will twist when subject to a torque is defined as:

$$\phi = \frac{TL_s}{GJ_p} \tag{3.8}$$

where ϕ is the maximum twist angle in. Shaft elasticity or torsional stiffness is defined as:

$$\psi = \frac{T}{\phi} \tag{3.9}$$

where ψ is the shaft elasticity and ϕ maximum twist angle. Since the shaft has three different diameters, the performance parameters were calculated for each segment separately and are shown in Table 10. The first segment corresponds to the inner diameter of the duplex bearing, the second segment corresponds to the inner diameter of the momentum wheel and the third segment corresponds to the diameter of the momentum wheel shoulder.

Parameter	Units	Segment 1	Segment 2	Segment 3
Diameter	mm	10	15.93	41.33
Length	mm	39.34	35	6.83
Polar Moment of Inertia	mm^4	9.81e2	6.32e3	2.86e5
Shaft Stiffness	Nm	2.15e3	1.55e4	3.6e6
Maximum Twist Angle	rad	3.83e-4	5.29e-5	2.28e-7
Maximum Shear Stress	MPa	4.16	1.04	0.059
Shaft Elasticity	Nm/rad	2.15e2	1.55e4	3.6e6

Table 10. Final prototype shaft analysis

The shaft analysis shown in Table 10 proves that the current shaft design is capable of handling the loads of the newly design momentum wheel assembly. The maximum shear stress for the shaft is 4.16 MPa which is considerably lower than shear modulus of 86 GPa. So, the shaft will not fail in shear.

In addition to the shaft, the motor connector is also an important aspect since the momentum wheel assembly will be spinning with such high rotational speeds, it is this is

critical that the motion between the motor, shaft and wheel be transmitted along the same axis of rotation. Any unwanted vibrations or wobbling in the shaft, wheel or motor connector while the momentum wheel is spinning it could cause the entire momentum wheel assembly to fail [61]. Therefore, both the 2nd and final prototypes used a hex key to couple the motor connector and the shaft (Figure 26). The hex key connection type allows for minimal movement between the two parts by providing a large surface area for connecting the two components. This ensures that the full torque of the motor is transmitted to the shaft. The integration of all of the momentum wheel assembly components including the shaft with the motor connector is discussed further in Chapter V.

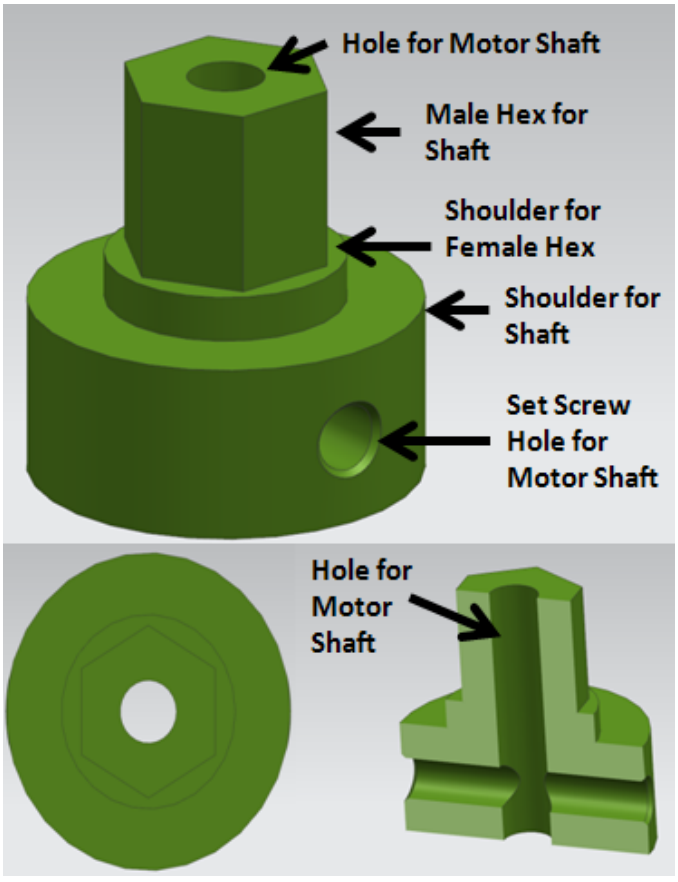

Figure 26. Motor connector CAD model

5. Cases and Bearing Washer

The purpose of the casings is to house and protect the parts of the momentum wheel assembly. Since most of the current momentum wheel components have been altered, the current momentum wheel casing could not be used for the new design. The final prototype momentum wheel assembly has two cases: the outer case and the motor case. The outer casing has two parts: the bearing side case and the motor side case

A requirement of overall size of the outer casing was obtained through inspection of the current gimbal assembly. The casing would also need to connect to the gimbal assembly using a ½ inch shaft and slotted spring pin. This is a design requirement based on the current gimbal mounting and will discussed further in the next chapter. In addition to the size requirements, each side of the case was designed to secure, protect and maintain alignment of other momentum wheel assembly components.

The bearing side case was designed to house the bearing, protect the spinning momentum wheel and connect to the other side of the case. The bearing side case was also designed to have a shoulder for a bearing washer. This washer was designed to hold the duplex bearing in place. The bearing washer and its dimensions are shown in Figure 27.

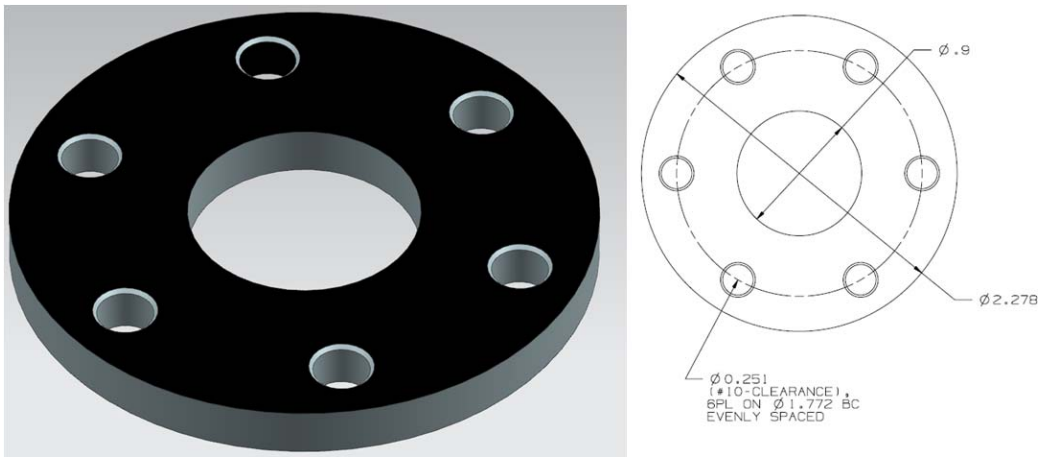

Figure 27. Bearing washer CAD model

In addition to housing the bearing, the casing also has to align properly with the motor side outer casing so the casing was designed with a female locating register (see Figure 28).

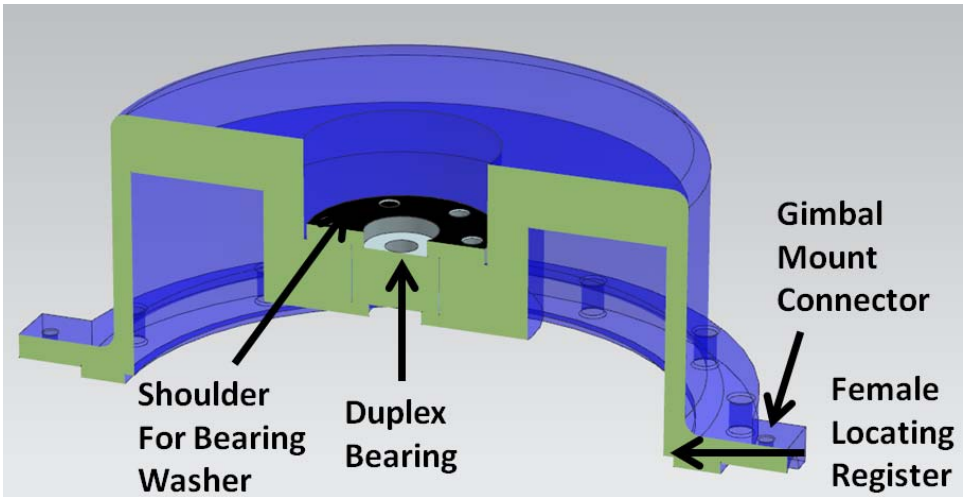

Figure 28. Bearing side case CAD model

The motor side case was designed to secure the motor and connect to the bearing case. The motor case has two locating registers, one is for the motor casing and the other is the male locating register which connects to the bearing side case (see Figure 29) The precise alignment of both of these registers is very important; any alignment issues with the casing will propagate throughout the entire assembly and can cause a failure of the rotor assembly.

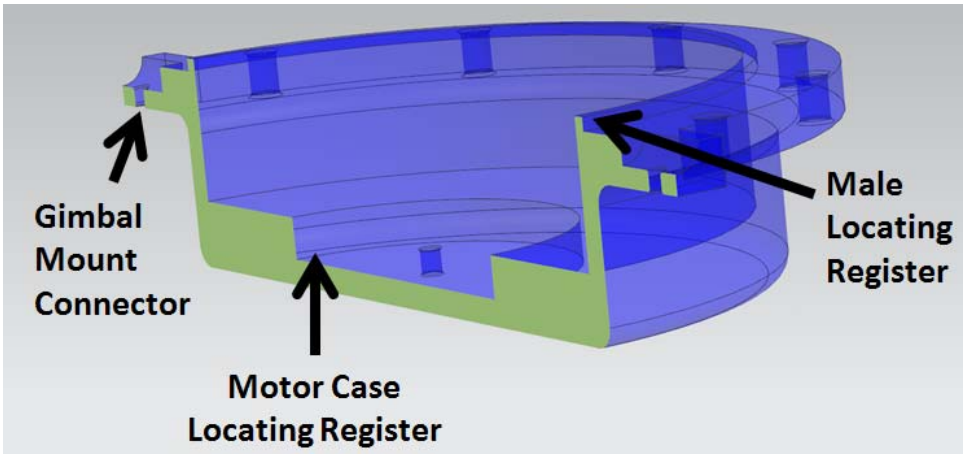

Figure 29. Motor side case CAD model

A motor case was also designed to house and secure the BLDC motor and to ensure that the motor was proper aligned with the other momentum wheel assembly components. (see Figure 30). The integration of all of the momentum wheel assembly components is discussed in detail in Chapter V.

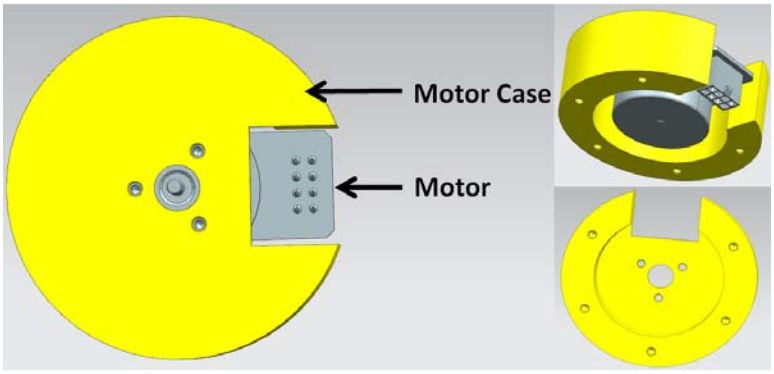

Figure 30. Motor case CAD model

THIS PAGE INTENTIONALLY LEFT BLANK

IV. GIMBAL ASSEMBLY

This chapter discusses the mechanical characteristics of the gimbal assembly and its components which include: the motor, gearhead, absolute optical encoder and gimbal frame (see Figure 31). As previously stated, a CMG is a constant speed momentum wheel mounted on a pivoted support structure also known as a gimbal. Therefore, the momentum wheel assembly designed will only become a CMG once it is attached to the gimbal assembly. This chapter also focuses on evaluating the suitability of the gimbal assembly with the newly designed momentum wheel assembly attached.

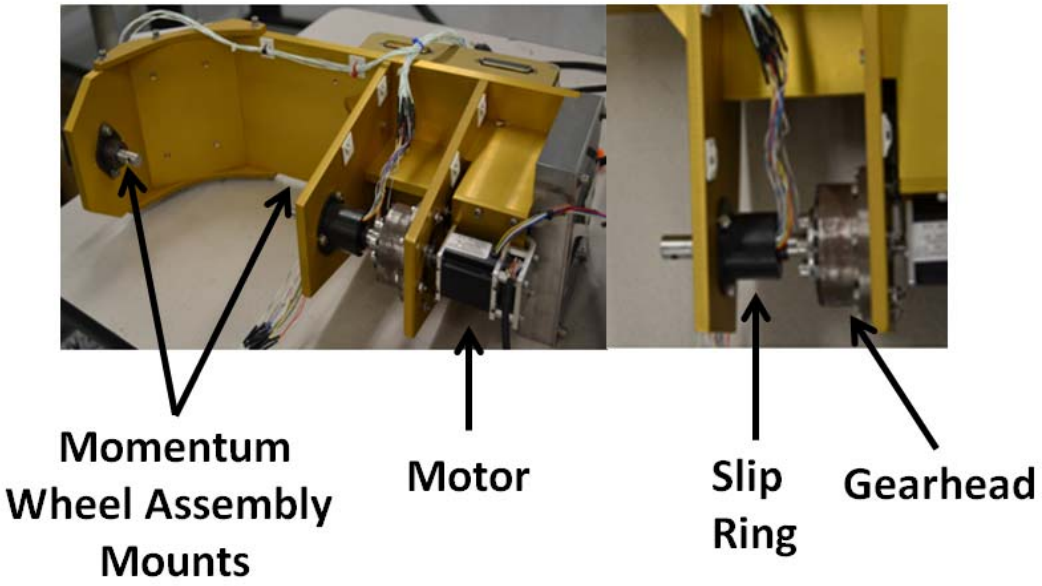

Figure 31. Spacecraft simulator gimbal assembly

A. GIMBAL ASSEMBLY EVAULATION

The gimbal assembly is much like the momentum wheel assembly in that all of its components are coupled and making even a small change in one component choice can cause a ripple effect through the entire assembly, i.e., the motor size, encoder choice, gearhead ratio. The gimbal assembly differs in that its performance is highly dependent on the size, weight and moment of inertia of the load that it is trying to rotate. Therefore,

the gimbal assembly was first integrated with the newly designed momentum wheel assembly prior to being examined. The assembly will now be referred to as the CMG, since the momentum wheel assembly and the gimbal are integrated. The performance of the CMG assembly was then evaluated with respect to the R-SAT by using a simplified double integrator problem formulation. This was done to ensure that the design is sufficient to integrate onto the R-SAT. The performance parameters for one newly designed CMG mounted on the R-SAT are shown in Table 11.

Parameter	Unit	Value
CMG Speed	rpm	6,500
CMG rotor nominal rotating mass	kg	3.39
Momentum Wheel Moment of inertia	kg· m^2	0.0139
Gimbal Moment of inertia	kg· m^2	0.0114
Moment of Inertia of the Spacecraft	$kg \cdot m^2$	37.12
Gimbal Motor Stall Torque	mNm	80

Table 11. Performance parameter for newly designed CMG mounted on the R-SAT

The double integrator mode is the simplest mathematical model that defines the relationship between a CMG and a spacecraft and is derived from the equations shown in Chapter II. The differential equations, assuming that the CMG is mounted perpendicular to the spacecraft spin axis, are in state-space form:

$$\dot{\theta}_{sc} = \omega_{sc} \tag{4.1}$$

$$\dot{\delta} = \delta_v \tag{4.2}$$

$$\dot{\omega}_{sc} = -\frac{1}{J_{sc}} h_{cmg} \cos(\delta)\delta_v \tag{4.3}$$

$$\dot{\delta}_v = \frac{1}{J_g}\left(\tau_g + h_{cmg} \cos(\delta)\omega\right) \tag{4.4}$$

where θ_{sc} is spacecraft attitude angle, ω_{sc} is the spacecraft body rate, $\dot{\omega}_{sc}$ is the spacecraft body acceleration, J_{sc} is the moment of inertia of the spacecraft along its spin axis, τ_g is the gimbal torque, h_{cmg} is angular momentum of CMG, δ is gimbal angle of the CMG,

$\dot{\delta}$ and δ_v is the gimbal rate, $\dot{\omega}$ is the spacecraft acceleration, $\dot{\delta}_v$ is the gimbal acceleration and J_g is the moment of inertia of the CMG along the gimbal axis. If this analysis was conducted along another axis the final solutions would change based on the moment of inertia values shown in the fully populated moment of inertia matrix:

$$J_{spacecraft} = \begin{bmatrix} 37.245 & 0.590 & 0.052 \\ 0.590 & 39.88 & 0.085 \\ 0.052 & 0.085 & 70.03 \end{bmatrix} kg \bullet m^2$$

The double integrator problem was be used to determine the maximum maneuver rate or how fast the R-SAT can maneuver using the current configuration. Solving Equation (4.4) for ω using the values found in Table 11, the maximum maneuver rate for R -SAT is 0.24 degrees per second. This means that the R-SAT would take 123 seconds to conduct a 30 degree maneuver. The maximum maneuver rate for the R-SAT can be improved by adding a gearhead to the gimbal motor. When a gearhead is added to the system, Equation (4.4) becomes:

$$\dot{\delta}_v = \frac{1}{J_g}\left(\tau_g + \left(\frac{1}{R}\right) h_{cmg} \cos(\delta)\omega\right) \tag{4.5}$$

where R is the gear ratio of the gimbal gearhead. The maximum maneuver rate for R -SAT with a gimbal gearhead ratio of 100 is 24.2 degrees per second. With a gearhead added, the R-SAT takes 1.24 seconds to conduct a 30 degree maneuver, which is more realistic for an agile spacecraft. In reality the maneuver would take longer than 1.24 seconds because the acceleration has not been accounted for.

The actual R-SAT point-to-point maneuver time can be found by using the pseudospectral method implemented in DIDO and solving for a time optimal solution. DIDO is MATLAB-based program which solves optimal control problems using a set of differential equations for the dynamics model, a minimized independent variable, control variable and boundary conditions [62], [63]. The four models were used to write four MATLAB functions: a dynamics function, a cost function, an event function and a MATLAB code to run DIDO. The dynamics function defines the differential equations or system dynamics given by Equations (4.1) to Equation (4.3) and Equation (4.5).

The cost function defines a functional which contains decision variables for the given problem. Since this is a time optimal problem, the decision variables are the final time, the control variable and the state variables for the spacecraft. The cost function is written as:

$$J[x(\bullet), u(\bullet), t_f] = t_f \tag{4.6}$$

where t_f is the final time, $x(\bullet)$ is the state function or trajectory in state space and $u(\bullet)$ is control function or trajectory [64]. The 'event' function defines the constraints of the problem. The constraints in this case are the initial and final condition states of the CMG gimbal and spacecraft. The initial boundary conditions for the spacecraft and the CMG gimbal are all set to zero.

$$(\theta_0, \omega_0, \delta_0, \delta_{v_0}) = (0, 0, 0, 0) \tag{4.7}$$

The final boundary condition occurs when the spacecraft has completed a 30 degree maneuver around its spin axis and all other variables have returned to zero.

$$(\theta_f, \omega_f, \delta_f, \delta_{v_f}) = (30, 0, 0, 0) \tag{4.8}$$

The main DIDO MATLAB code is used to run (call) the DIDO program; which starts the DIDO program, defines the control variable and defines the boundary conditions. The control variable is the torque supplied by the gimbal motor and is defined by:

$$u = \tau_g \tag{4.9}$$

where u is the control variable equal to the gimbal torque. This was used as the limiting control variable because the gimbal torque limits the maneuvering ability spacecraft.

DIDO has two different modes of operation, normal mode and accurate mode and both modes are capable of obtaining accurate solutions. There are some problems for which a normal solution does not improve with the addition of nodes; this is when accurate mode can be used to generate a more accurate solution. It is important to note, that the simulation run time increases when DIDO is in accurate mode, so it will take longer to achieve a solution [63]. Figure 32, Figure 33 and Figure 34 plot the results for analysis the simulation.

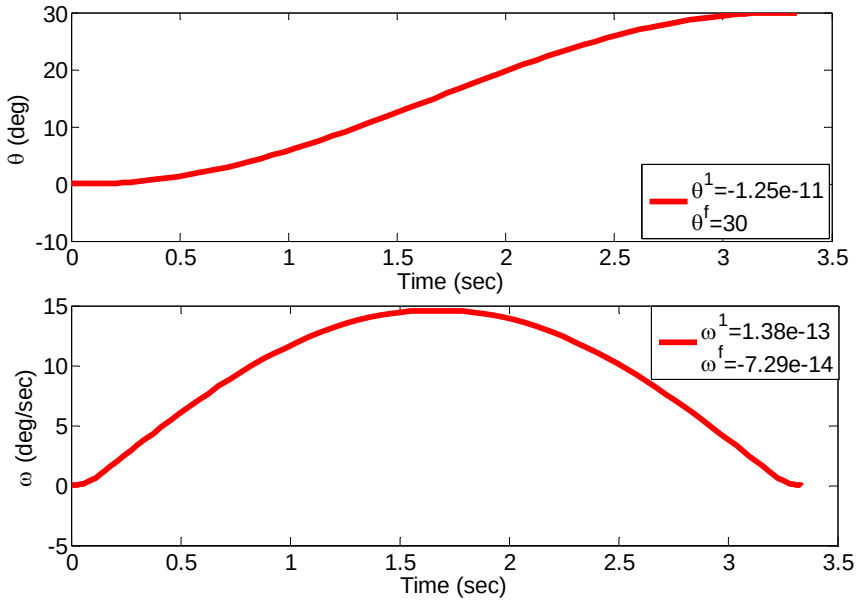

Figure 32. Spacecraft attitude and rate during time optimal maneuver

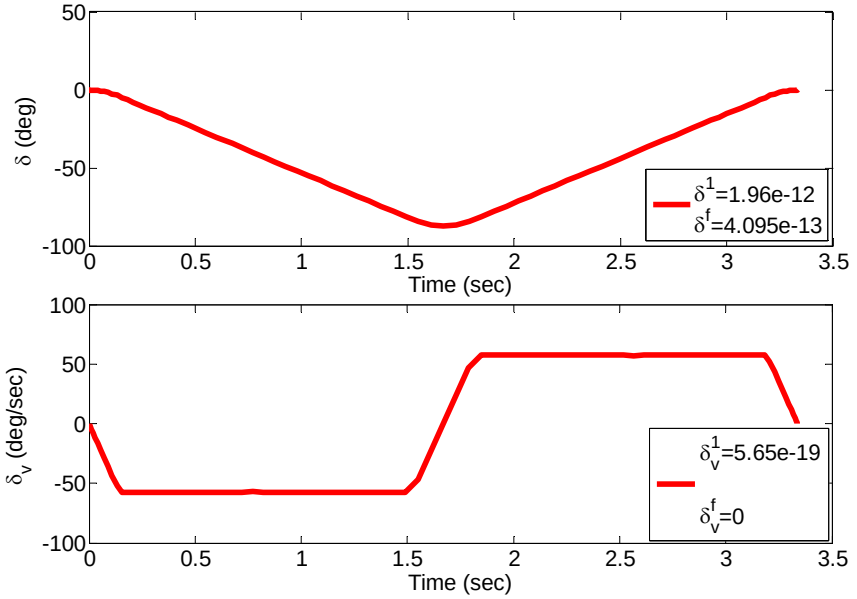

Figure 33. Gimbal position and rate during time optimal maneuver

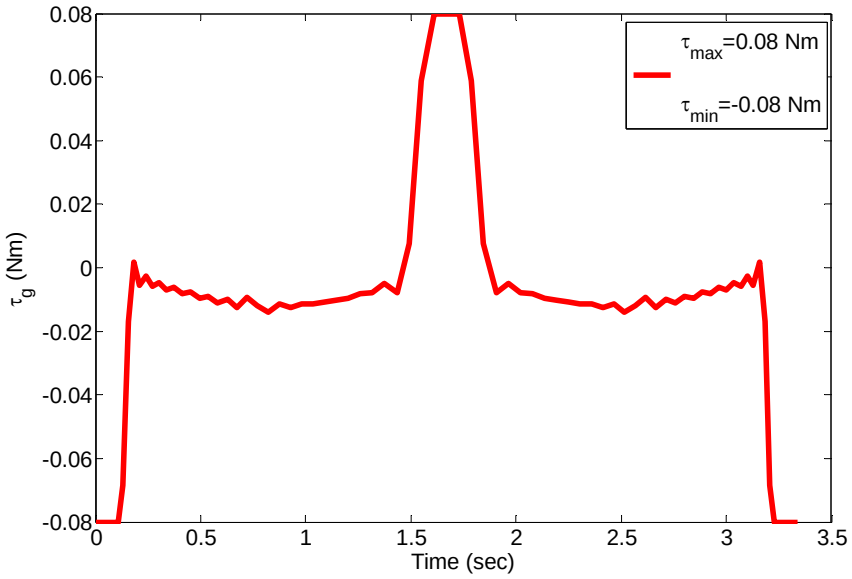

Figure 34. Gimbal control torque required for time optimal maneuver

The results show that current gimbal assembly with a gearhead having a gear ratio of 100:1 and the newly designed momentum wheel assembly is capable of moving the R-SAT 30 degrees about its roll axis within 3.3 seconds at a maximum rate of 15 degrees per second. Since this is a minimum time problem, the gimbal torque is observed to reach its maximum value. Thus, the time optimal solution trajectory utilizes the full torque capability of the CMG to conduct the maneuver.

B. GIMBAL ASSEMBLY COMPONENTS

Since the gimbal assembly will not be redesigned at this stage in the simulator retrofit, this section describes the parameters and the mechanical characteristics of the current gimbal assembly components which include: the frame, motor, gearhead, absolute optical encoder and slip ring.

1. Frame

The gimbal frame is used to support and house the other gimbal components and the CMG when it is mounted. The gimbal frame is constructed as an assembly using Aluminum 6061 (AL-6061) whose material properties and dimensions are shown in Table 12 and Figure 35.

Parameter	Units	Value
Tensile Strength, Ultimate	MPa	124
Tensile Strength, Yield	MPa	55.2
Modules of Elasticity	GPa	68.9
Poisson's Ratio	GPa	0.33
Shear Modulus	GPa	26

Table 12. Material properties for AL-6061 (After [65])

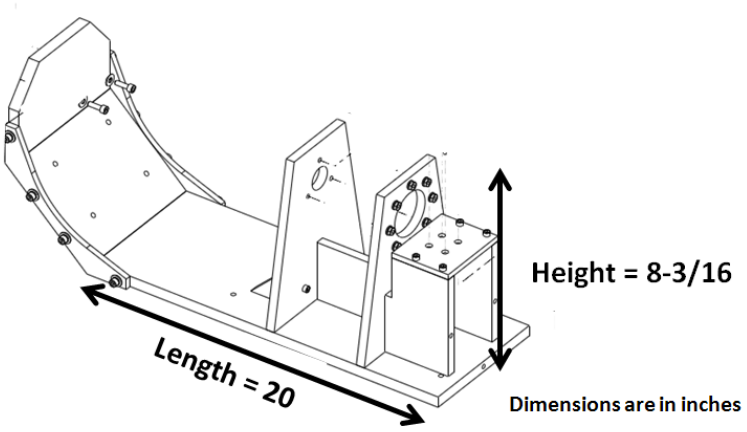

Figure 35. Gimbal frame (After [66])

The material properties and dimensions shown in Table 12 and Figure 35 can be used to conduct further analysis such as a finite element analysis. A finite element analysis was not conducted on the gimbal frame, but could be done in the future to determine the overall performance parameters and limitations of the current gimbal frame and to suggest areas for improvement.

2. Motor

The purpose of the gimbal motor is to rotate the momentum wheel assembly. The current gimbal is powered Emoteq Brushless DC motor. This is the same motor as the original momentum wheel assembly (see Table 3 and Figure 14 for performance

parameters). The results shown in Figure 32 illustrate that the current gimbal motor and gearhead combination are sufficient to operate the R-SAT simulation.

3. Gearhead

The purpose of a gearhead is to reduce the speed of the gimbal motor shaft and transfer it to rotate the CMG wheel. The gimbal has a Harmonic Drive CSG-17–100–2UH series gearhead with a gear ratio of 100:1 whose performance parameters and picture are shown in Table 13 and Figure 36, respectively [34].

Parameter	Unit	Value
Gear Ratio	(-)s	100
Rated Torque at 2,000 rpm	Nm	31
Limit for Repeated Peak Torque	Nm	70
Limit for Average Torque	Nm	51
Maximum Input Speed with Grease	rpm	7,300
Limit for Average Input Speed with Grease	rpm	3,500
Moment of Inertia	$kg \cdot m^2$	0.079e-4
Position Accuracy	arc/min	1.5
Mass	kg	0.68
Basic Life Rate in Hours ($L_{10_{hours}}$)	hours	10,000
Backlash	deg	2.78e-3

Table 13. Harmonic Drive CSG series gearhead performance parameters (After [67])

Figure 36. Harmonic Drive CSG series gearhead (From [68])

The basic life rate for the gearhead and is depend on the angular velocity for which it will be operated. The number of revolutions can be obtained using:

$$L_{10} = L_{10_{hours}}(\omega \bullet 60) \tag{4.10}$$

where $L_{10_{hours}}$ is the basic life rate in hours. The L_{10} for the gearhead operating at 6,500 rpm is 3,900e10^6 revolutions (3,900 million revolutions). Therefore, the gearhead should last 4.5 times longer than the duplex bearing (see Chapter III for bearing calculations). Unfortunately no gearhead is manufactured perfectly and there are small variations which arise from tooth errors and rotation errors (eccentricities) which cause imperfections or errors in the gearhead system [61]. These imperfections can lead to a gearhead that has backlash. Backlash is defined as the amount by which one tooth can move without engaging the tooth on the opposite side (see Figure 37) [61].

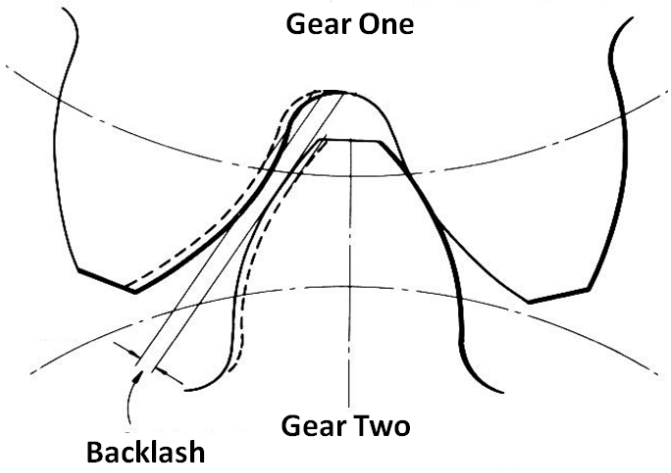

Figure 37. Backlash and backlash allowances (After [31])

Since it is important that the motion be transmitted between shafts with a high degree of angular fidelity, the presence of backlash in the system can limit the performance of speed and position control or even cause a system to behave in an irregular fashion [69]. Therefore, the backlash for the Harmonic Drive CSG series gearhead was examined to determine the effects it would have on the performance of a newly designed CMG.

A 2002 survey paper by Nordin and Gutman summarized two models for controlling the effects of backlash on a mechanical system: the dead zone model and the non-zero shaft damping model. The dead zone model is only valid for system whose shafts have zero damping or is an elastic shaft. In order for a shaft to have zero damping it must act as a pure spring which means that the shaft torque is proportional to the shaft twist [69]. Since the gimbal shaft is stainless steel, it cannot accurately be modeled as a spring. Therefore, the CMG system was first examined using the non-zero shaft damping model shown in Figure 38 [69].

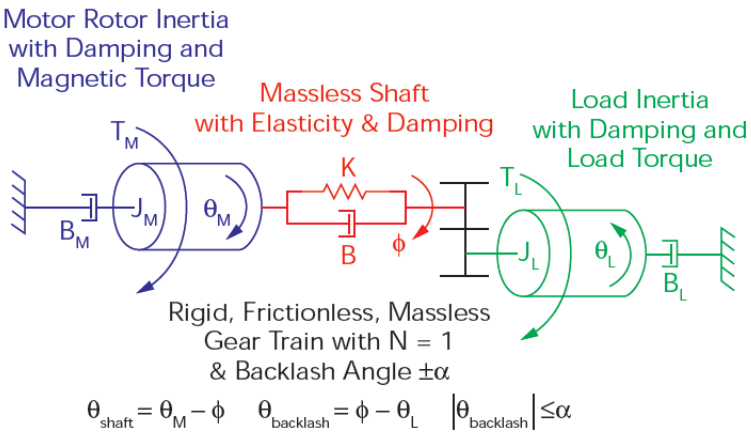

Figure 38. Two-mass system with backlash (From [70])

The mechanical model shown in Figure 38 represents a mechanical system with a gear ratio of 1:1 and does not represent our specific system that has gear ratio of 100:1. However, our analysis assuming a 1:1 gear ratio enables a basic understanding of the effects of backlash on the operation of the gimbal to be obtained.

The system equations of motion for Figure 38 are represented by Equation (4.10)-Equation (4.16). The dynamics for the motor are defined by:

$$J_m\ddot{\theta}_M + B_M\dot{\theta}_M = T_M - T_S \tag{4.11}$$

where J_m is the motor rotor inertia, $\ddot{\theta}_M$ is the angular acceleration of the motor rotor, B_M is the viscous load friction of the motor, $\dot{\theta}_M$ is the angular velocity of the motor rotor, T_M is the motor torque and T_s is the torque transmitted through the shaft. As the motor twists there is a displacement between the angle of the motor shaft and the shaft, this relationship is defined by:

$$\dot{\theta}_D = \dot{\theta}_M - \dot{\theta}_L \tag{4.12}$$

where $\dot{\theta}_D$ is the angular velocity of the displacement angle and $\dot{\theta}_L$ is the angular velocity of the load or the rate at which the load is twisting per unit time. The dynamics of the shaft are defined by:

$$T_{sc} = B_s\dot{\theta}_D + K\ \theta_D \tag{4.13}$$

where T_{sc} is the nominal transmitted shaft torque without backlash, B_s is the inner Damping Coeffient of the Shaft, K_s is the shaft elasticity and θ_D is the displacement angle between the motor shaft. The dynamics of backlash on the system is defined as:

$$T_{sb} = B_s\dot{\theta}_b + K_s\theta_b \tag{4.14}$$

where T_{sb} is the torque removed from the system due to backlash. The actual transmitted shaft torque is a function of the nominal transmitted shaft torque and the negative effects of backlash (see Equation 4.13).

$$T_S = T_{sc} - T_{sb} \tag{4.15}$$

where T_S is the shaft torque that is actually transmitted to the load. The load (CMG gimbal) dynamics are defined by:

$$J_L\ddot{\theta}_L + B_L\dot{\theta}_L = T_S - T_L \tag{4.16}$$

where J_L is the load inertia, $\ddot{\theta}_L$ is the angular acceleration of the load, B_L is the viscous load friction of the load, $\dot{\theta}_L$ is the angular velocity of the motor rotor and T_L is the load torque. The equations of motion were implemented into the Simulink model (Figure 39) with the addition of a PI controller.

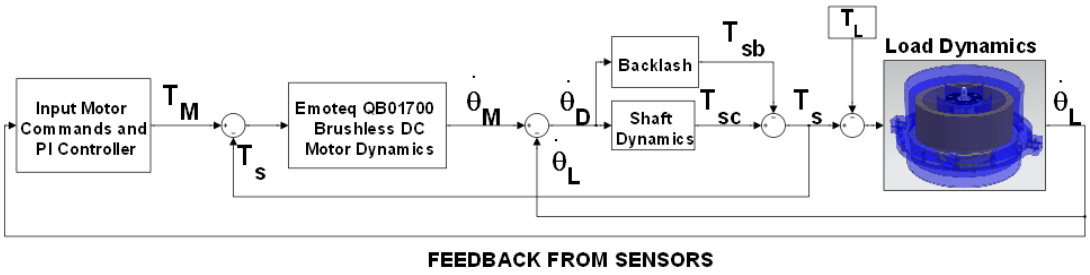

Figure 39. Two-mass system with backlash and gear ratio of 1

The elasticity and viscous load friction of the loads for the motor, shaft and load are not explicitly shown in Figure 39, but are embedded within their respective dynamics block, i.e., the shaft elasticity and viscous load friction of the loads are embedded within the shaft dynamics block. The input parameter was a 0.1 Nm step response. The other parameters for the model are shown in Table 14. The results for the simulation are shown in Figure 40 and Figure 41.

Parameter	Unit	Value
Motor Rotor Inertia	$kg \cdot m^2$	0.4
Viscous Load Friction of the Motor	Nm/(rad/sec)	0.1
Shaft Elasticity	Nm/rad	3,300
Inner damping coeffient of the shaft	Nm/(rad/sec)	1
Load Inertia	$kg \cdot m^2$	5.6
Viscous Load Friction of the Load	Nm/(rad/sec)	1
Backlash	deg	1
Proportional Gain	(-)	38
Integral Gain	(-)	0.35

Table 14. Nominal case Simulink input parameter (After [69])

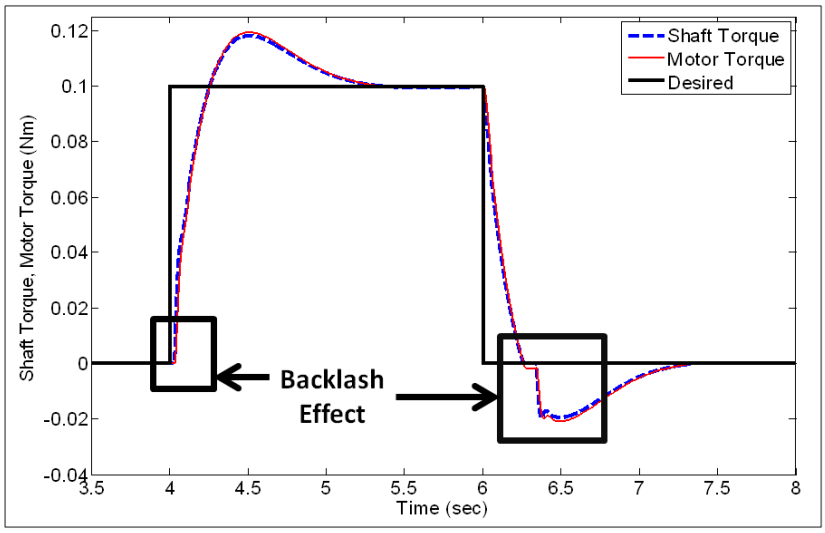

Figure 40. Torque response for step input with PI-controller and 1 degree backlash

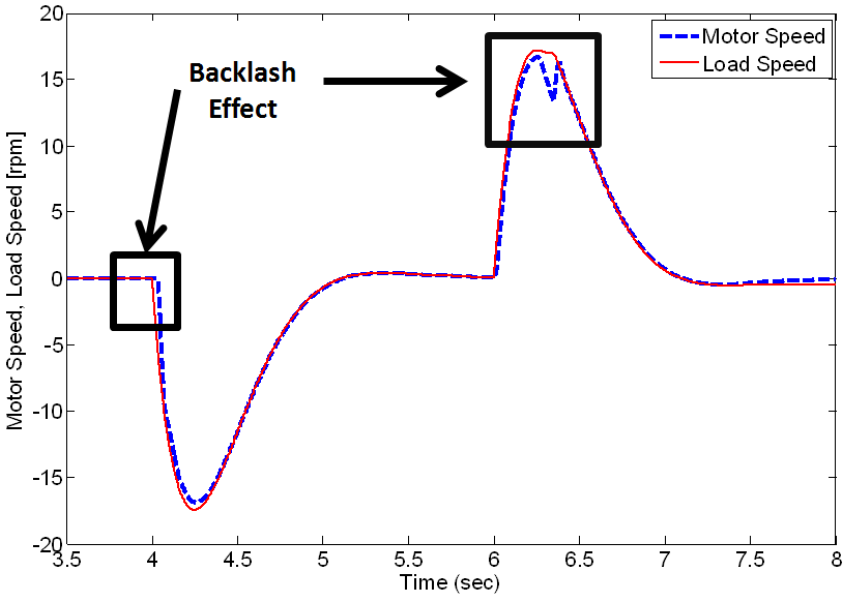

Figure 41. Velocity response for step input with PI-controller and 1 degree backlash

The simulation results show that backlash affects the gimbal shaft initially when conducting maneuvers and especially when the gimbal shaft is changing directions. The effects of backlash become negligible as the system reaches steady state. However, the gimbal shaft must change direction in order to control the spacecraft (see Figure 33). Therefore, the presence of backlash can degrade the performance of the CMG system.

The backlash analysis was then conducted for the current gimbal assembly with a gear ratio of 1:1 (assumed for convenience). The gimbal shaft is made of SST-304 (see Table 9 for material properties). The design parameters for the gimbal shaft calculated using the equations in Chapter III and are shown in Table 15. The model parameters are for the newly design CMG system backlash simulation analysis are shown in Table 16.

Parameter	Units	Value
Diameter	mm	12.7
Length	mm	98.5
Polar Moment of Inertia	mm^4	2.55e3
Shaft Stiffness	Nm	2.22e6
Maximum Twist Angle	rad	3.69e-4
Maximum Shear Stress	N/mm^2	15.86
Shaft Elasticity	Nm/rad	2.23e6

Table 15. Gimbal shaft design parameters

Parameter	Unit	Value
Motor Rotor Inertia	$kg \cdot m^2$	1.1e-6
Viscous Load Friction of the Motor	Nm/(rad/sec)	5.55e-8
Shaft Elasticity	Nm/rad	2.55e6
Inner damping coeffient of the shaft	Nm/(rad/sec)	1
Load Inertia	$kg \cdot m^2$	0.033
Viscous Load Friction of the Load	Nm/(rad/sec)	1
Backlash	deg	2.78e-3

Table 16. Input parameter for backlash Simulink model

The Simulink model (Figure 39) for a two-mass system with non-zero shaft damping and a PI controller is not an acceptable model for the current gimbal assembly and the newly designed momentum wheel assembly. This is because the load inertia (see Table 16) is considerably higher (30,000 times greater) than the motor inertia and the stability margins of the system become unacceptable [69]. This instability can be corrected by adding a notch filer, a higher order controller to the control system or using a motor with a higher inertia. Since development of the gimbal control logic is not the focus of this thesis, additional analysis was not performed, but is left instead as future work.

4. Digital Absolute Optical Encoder

The purpose of the encoder is to provide position and velocity feedback on the gimbal shaft as it is rotating. The gimbal assembly is equipped with an Allied Motion CP-550–16S-1/2 digital absolute optical encoder whose performance parameters and picture are shown in Table 17 and Figure 42, respectively.

Parameter	Units	Value
Bit Count	Bit	16
Shaft Bore Size	inch	0.5
frequency Response	kHz	100
Accuracy	arcsec	±12
Power Supply (	VDC	±5
Maximum Speed	rpm	10,000
Resolution	cycles per revolution	up to 2,048
Type	N/A	Digital

Table 17. Allied Motion CP-550–16S-1/2 absolute optical encoder performance parameters (After[34])

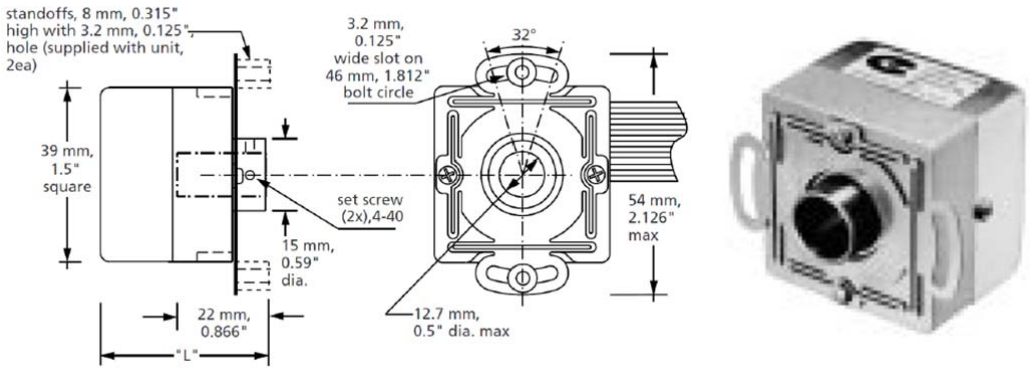

Figure 42. Allied Motion CP-500 series absolute optical encoder (After [71])

An absolute encoder has a unique code for each position, so it has the ability to know the location of the shaft without having to be reset to a nominal value [72]. Allied motion has since changed their model numbering and are no longer producing the CP-550–16S-1/2 encoder. An acceptable replacement encoder is Dynapar AI25–1217–3-5-A-0-D whose performance parameters and picture are shown in Table 18 and Figure 43.

Parameter	Units	Value
Bit Count Multi-Turn	Bit	12
Bit Count Multi-Turn	Bit	17
Shaft Bore Size	inch	0.5
frequency Response	kHz	500
Absolute Accuracy	arcsec	36
Power Supply	VDC	5
Maximum Continuous Speed	rpm	10,000

Table 18. Dynapar AI25–1217–3-5-A-0-D absolute encoder performance parameters (After [73])

Figure 43. Dynapar absolute encoder (replacement for the original encoder)

5. Slip Ring

The purpose of the slip ring is to route electrical wires for the momentum wheel assembly in order to prevent them from getting twisted or damaged while the momentum wheel assembly is rotated (see Figure 44).

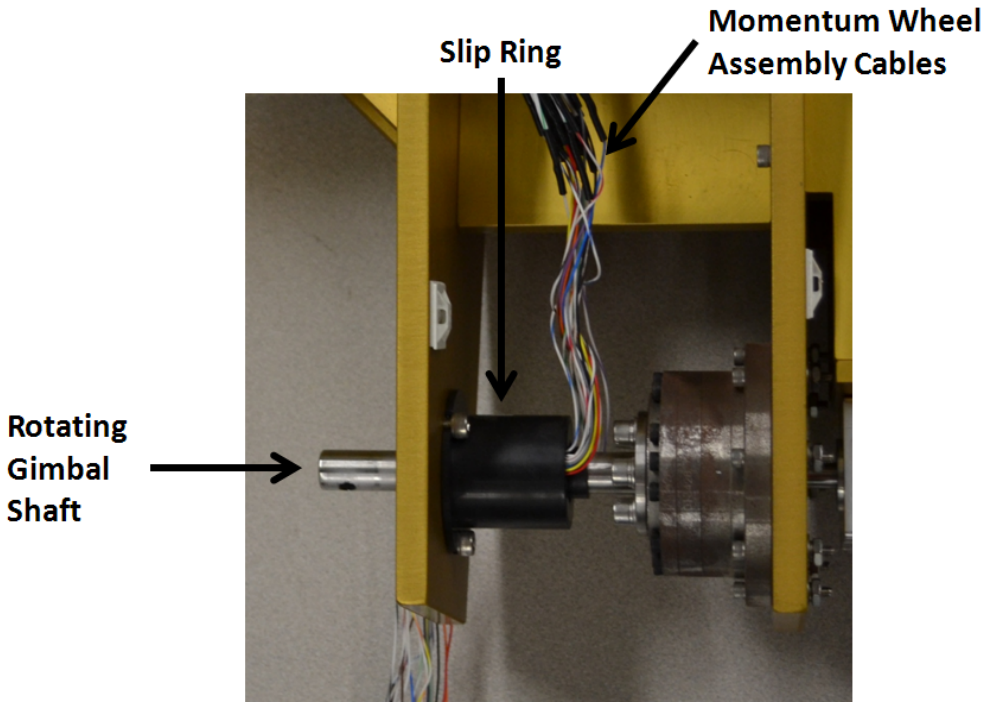

Figure 44. Slip ring location on gimbal assembly

The current gimbal assembly has one MOOG SRA-73683–18 slip ring whose specifications and picture are shown in Table 19 and Figure 45, respectively.

Parameters	Unit	Value
Number of circuits	(-)	18
Through-bore	in	0.5
Maximum Continuous Operating Speed	rpm	120
Voltage	VAC	210
Current Rating	A	2

Table 19. MOOG SRA-73683–18 slip ring specifications (After [74])

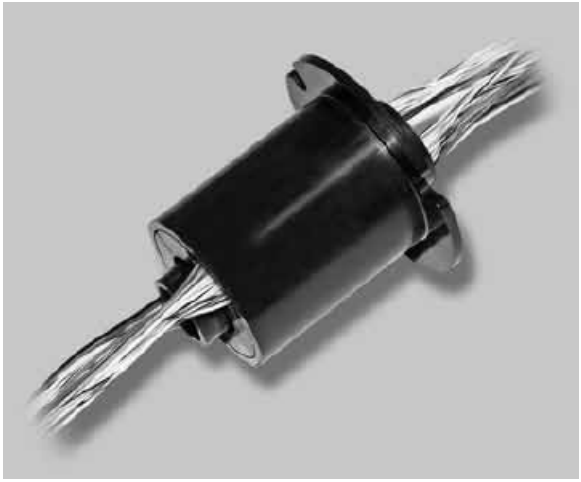

Figure 45. MOOG SRA-73683–18 slip ring (From [74])

V. MANUFACTURING, INTEGRATION AND BALANCING

This chapter discusses the details of the CMG manufacturing process, integration of the CMG components and balancing of the CMG the momentum wheel.

A. MANUFACTURING

The manufacturing of the momentum wheel assembly components is just as important as the design. For example, if any of the components were manufactured poorly or not to specification than the assembly might not fit together, may not operate properly, may fail early or may not work at all. That is why it is important for the designer and manufacturer to discuss the overall concept of the design and resolve any potential issues prior to any material being cut.

Immediately after the first prototype was completed, the manufactures (Inter-City Manufacturing, Sand City, CA) who became a part of the momentum wheel assembly design team. Design meetings were regularly scheduled with the machinists in order to ensure that the parts could be manufactured to the design specifications. The machinists not only manufactured the components, but also actively participated in the design process. For example, the manufacturer suggested design changes for some design configurations that were easy enough to develop using the CAD program, but would be impossible to manufacture. Once the final design was settled upon, the manufacture of the components was completed using various manufacturing techniques and machines such as the Fanuc Series 16 Computer Numerical Control (CNC) machine. Figure 46 shows the motor side case being manufactured at Inter-City Manufacturing in the CNC machine. The design process concluded with the completed final momentum wheel assembly prototype (see Figure 47). The integration of the all of the components shown in Figure 47 are discussed in the following sections.

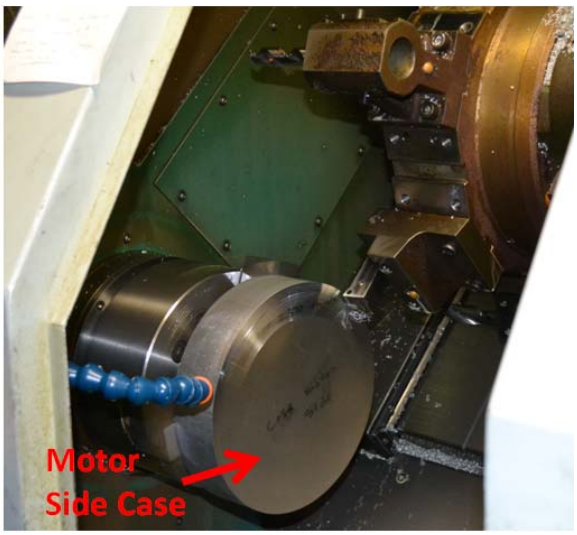

Figure 46. Fanuc Series 16 CNC machine

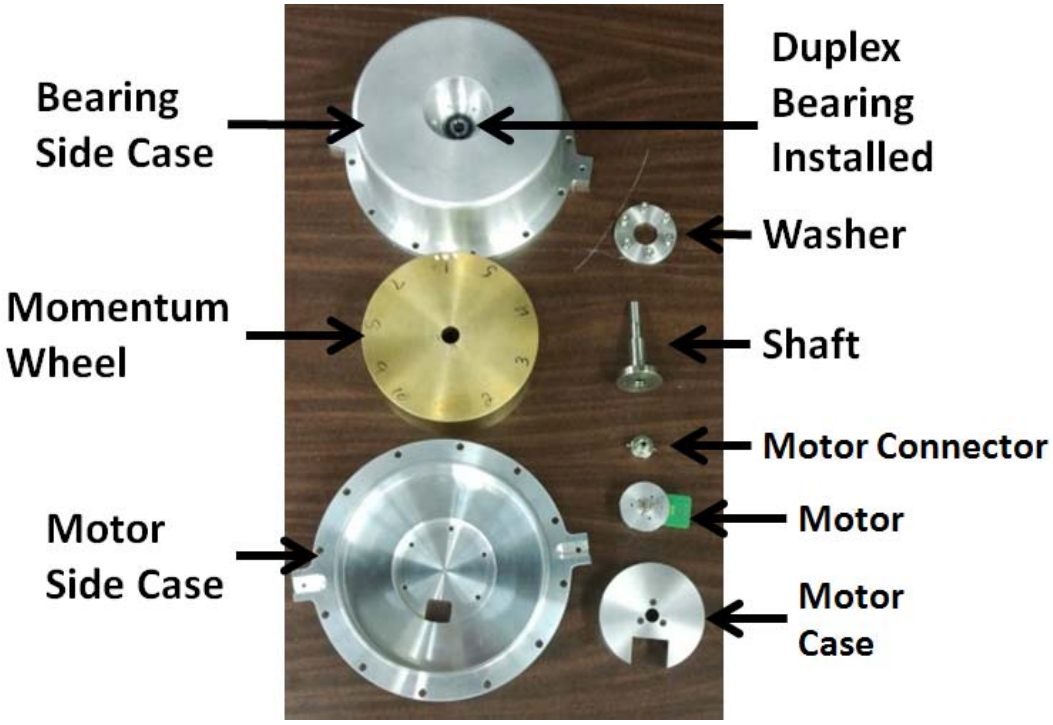

Figure 47. Final prototype components

B. INTEGRATION OF THE MOMENTUM WHEEL ASSEMBLY

1. Momentum Wheel and Shaft Integration

The momentum wheel and shaft are integrated using a transitional fit and two dowel pins (see Figure 48 and Figure 49). A transitional fit allows for very little clearance between the two components and is the closest fit that will allow easy disassembly by hand. This type of connection permits the two parts to be repaired or replaced easily [75]. A press fit or interference fit on the other hand has no clearance between the components. In fact an interference fit requires that one of the components be thermally expanded or cooled in order to integrate them together [75]. A interference fit cannot be disassembled easily and requires the components to be heated or cooled again. Moreover, the thermal process can distort the alignment between each of the parts. This is not desirable for a high speed rotor. Therefore, interference fits were not used for the prototype. Instead, the dowel pins, the wide shoulder area of the wheel shaft and the locking nut helps to maintain the alignment of the momentum wheel and shaft.

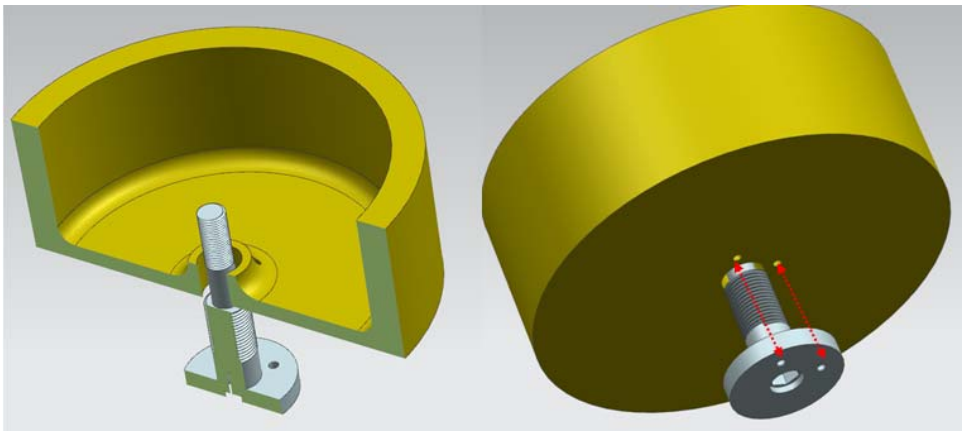

Figure 48. Momentum wheel and shaft integration CAD model

Figure 49. Momentum wheel and shaft integration

2. Shaft and Motor Connector Integration

The shaft and motor connector are integrated using a hex key coupling. The hex key coupling allows for easy disassembly of the components, but still give a good connection between the wheel and the motor shafts (see Figure 50 and Figure 51) Due to manufacturing tolerance, there exists some play between the motor connector and the shaft. This did not appear to cause any issues when the CMG was spun up. Some chatter can, however, be heard when the CMG is gimbaled. It is expected that this is more a nuisance than a series design flaw. This can also be corrected with further iterations by manufacturing the shaft and motor connector as one piece.

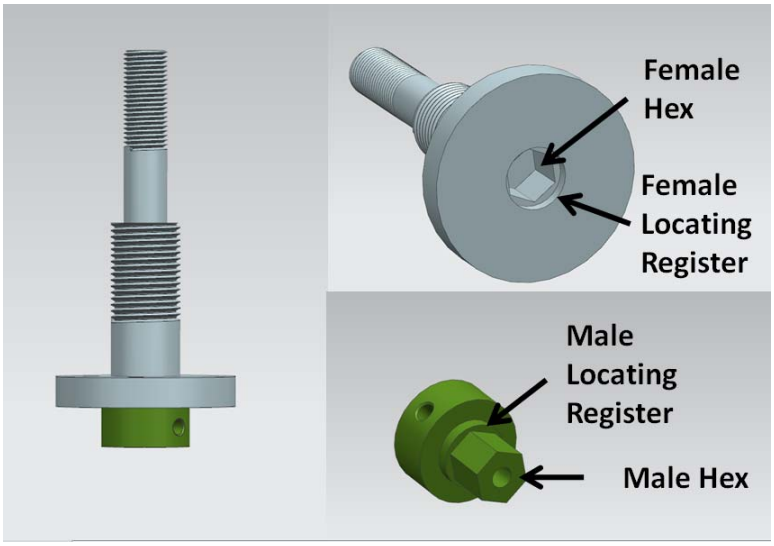

Figure 50. Shaft and motor connector integration CAD model

Figure 51. Shaft and motor connector integration

3. Motor and Motor Case Integration

The motor case securely connects to the motor using three screws and the locating register. There is also a gap for the motor electrical connector and a locating register for the lip around the motor shaft (Figure 52 and Figure 53). The motor locating register ensures precise alignment of parts.

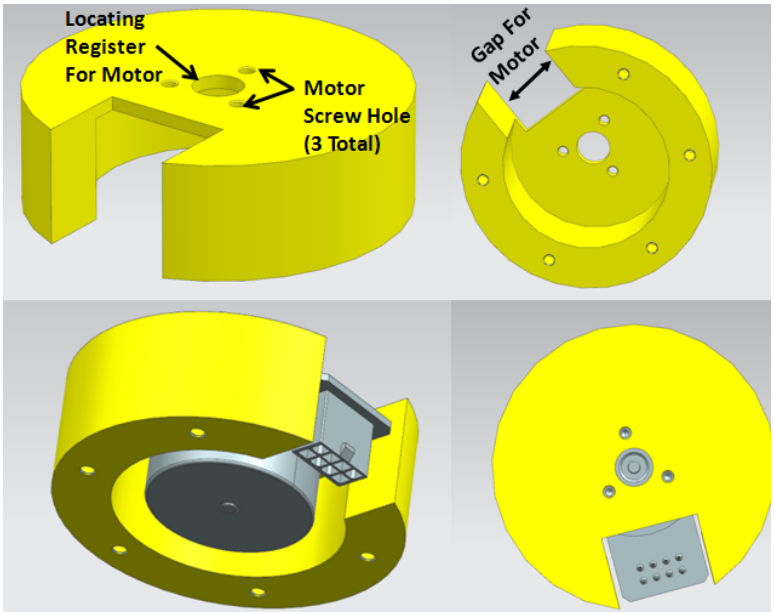

Figure 52. Motor and motor case integration CAD model

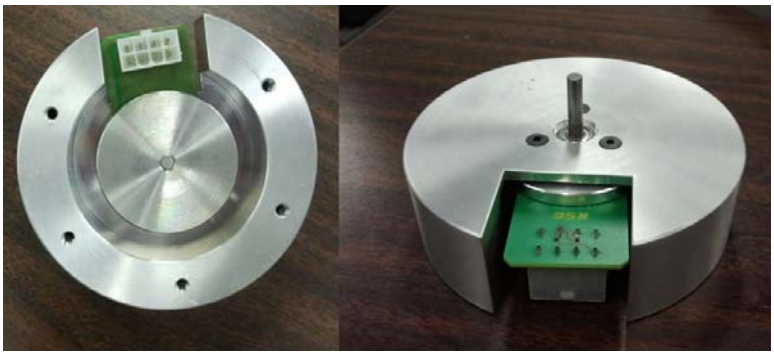

Figure 53. Motor and motor case integration

4. Motor Case and Motor Side Case Integration

The motor case and motor side case are integrated using five screws and a locating register (Figure 54 and Figure 55). The locating register allows the motor shaft to be aligned with the other momentum wheel assembly components. Therefore, no measurements need to be made when assembling the motor to the motor case.

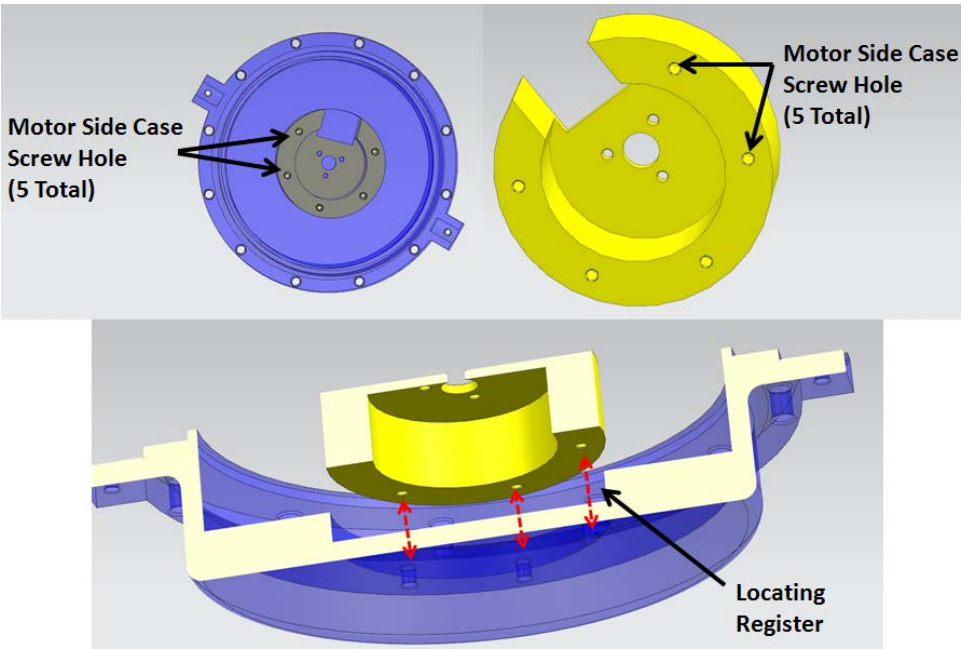

Figure 54. Motor case and motor side case integration CAD model

Figure 55. Motor case and motor side case integration

5. Motor and Motor Connector Integration

The motor and the motor connector are integrated using two set screws (see Figure 56 and Figure 57), once the motor has been mounted in the motor case. The motor case is removed from the CAD models and picture for clarity. The vertical location of the motor connector with respect to the motor needs to be accurate because it will affect the vertical alignment of the other momentum wheel assembly components and can cause unwanted stress and loads. The desired vertical position was measured using the CAD model assembly to be 0.116 inches from the face of the motor case. The actual desired vertical distance was obtained from the manufacturers as 0.114 inches. (see Figure 58). During assembly this value can be set using a feeler gauge (see Figure 59). At no time during assembly should the connector be any further from the motor than 0.114 inches, it better to have a slightly smaller gap between the components then it is to have them rub together.

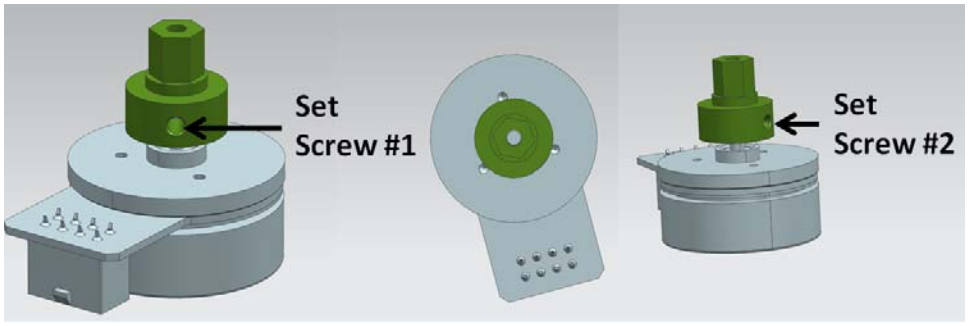

Figure 56. Motor and motor connector integration CAD model

Figure 57. Motor and motor connector integration

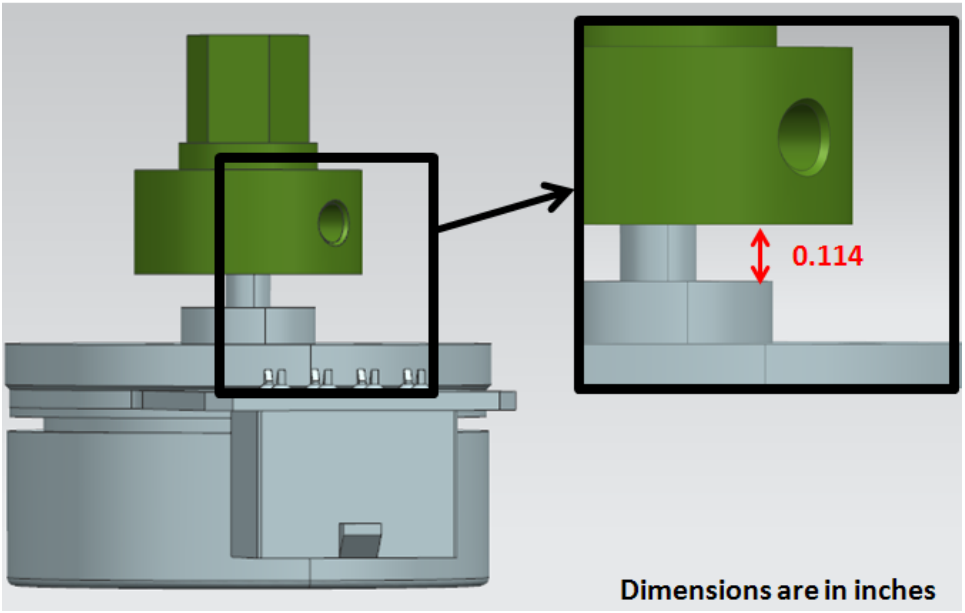

Figure 58. Motor connector positioning CAD model

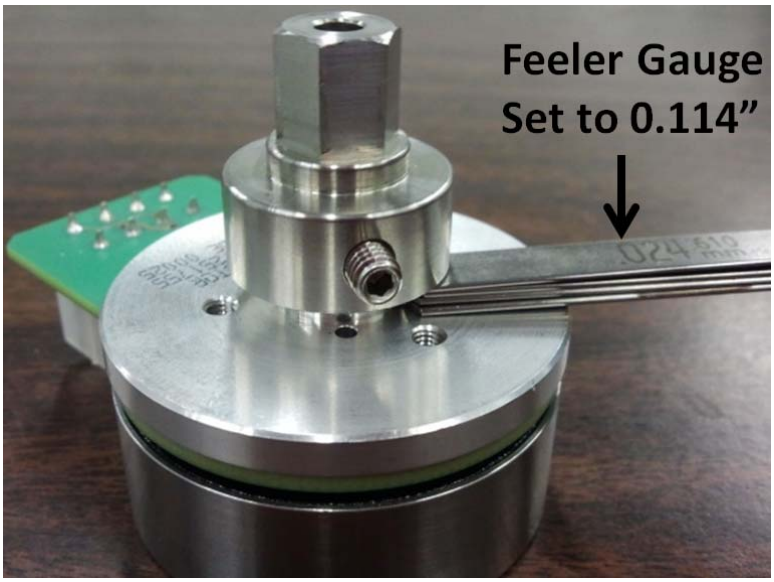

Figure 59. Motor connector positioning

6. Duplex Bearing and Bearing Side Case Integration

The duplex bearing is housed within the bearing side case (see Figure 60 and Figure 61). Since the bearing side case was designed to house the duplex bearing, it the needed to be able to properly preload the bearing. Recall, that proper preloading of the angular contact bearing is very critical for the operation of the CMG. Preloading is done by adding an axial load with the correct amount of force. So it important to have the bearing housing made to the correct specifications. The bearings required a housing tolerance of only 0.006 mm; which is a tight tolerance. With that in mind, the bearing side outer casing was designed to house the bearing. This means that the manufacturing of the case was now even more critical for the design. The preloading of the inner bearing race was achieved by placing a threaded lock nut on the shaft and tightening the assembly so as to apply 20 N of force (see Figure 62). The bearing washer was designed to hold the duplex bearing in place and is integrated to the case using 5 screws.

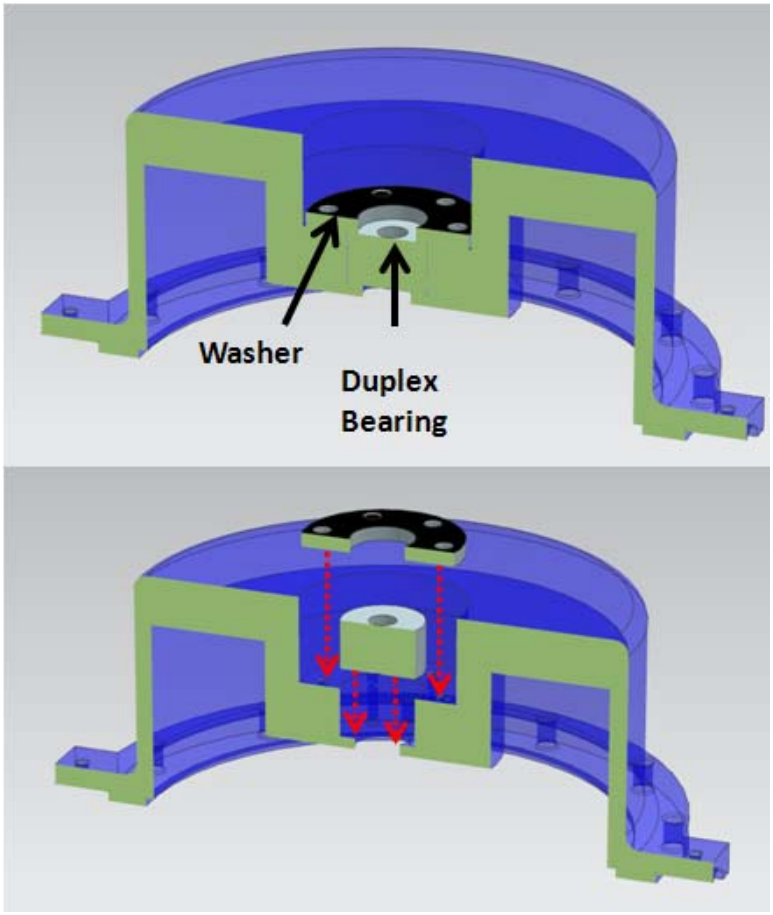

Figure 60. Bearing side case and duplex bearing integration CAD model

Figure 61. Bearing side case and duplex bearing integration

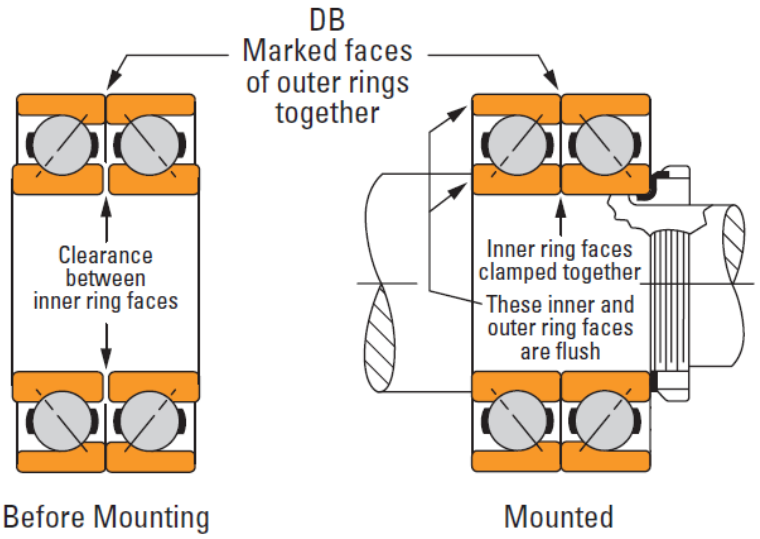

Figure 62. Timken duplex bearing configuration (From [52])

The bearing was mounted inside the bearing side case by heating the casing to thermally expand it enough to place the bearing inside. When the casing cools the outer race of the bearing would be properly preloaded and mounted inside the casing. This step is very important in the manufacturing process because if not done properly could lead to cramping of the bearing, abnormal increase in preloading leading to overheating and bearing failure [52].

C. MOMENTUM WHEEL ASSEMBLY BALANCING

When assembled, the momentum wheel assembly consists of a rotor assembly including all of the rotating components such as the momentum wheel, the shaft, the motor connector, the bearing and the motor (see Figure 63).

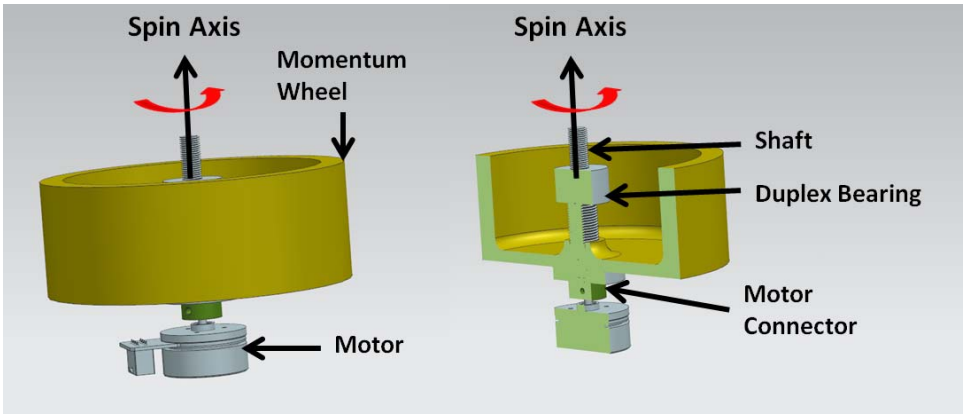

Figure 63. Final prototype rotor assembly

The MOI and angular momentum for the complete rotor assembly was calculated using NX I-DEAS 6.1 and the maximum angular momentum was calculated using Equation (1.2). The resulting values are listed in Table 20.

Parameter	Unit	Value
Maximum Angular Velocity	rpm	6,500
Maximum Angular Velocity	rad/sec	680.68
MOI Rotor Assembly	kg-m^2	0.0105
Maximum Rotor Assembly Angular Momentum	N·m·sec	7.14

Table 20. Final prototype momentum wheel assembly performance parameters using no load speed

Since the momentum wheel will be spinning at very high rates (6,500 rpm), it is important that the rotating mass be balanced. An object is considered unbalanced when there is an uneven distribution of weight or mass around the center of rotation. The force associated with the unbalance is proportional to the square of the angular rotation speed [76]. In addition to the rotation speed, the unbalance of a rotating mass is also highly dependent on geometry, mass and material properties [77]. The entire rotor assembly (see Figure 63) was not balanced as an assembly because the components are not permanently

fixed together i.e., the components do not have an interference fit. Instead, each of the components was examined for unbalance individually. As a result of the examinations, it was found that the momentum wheel was the only component that required balancing.

1. Procedure for Balancing

The momentum wheel was balanced to the International Organization for Standardization 1940–1 (ISO 1940–1) balance quality of 1.0 (G 1.0). The ISO 1940–1 is the Mechanical Vibration: Balance Quality Requirements for Rotor in a Constant (rigid) State and is a common standard used for balancing within the mechanical engineering and manufacturing communities [76]. The ISO balance quality grades for different types of rigid rotors are shown in Table 21.

Balance Quality Grade	Rotor Types Examples
G 6.3	- Parts of process plant machines - Marine main turbine gears (merchant service) - Centrifuge drums - Paper machinery rolls; print rolls - Fans - Assembled aircraft gas turbine rotors - Flywheels - Pump impellers - Machine-tool and general machinery parts - Individual components of engines under special requirements
G 2.5	- Gas and steam turbines, including marine main turbines - Rigid turbo-generator rotors - Computer memory drums and discs - Turbo-compressors - Machine-tool drives - Turbine-driven pumps
G 1.0	- Tape recorder and phonograph (gramophone) drives - Grinding-machine drives - Small electric armatures with special requirements
G 0.4	- Spindles, discs and armatures of precision grinders - Gyroscopes

Table 21. ISO balance quality grades for rigid rotors (After [78])

The wheel was balanced to G 1.0, since it is a proof of concept prototype. However, further iterations of the momentum wheel assembly should be balanced to G 0.4 to be within ISO standards for a gyroscope. Under the ISO 1940/1, the allowable permissible unbalance of the rotor can be calculated using Equation (5.1) or obtained using Figure 64. The permissible unbalance is given as:

$$U_{per} = 170.5 \cdot G \cdot \frac{W_{lbs}}{n} \tag{5.1}$$

where U_{per} is the permissible residual unbalance in gram-inches, G is the balance quality grade, W_{lbs} is the weight of the object being balanced in lbs, and n is the maximum angular velocity for which the object will be rotated in rpm's.

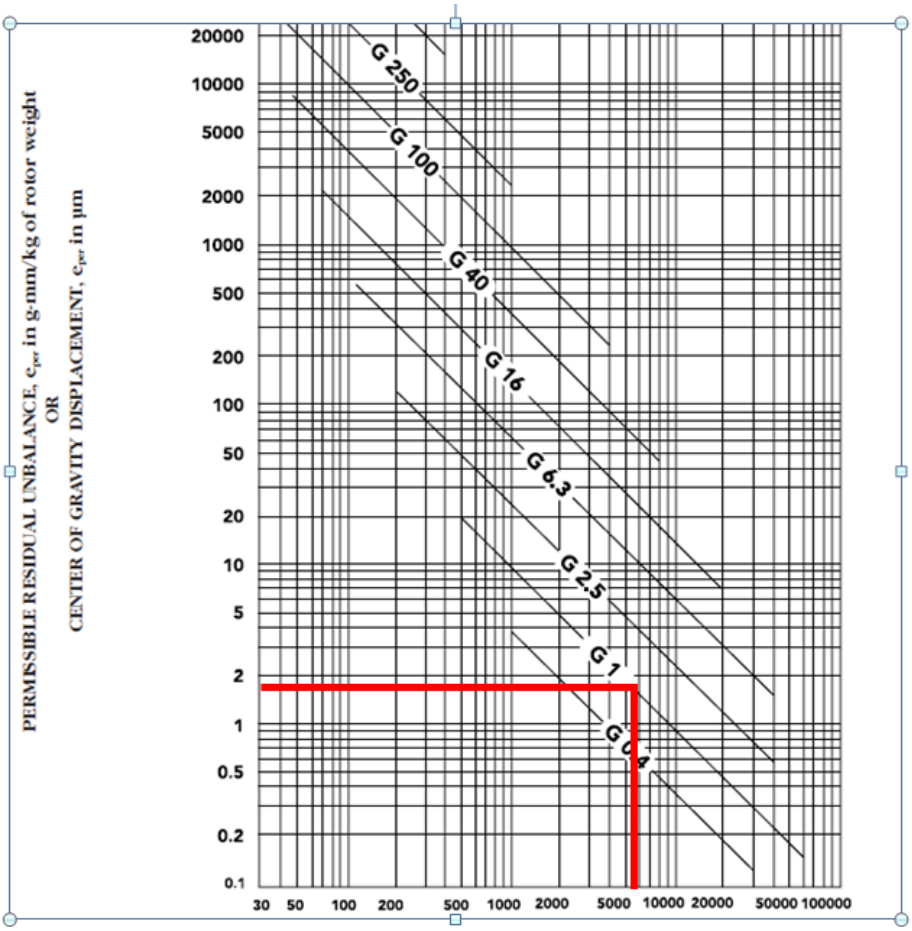

Figure 64. Balancing specification chart (After [78])

The allowable permissible unbalance for the rotating mass with one correction plane was found to be 0.21 gram-inches using Equation (5.1) and 0.237 gram-inches using Figure 64. The value obtained using Equation (5.1) is a more accurate and conservative number, so it was the value used to conduct the remaining balancing calculations. The momentum wheel has two balancing planes (see Figure 65) which is referred to as dynamic balancing where the unbalance is expressed in terms of the permissible unbalance or correction weight and a radius per plane [76].

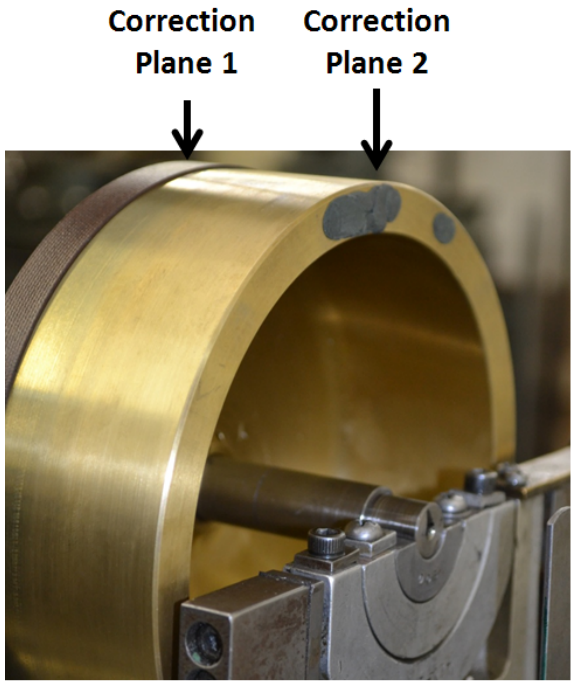

Figure 65. Wheel with allowable permissible unbalance mass

The momentum wheel dynamic balancing required that the correction weight be divided in half between the two planes and then divided by location radius of the correction weight. The radius is dependent on the wheel configuration and was found to be 2.75 inches. Therefore, the correction weight for each plane was 0.038 gram-inches (see Figure 66).

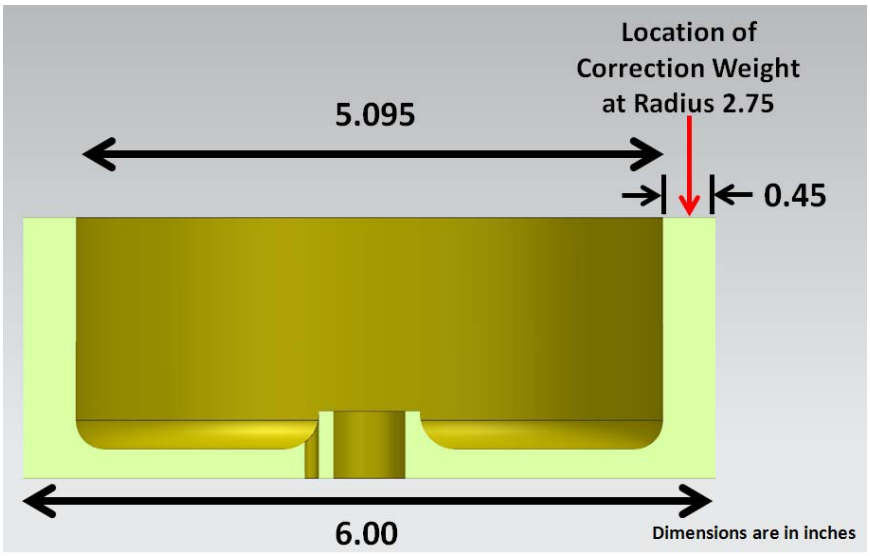

Figure 66. Correction weight location for momentum wheel

The momentum wheel with proper correction weight was then placed on a balancing machine, where it would be rotated in order to determine the amount of unbalance (see Figure 67).

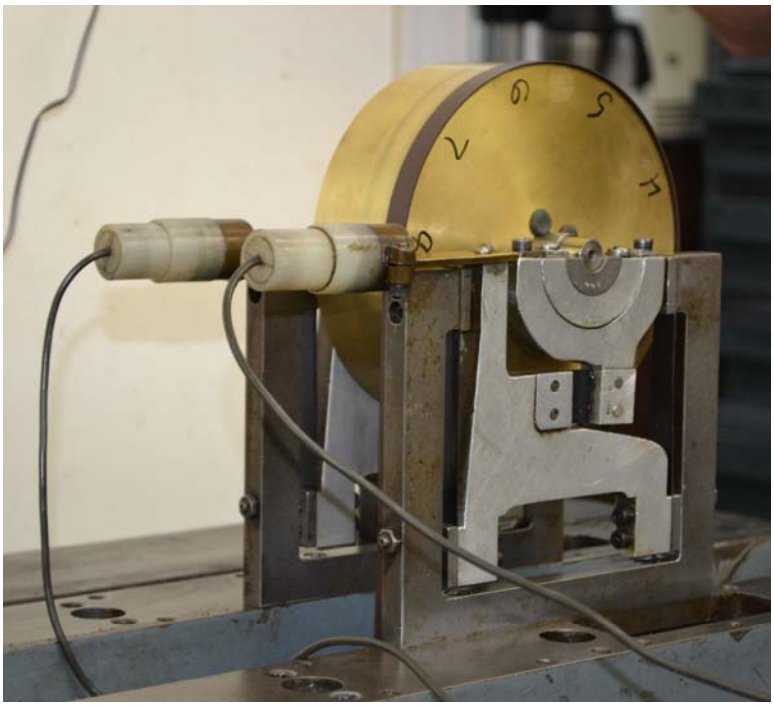

Figure 67. Wheel on balancing machine

The balancing machine is essentially a force sensor which measures the unbalance force created by the wheel as it is rotated. The unbalance force can be written as:

$$F_{unbalance} = m_{unbalance} \cdot d \cdot \omega^2 \tag{5.2}$$

where $m_{unbalance}$ is the mass of the unbalance mass, d is the distance from the unbalance mass to the centerline of the wheel and ω is the angular velocity of the wheel [77].

The balancing machine must first be calibrated using the G 1.0 correction weight. This is done by rotating the wheel with the correction weight and setting the balancing machine value to a set number such as 1.0. This is to calibrate the balancing machine to G 1.0. The correction weight is then removed and the wheel is rotated again. The desired result is for the output of the balance machine number to remain the same. If the balance machine reads a number less than 1 the wheel is balanced better than G 1.0 standards and does not require any alternations. However, if the number is higher than 1 the wheel is not with G 1.0 standards and the additional mass can then be removed from the wheel using a drill (see Figure 68).

Figure 68. Image of the wheel being drilled

Since the values of unbalance were so small only small amount of the wheel's mass were removed at a time. Then the wheel would be placed back on to the balancing machine to re-check the value of unbalancing; this procedure was repeated until the wheel's rotational imbalance was with the allowable permissible unbalance specifications. The momentum wheel was balanced to ISO 1940/1 G 1.0, but the overall entire assembly cannot be certified to G 1.0 since it was not balanced as a complete assembly. The amount of imbalance in the momentum wheel assembly was also tested after integration using an accelerometer and the results are discussed in Chapter VI.

D. GIMBAL AND MOMENTUM WHEEL ASSEMBLY INTEGRATION

The momentum wheel assembly is integrated with the gimbal assembly using a 1/2 inch gimbal shaft and slotted spring pin (see Figure 69 and Figure 70). Once the momentum wheel assembly is integrated with the gimbal, there are a total of twelve screws that are used to secure the bearing side and the motor side case together. The screws should be secured in a diagonal sequence and it is important that all twelve are in place and torqued to the same specification before using the CMG.

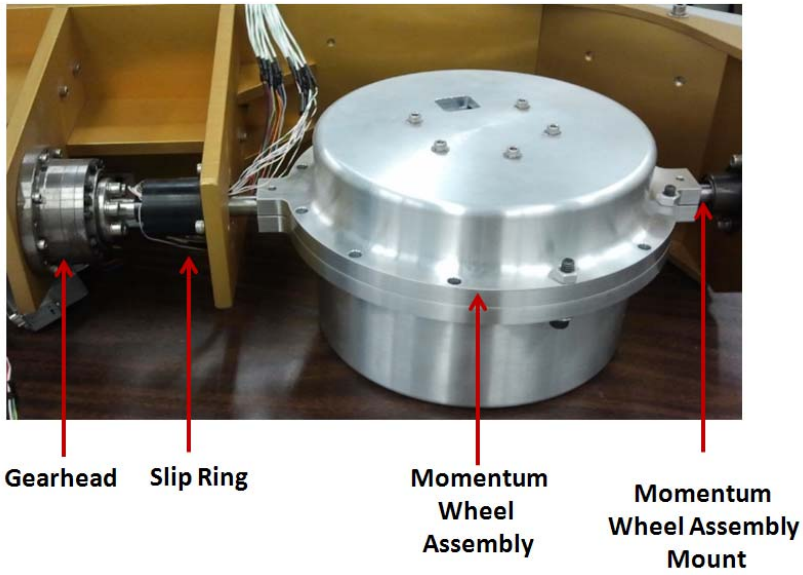

Figure 69. Gimbal and momentum wheel assembly integration

Figure 70. Gimbal and momentum wheel assembly integration

THIS PAGE INTENTIONALLY LEFT BLANK

VI. TESTING AND EVALUATION

A. INTRODUCTION

The momentum wheel assembly was tested separately from the gimbal assembly prior to integrating the complete CMG. Since the development of open-architecture electronics is beyond the scope of this thesis, the prototype momentum wheel assembly was tested using a COTS electronics setup including a motor controller, power supply and associated software. This chapter contains the initial testing of the momentum wheel assembly. The gimbal assembly and the complete CMG system was not tested during this thesis.

B. MOMENTUM WHEEL ASSEMBLY TESTING

The momentum wheel assembly was tested using an external power supply, a BDLC motor controller, Maxon EPOS studio, an accelerometer and a computer (see Figure 71).

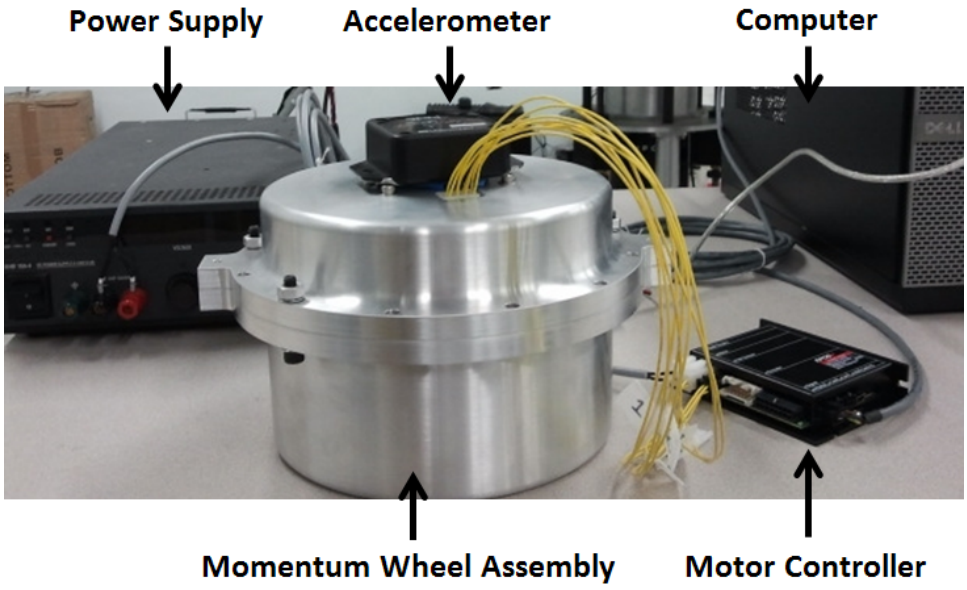

Figure 71. Experimental set up

The experimental setup in Figure 71 was used to determine the maximum achievable angular velocity of the prototype momentum wheel assembly. The wheel was oriented such that the duplex bearing was loaded axially. The motor was operated using a Maxon EPOS2 24/5 position/velocity controller (see Figure 72).

Figure 72. Maxon EPOS 24/5 position/velocity controller

The EPOS2 24/5 controller is a full digital smart motion controller that allows for the user to communicate and control EPOS enabled devices. The motor controller was connected to a computer using RS232 connector and was programed through the EPOS Studio software; which provided the capability for automatic gain tuning and standard motion control such as position, homing, profile velocity, position, profile velocity and current modes [79].

The motor gains was tuned using the EPOS studio auto regulation tuning with the load (momentum wheel assembly) detached from the motor. The auto regulation tuning allows for three essential regulation structures to be tuned: the current control loop, the position control loop, and the velocity control loop [80]. The block diagram for current regulation, velocity regulation and position regulation structures are shown in Figure 73, Figure 74 and Figure 75, respectively. As can be seen, the motor controller uses a relatively simple inner-outer loop control structure to operate the motor in either position or velocity mode.

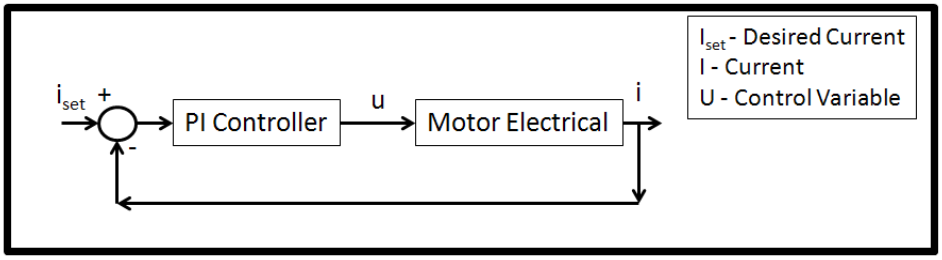

Figure 73. Current regulation block diagram (After [80])

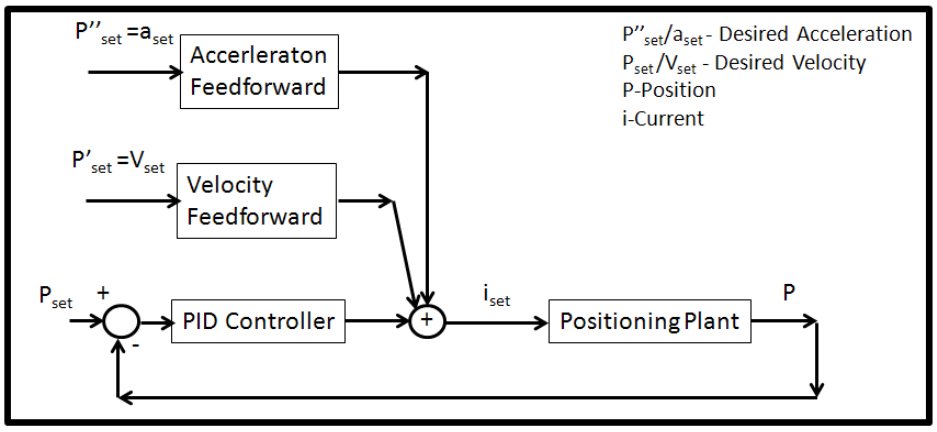

Figure 74. Velocity regulation block diagram (After [80])

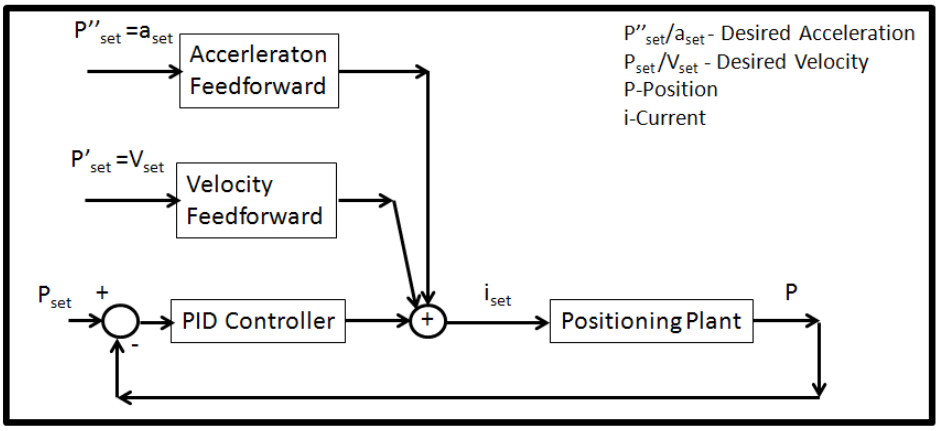

Figure 75. Position regulation block diagram (After [80])

The auto tuning algorithm is a simple and quick way to tune the regulation gains, but to achieve an optimum regulation behavior a more detailed tuning should be conducted such as the EPOS expert tuning mode should be completed. Alternatively, a

tuning calculation for the motor/motor controller system. This was not conducted during the time of this thesis, but should done with further iterations in order to optimize the CMG control system. A plot of the regulation tuning results and the auto tuning gains are shown in Figure 76 and Table 22, respectively.

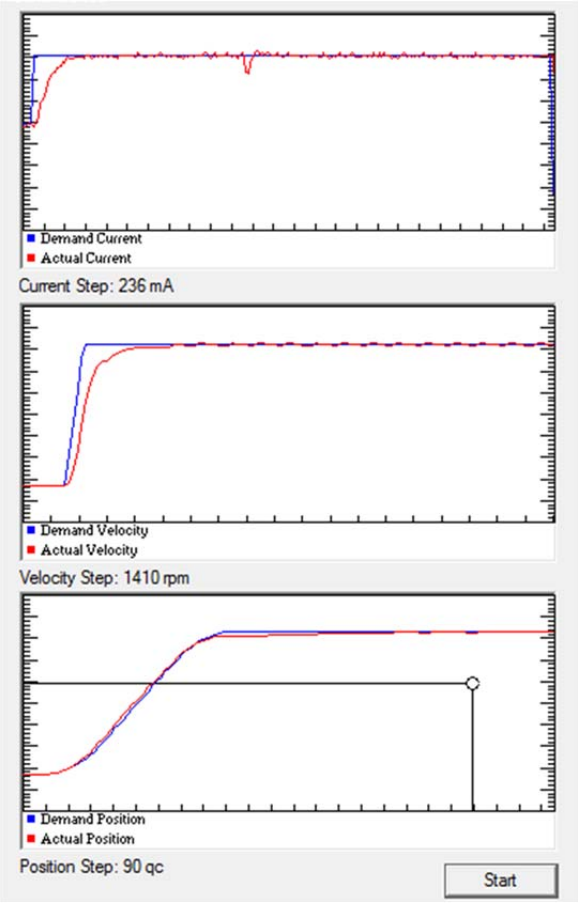

Figure 76. Auto tuning results

Parameter	Current Regulation Values	Velocity Regulation Values	Position Regulation Values
Proportional Gain	510	1537	123
Integral Gain	0	82	132
Derivative Gain	0	0	589
Velocity Feed Forward Factor	0	1944	1944
Acceleration Feed Forward Factor	0	650	650

Table 22. Motor controller gains

Once the motor controller gains were saved and implemented onto the motor position controller hardware, the momentum wheel assembly velocity testing was carried out by increasing the velocity of the momentum wheel in increments of 250 rpm. At each increment, the Maxon motor current consumption and the acceleration of the momentum wheel assembly were collected. The testing continued until the motor speed could no longer be increased. The motor has a published no load speed of 6,500 rpm, but the addition of the momentum wheel to the motor reduced the maximum operating speed of the momentum wheel assembly to 5,000 rpm.

The motor current consumption defines power requirement of the momentum wheel and the amount of time that the two batteries R-SAT can support the operation of the momentum wheel assembly. Each of the batteries is rated for 12 ampere-hours each. Since they are connected in a series to provide a bus voltage of 24 volts, the capacity of the system is 12 ampere-hours (see Figure 77).

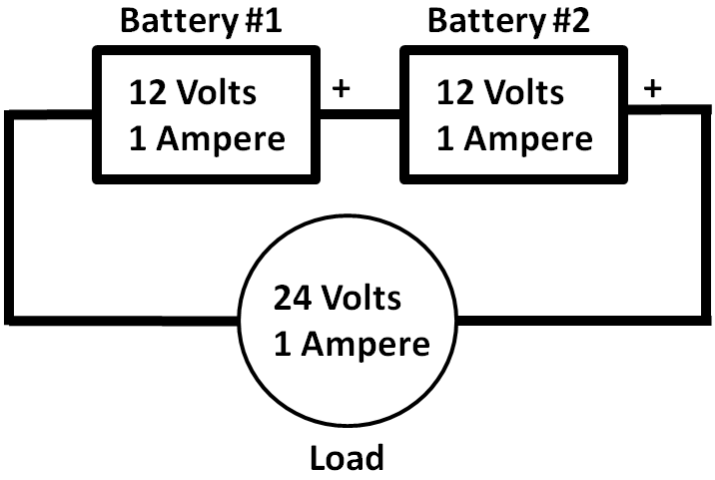

Figure 77. Batteries in a series (After [81])

The amount of current consumed as a function of momentum wheel speed is shown in Figure 77.

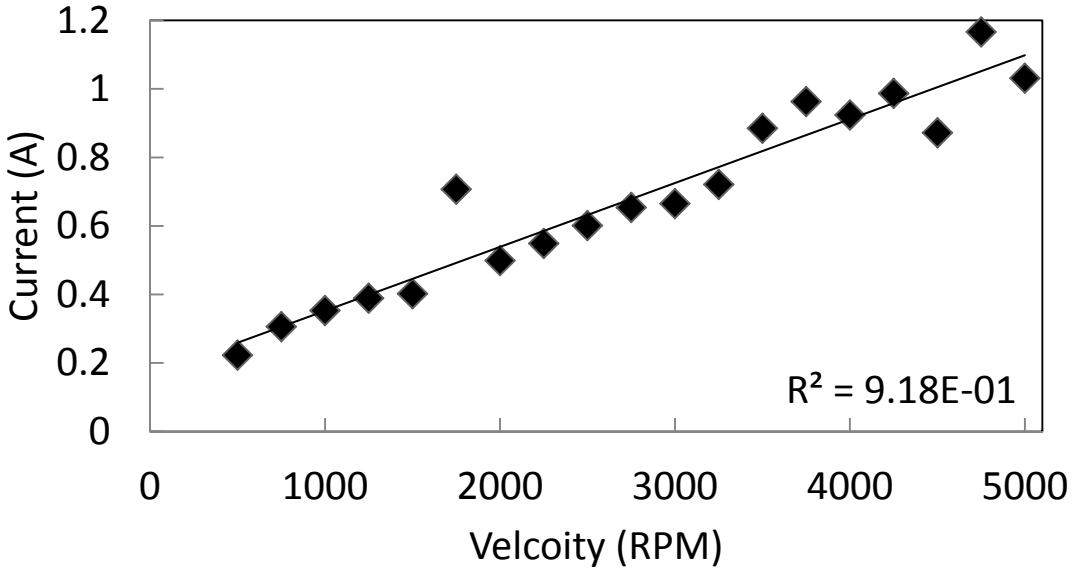

Figure 78. Current consumption as a function of momentum wheel speed

Figure 77 shows that the test results create a linear regression trend line whose equation is given by:

$$I = 1.86x10^{-4}\omega + 1.66x10^{-1} \tag{6.1}$$

where I is the current of the power supply (or battery) and ω is the angular velocity of the momentum wheel. The coefficient of determination or R^2 is a measure of how well the data fits the trend line and is generally measured on a scale of 0 to 1.0, where 1.0 is a perfect match [82]. Since the R^2 value shown in Figure 77 is 0.92, which indicates that the data points fit the tread line well, Equation (6.1) accurately represents the behavior of the fully loaded Maxon motor and can be used to analyze the current consumption at varying momentum wheel speeds. At a constant momentum wheel speed of 5,000 rpm, Equation (6.1) indicates that the drive motor requires about 1.17 amps of current (28 Watts of power at 24 Volts). Therefore, the R-SAT onboard power supply must supply about 120 Watts for running four of the newly designed momentum wheel assemblies. Assuming that maintaining the wheel momentum takes about 30% of the available power (400 Watts), the simulator can be ran for about 1 hour and 20 minutes.

Acceleration measurements of the momentum wheel assembly were used to analyze the unbalance force generated on the assembly as a function of momentum wheel

speed. This ultimately is used to verify that the momentum wheel is balanced to G 1.0. Since the maximum operating speed is now reduced to 5,000 rpm, the allowable permissible unbalance shown in the previous chapter has changed somewhat. The allowable permissible unbalance for the rotor assembly at G 1.0 was calculated using Equation (5.1) and was found to be 0.273 gram-inches. The allowable permissible unbalance amount for 500 rpm and 2,500 was also calculated using Equation (5.1) and was found to be 2.73 gram-inches and 0.546 gram-inches, respectively. The acceleration magnitude of the momentum wheel assembly as a function of time is shown in Figure 79.

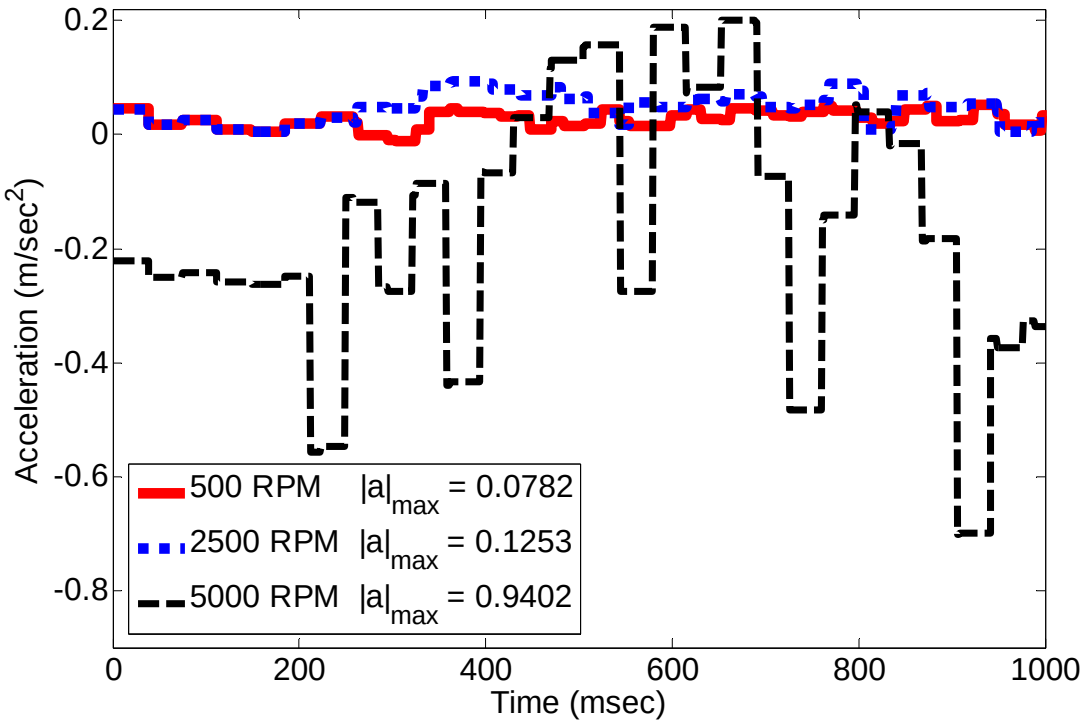

Figure 79. Measured acceleration magnitude as a function of momentum wheel speed

The unbalance force caused by the accelerations in Figure 79 was calculated by using a modified version of Equation (3.1)

$$F_{unbalance} = a_{unbalance} m_{rotor} \tag{6.2}$$

where $a_{unbalance}$ is the measured unbalance acceleration magnitude and m_{rotor} is the mass of the rotor assembly (3.39 kg). Figure 80 shows the unbalance force for the momentum wheel assembly as a function of momentum wheel speed.

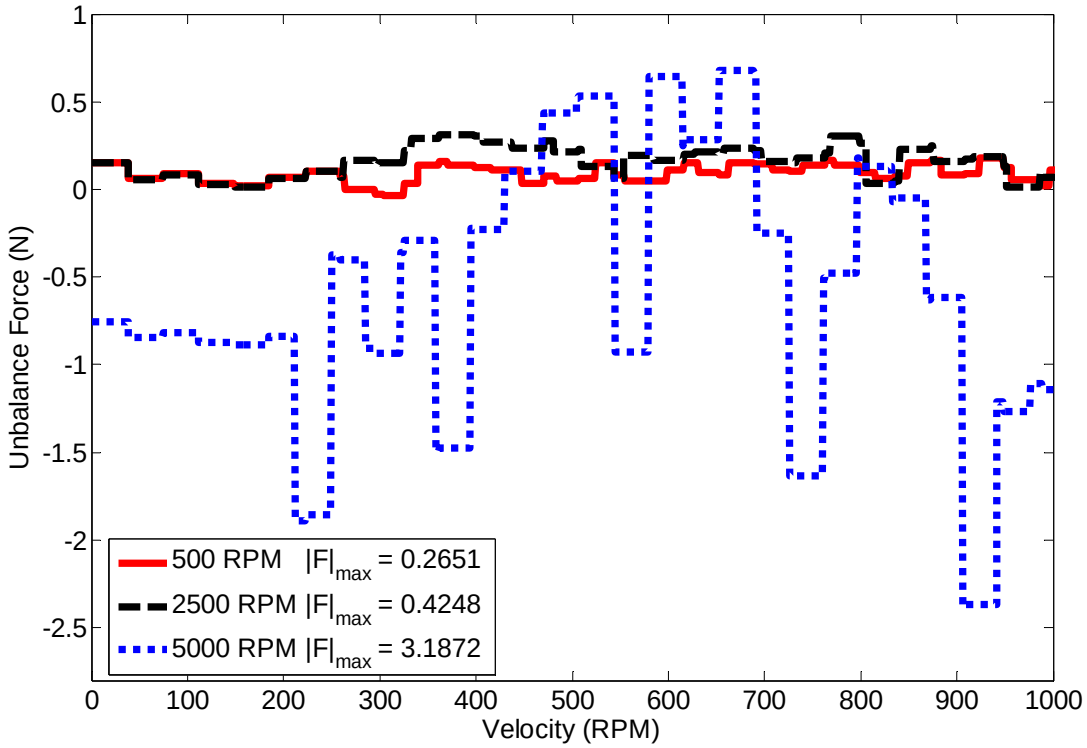

Figure 80. Unbalance force as a function of momentum wheel speed

The computed unbalance force was then used to calculate the unbalance amount for the momentum wheel assembly as a function of momentum wheel by using Equation (5.2) and the results are shown in Figure 81 through Figure 84. Figure 81 through Figure 84 verifies that the momentum wheel assembly unbalance amount at all three momentum wheel velocities are below the calculated allowable permissible unbalance amount. Therefore, the results of this test verified that show the momentum wheel assembly is within the ISO 1940–1 balance quality grade G 1.0.

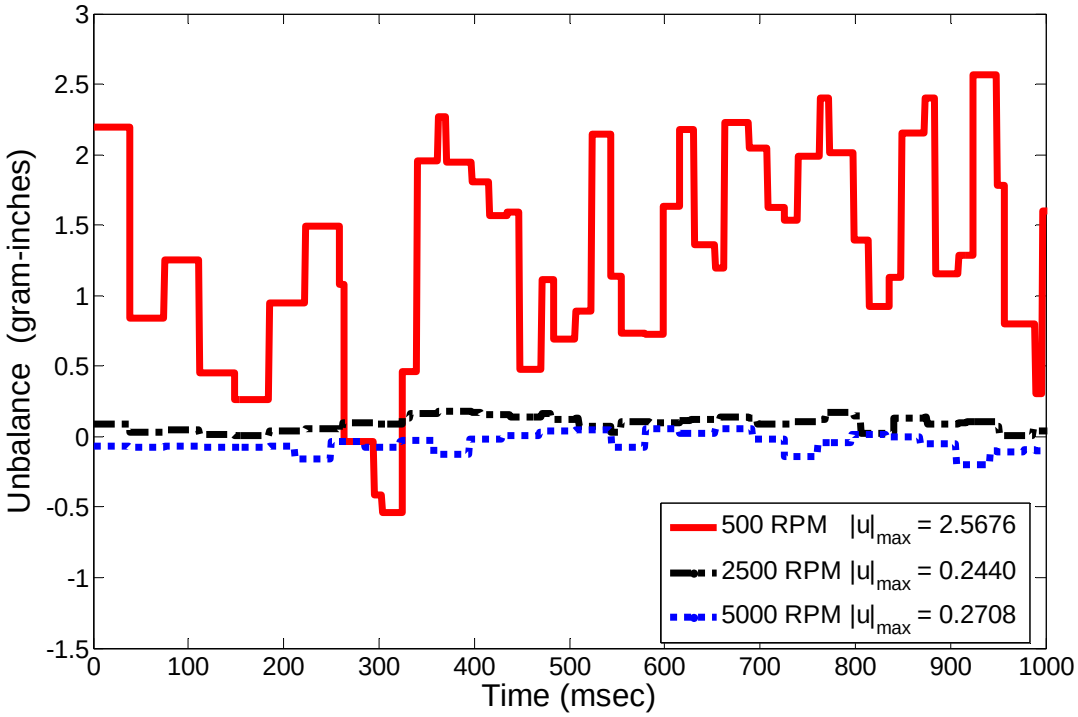

Figure 81. Computed unbalance amount as a function of time

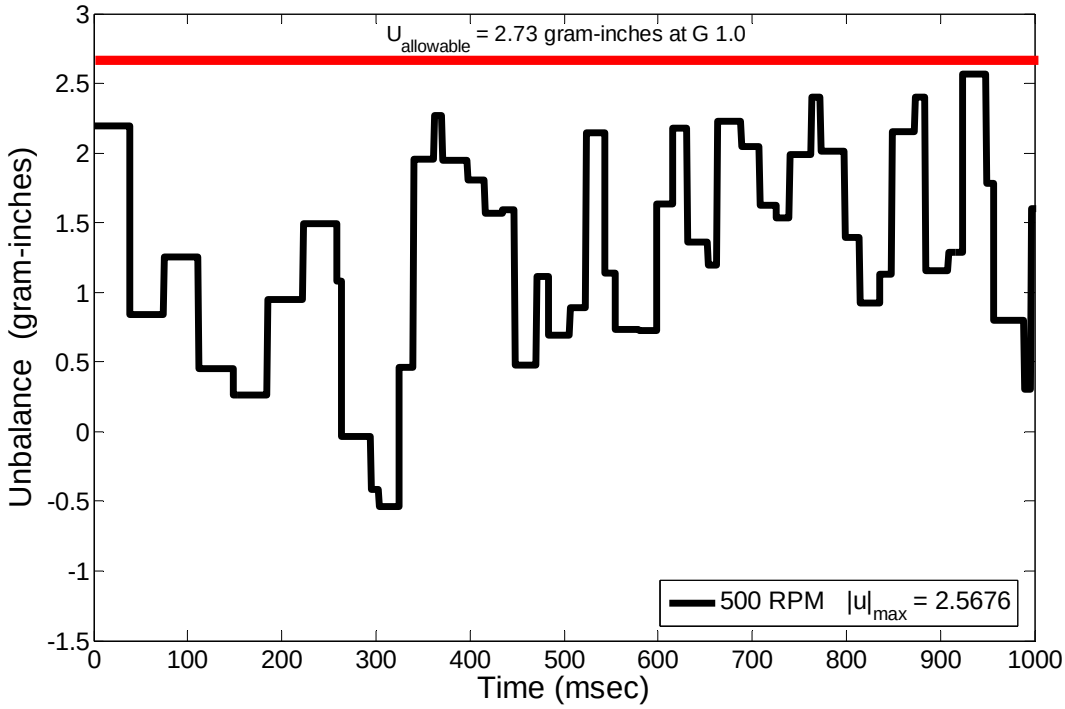

Figure 82. Computed unbalance amount as a function of time at 500 rpm

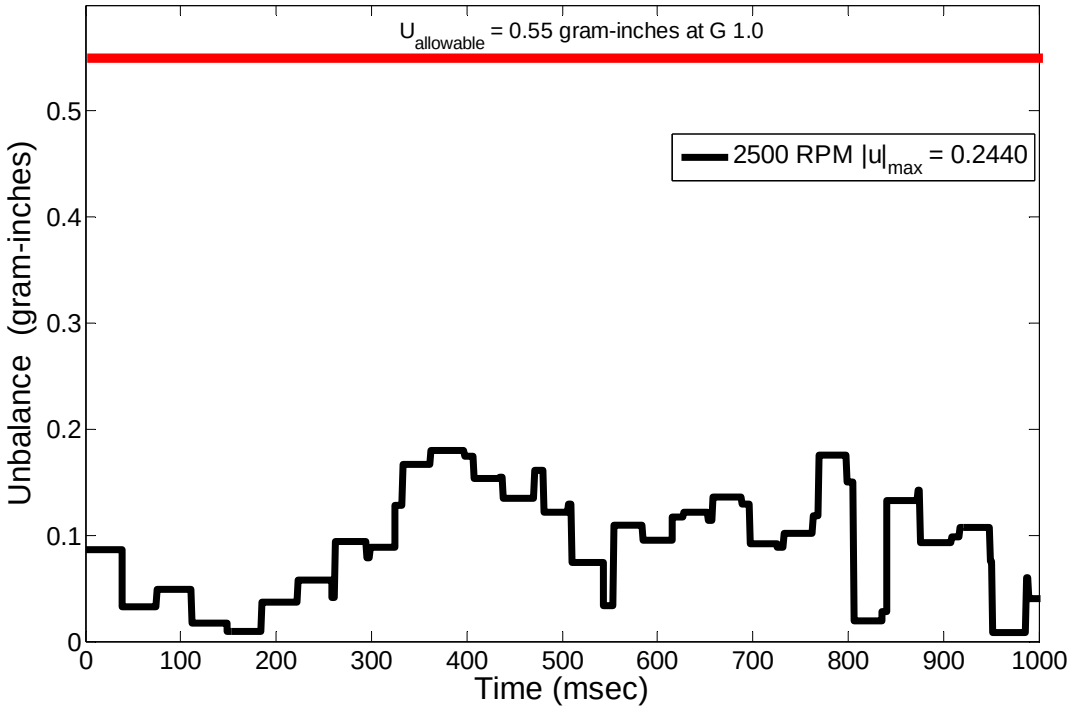

Figure 83. Computed unbalance amount as a function of time at 2,500 rpm

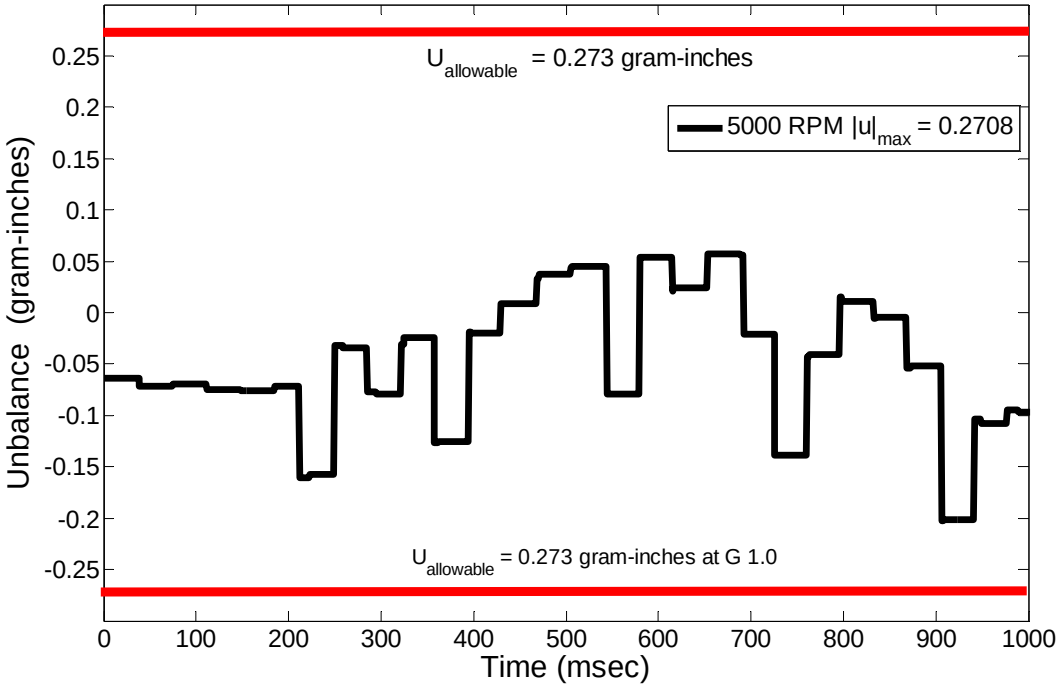

Figure 84. Computed unbalance amount as a function of time at 5,000 rpm

VII. CONCLUSION, CHALLENEGES AND FUTURE WORK

A. CONCLUSION

This thesis contributed to the development of the next generation R-SAT attitude control system by designing and building an open-architecture momentum wheel assembly which is fully interoperable with the current Andrew's Space gimbal mount. The momentum wheel assembly was successfully designed, manufactured and initial testing was successful. The performance parameters for the prototype momentum wheel assembly are shown in Table 23.

Parameter	Unit	Value
Maximum Angular Velocity with Fully Loaded Motor	rpm	5,000
Maximum Angular Velocity with Fully Loaded Motor	rad/sec	523.6
MOI Rotor Assembly	$kg \cdot m^2$	0.0105
Maximum Rotor Assembly Angular Momentum	N·m·sec	5.5
Mass of the Momentum Wheel Assembly	kg	8.63
Computed Unbalance Force at ISO 1940–1 G 1.0	gram-inches	0.2708

Table 23. Prototype momentum wheel assembly performance parameters

B. CHALLENEGES

The first challenge was to learn about each of the momentum wheel assembly components. It took at least three quarters, thousands of hours of research and conducting trade studies before the initial design process was started. By far one of the most challenges aspects of this project was understanding the complex relationship between all of the momentum wheel assembly components. It took a total of 13 design iterations before an acceptable solution. It wasn't until the first meeting with the machinists at Inter-City Manufacturing that the author truly began to see the expertise, knowledge and experience it really takes to manufacture precision components (of any kind). In addition

to the design challenges, there were also challenges when the author was analyzing the effects of backlash on the momentum wheel assembly. After conducting the backlash research (for almost three months), it is clear to the author that an entire thesis can be conducted on examining how backlash effects mechanical systems.

C. FUTURE WORK

Once the next generation R-SAT is complete it will be an invaluable resource for researchers at the Naval Postgraduate School. The newly designed open-architecture momentum wheel assembly prototype system is complete, but there is still a lot of research and work that needs to be done before the simulator is fully mission capable and can be utilized for research. Although the momentum wheel assembly is fully interoperable with the Andrew's Space gimbal mount, the ultimate goal is to have a complete open-architecture CMG system. This system would include a new open-architecture gimbal mount, open-architecture software and control laws and open-architecture electronics. Therefore, the following future work is recommended in order to complete the next generation open- architecture R-SAT:

1. Designing and build an open-architecture gimbal mount. This project will have a lot of the same challenges that were experienced during this thesis work. It is recommended that this project start by examining the current gimbal solution, speaking with the machinists at Inter-City for incite on manufacturing and learn how to conduct a finite element analysis using a CAD modeling tool.

2. Integrate the momentum wheel assembly with the newly design gimbal mount. This project will require some knowledge of electrical engineering, writing control algorithms and will involve hardware testing. It is recommended that this project start by conducting research on how motor controllers work and how they communicate with tools such as Matlab and Simulink. (A semester project title "Design a demo experimental setup for human augmentation" by Mike Rinderknecht is a good example of how to communicate with the Maxon motor controller using Matlab.)

3. Test and analyze the CMGs performance. This will require knowledge of spacecraft CMG control and will be done mostly in the lab. Therefore, most of the work for this project cannot be conducted off campus.
4. Develop and build a electronics board and design software to control the CMG. This project will require extensive knowledge of electrical engineering, software programing and knowledge of spacecraft CMG control. This project may require more time than other project due to the time required to design, build and integrate with the board with the COTS components. It is recommended that this project be split between multiple researchers in order to complete within a reasonable amount of time.
5. Integrate and test the CMG with the R-SAT. This project is much like the testing of the CMGs performance and will require knowledge of spacecraft CMG control. This will also requires knowledge of how the current R-SAT is configurable and how it operates.

THIS PAGE INTENTIONALLY LEFT BLANK

LIST OF REFERENCES

[1] E. M. Emme, "Aeronautics and astronautics: An American chronology of science and technology in the exploration of space, 1915–1960," National Aeronautics and Space Administration, Washington, D.C., Tech. Rep. NASA-TM-80521, Dec. 1961.

[2] R. E. Bourdeau, J. L. Donley and E. C. Whipple. The ionosphere direct measurements satellite instrumentation explorer VIII. Goddard Space Flight Center. MD. Jan. 1961.

[3] L. A. Frank, B. J. O'Brien, J. A. Van Allen and C. D. Laughlin. Absolute electron intensities in the earth's outer radiation zone. *Journal of Geophysical Research 67(1),* pp. 397–403. 1962.

[4] P. J. Coleman, D. L. Judge, E. J. Smith and C. P. Sonett. Characteristics of extraterrestrial ring current system observed by explorer VI and pioneer V satellites. National Aeronautics and Space Administration. Washington, D.C. Apr. 1960.

[5] H. A. Cohen, R. E. Coon and C. L. Hemenway, "Collection and analysis of micrometeorites," National Aeronautics and Space Administration, New York, Tech. Rep. 19620000876, Jan. 1961.

[6] Y. D. Kalinin. Magnetic and ionospheric disturbances: Collected articles pertaining to sections 3 and 5 of the IGY program (geomagnetism and earth currents, ionosphere). National Aeronautics and Space Administration. Washington, D.C. Jan. 1961.

[7] K. L. Bedingfield, R. Leach and M. B. Alexander. Spacecraft system failures and anomalies attributed to the natural space environment. National Aeronautics and Space Administration. AL. Aug. 1996.

[8] J. Wertz and W. Larson. *Space Mission Analysis and Design* (Third Edition ed.) 1999.

[9] M. L. Psiaki. Magnetic torquer attitude control via asymptotic periodic linear quadratic regulation. *Journal of Guidance, Control, and Dynamics 24(2),* pp. 386–394. March-April 2001.

[10] G. P. Sutton and O. Biblarz. *Rocket Propulsion Elements* (Eighth ed.) 2010.

[11] J. R. Wertz, Ed., *Spacecraft Attitude Determination and Control.* Dordrecht, The Netherlands: Kluwer Academic Publishers, 1978.

[12] B. J. O'Connor and L. A. Morine. A description of the CMG and its application to space vehicle control. Presented at AIAA Guidance, Control and Flight Dynamics Conference. Aug. 1967.

[13] G. F. Auclair and R. C. Wells. Control moment gyro selection and design criteria. Presented at AIAA Guidance, Control and Flight Mechanics Conference. 1970.

[14] V. Lappas and B. Wie. Robust CMG steering logic with gimbal angle constraints. Presented at AIAA/AAS Astrodynamics Specialist Conference and Exhibit. 2006.

[15] V. Lappas, W. Steyn and C. Underwood. Design and testing of a control moment gyroscope cluster for small satellites. *Journal of Spacecraft Rockets 42(4),* pp. 729–739. 2005.

[16] C. J. Heiberg. A practical approach to modeling single-gimbal control momentum gyroscopes in agile spacecraft. Presented at AIAA Guidance, Navigation, and Control Conference and Exhibit. 2000.

[17] A. Jacot and D. Liska. Control moment gyros in attitude control. *Journal of Spacecraft Rockets 3*pp. 1313–1320. 1966.

[18] H. F. Kennel, "A control law for double-gimbaled control moment gyros used for space vehicle attitude control," George C. Marshall Space Flight Center, Marshall Space Flight Center, Alabama, Tech. Rep. TM-X-64536, August 7. 1970.

[19] A. D. Jacot and D. J. Liska. Control moment gyros in attitude control. Presented at AIAA Second Annual Meeting. Jul. 1965.

[20] C. R. Keckler and R. G. Kyle. Description of a real-time digital full-scale CMG control system simulation for manned spacecraft. Presented at AIAA Aerospace Computer Systems Conference. 1969.

[21] R. G. Kyle. Optimal feedback control for nonlinear control moment gyro systems (optimal feedback control for nonlinear control moment gyro for Apollo telescope mount) [Ph.D. thesis - Virginia univ.]. *United States* pp. 119P-119P. 1969. Available: http://search.proquest.com/docview/22802828?accountid=12702.

[22] D. W. Sutherlin, J. S. Boland and M. T. Borelli. Attitude control of an orbiting space vehicle (gimbaled control moment gyro for Skylab telescope mount stringent pointing requirements, investigating normal and clamped operation modes and dynamic response of attitude control). *Journal of Spacecraft and Rockets 8*pp. 1165–1167. 1971.

[23] C. S. Rybak, S. I. Lieberman, L. L. Hartter, R. L. Gregory, A. K. Nakashima and R. F. Kaczynski, "Achieving ultrahigh accuracy with a body pointing CMG/RW control system," in *AIAA Guidance and Control Conference,* Key Biscayne, Florida, 1973.

[24] N. A. Osborne, “Fine-pointing improvement by augmentation methods,” in *AIAA Guidance and Control Conference,* Key Biscayne, Florida, 1973, .

[25] S. P. Liden, “Precision CMG control for high-accuracy pointing,” in *AIAA Guidance and Control Conference,* Key Biscayne, Florida, 1973.

[26] J. M. Kolvek, “Final summary report advanced control moment gyro development,” Bendix Corporation, Teterboro, New Jersey, Tech. Rep. NASA-CR-120567, 1974.

[27] B. K. Colburn and L. R. White, “Computation and sensitivity considerations of the ricatti equation in spacecraft CMG steering laws,” in *AIAA 14th Aerospace Sciences Meeting,* Washington, D.C., 1976.

[28] L. R. Bishop, R. H. Bishop and K. L. Lindsay. Proposed CMG momentum management scheme for space station. *Journal of Guidance, Control and Dynamics* pp. 1229–1236. 1987.

[29] L. Cook, P. Golley, H. Krome, J. Blondin, C. Gurrisi and J. Kolvek. Design, fabrication and test of a prototype double gimbal control moment gyroscope for NASA space station. Presented at Annual Rocky Mountain Guidance and Control Conference. 1989.

[30] K. Kito, H. Kanki and S. Ishii. Concept design and performance test of a magnetically suspended single- gimbal control moment gyro. *Guidance and Control 1989: Proceedings of the Annual Rocky Mountain Guidance and Control Conference, Keystone, CO; UNITED STATES; 4–8 Feb.1989* pp. 25–30. 1989.

[31] L. Yang, M. M. Mikulas, K. C. Park and R. Su. Slewing maneuvers and vibration control of space structures by feedforward/feedback moment-gyro controls. *AIAA/ASME/ASCE/AHS/ASC Structures, Structural Dynamics, and Materials Conference, 34th and AIAA/ASME Adaptive Structures Forum, La Jolla, CA; UNITED STATES; 19–22 Apr.1993* pp. 3448–3456. 1993.

[32] C. J. Heiberg, D. Bailey and B. Wie. Precision pointing control of agile spacecraft using single gimbal control moment gyroscopes. *American Institute of Aeronautics and Astronautics, Inc.* pp. 1620. 1997.

[33] H. Kurokawa. Survey of theory and steering laws of single-gimbal control moment gyros. *Journal of Guidance, Control, and Dynamics 30(5),* pp. 1331–1340. 2007.

[34] L. Winder and S. Trundle, “3-DOF Satellite Simulator User’s Guide,” *Andrew’s Space,* 2009.

[35] S. Pizzica. Open systems architecture solutions for military avionics testing. *IEEE Aerospace and Electronic Systems Magazine. 16(8),* pp. 4–9. 2001.

[36] B. Wie, *Space Vechicle Dynamics and Control.* Reston, VA: American Institute of Aeronautics and Astronautics, Inc., 1998.

[37] R. A. Campbell. Performance of twin gyro attitude control system including passive compensation and nonlinear control law. Nation Aeronautics and Space Administration. Washington, D.C. 1970.

[38] R. Smith and S. D. Eppinger, "Identifying controlling features of engineering design iteration," *Management Science,* vol. 43, pp. 276–293, 1997.

[39] Allied Motion. (2012, December 4) *Quantum NEMA 17 brushless servo motors* [Online]. Available: http://www.alliedmotion.com/Products/Series.aspx?s=42.

[40] Orientalmotor. (2012, December 4). *Basics of motion control* [Online]. Available: http://www.orientalmotor.com/technology/articles/AC-brushless-brushed-motors.html.

[41] W. Brown, "Brushless DC Motor Control Made Easy, Application Note AN857," *Microchip Technology INC.,* 2002.

[42] P. Pillay and R. Krishnan, "Application Characteristics of Permanent Magnet Synchronous and Brushless DC Motors for Servo Drives," *IEEE Transaction on Industry Applications,* vol. 27, pp. 986–996, 1991.

[43] Anaheim Automation. (2012, December 4). *Brush DC Motor Guide* [Online]. Available: http://www.anaheimautomation.com/manuals/forms/brush-dc-motor-guide.php.

[44] P. Alaeinovin, S. Chiniforoosh and J. Jatskevich, "Evaluating misalignment of hall sensors in brushless DC motors," in *IEEE Electrical Power & Energy Conference,* Vancouver, Canada, Oct. 2008.

[45] Clemson University Vehicular Electronics Laboratory (CVEL) Automotive Electronics. (2012, December 4) *Brushed DC Motor* [Online]. Available: http://www.cvel.clemson.edu/auto/actuators/motors-dc-brushed.html.

[46] ASLM INC. (2012, December 4) *Rotary motors-radial* [Online]. Available: http://www.pmmotor.com/RotaryMotorsRadial.aspx.

[47] Danaher Motion, "RBE (H) Series Motor Data Publication,"*[Technical Manual],* 2003.

[48] G. Metta, D. Vernon, L. Natale, F. Nori and G. Sandini, "The iCub humanoid robot: An open platform for research in embodied cognition," in *IEEE Workshop on Performance Metrics for Intelligent Systems,* Washington, 2008.

[49] X. Xie, “Comparison of Bearings: For the Bearing Choosing of High-speed Spindle Design,” *Technical Report from Department of Mechanical Engineering, University of Utah,* 2003.

[50] McMaster-Carr. (2012, December 4). *McMaster-Carr Technical Drawing* [Online]. Available: http://www.mcmaster.com/#cadinlnord/1434k6/=k700qt.

[51] Koyo Corporation, “Koyo Ball Roller Bearings,” *Koyo Corporation [Technical Manual and Catalog],* 2006.

[52] The Timken Company, “Timken Super Precision Bearings for Machine Tool Applications,” *[Technical Manual],* 2009.

[53] Globalspec. (2012, December 4). *Ball Bearing Information* [Online]. Available: http://beta.globalspec.com/learnmore/mechanical_components/bearings_bushings/ball_bearings_all_types.

[54] J. Lieblein and M. Zelen, “Statistical Investigation of the Fatigue Life of Deep-Groove Ball Bearings,” *Journal of Research of the National Bureau of Standards,* vol. 57, pp. 273–316, November 1956.

[55] Koyo Corporation, “Training Manual,” *Koyo Corporation [Technical Manual],* 2008.

[56] Globalspec. (2012, December 4). *Needle Roller Bearings Information* [Online]. Available: http://beta.globalspec.com/learnmore/mechanical_components/bearings_bushings/needle_roller_bearings.

[57] MRC Bearing Services, “Engineering Handbook,” *[Technical Manual],* 2005.

[58] D. V. Griffiths, F. A. Gordon and N. Manoharan, “Bearing capacity of rough rigid strip footing on cohesive soil: probabilistic study,” *Journal of Geotechnical and Geoenvirnmental Engineering,* vol. 128, pp. 743–755, 2002.

[59] S. Freeder, “Andrews Space CMG wheel assembly shop drawing,” *[Technical Manual],* March 6, 2009.

[60] MatWeb LLC. (2012, December 4). *Material property data: 304 stainless steel* [Online]. Available: http://www.matweb.com/search/DataSheet.aspx?MatGUID=abc4415b0f8b490387e3c922237098da.

[61] G. W. Michalec, *Precision Gearing: Theory and Practice.* New York: John Wiley & Sons, Inc., 1966.

[62] J. A. Cascio, “Optimal path planning for multi-arm, multi-link robotic manipulator.” *M.S.C, Monterey, California Naval Postgraduate School,* 2008.

[63] I. M. Ross, “A beginner’s guide to DIDO: a MATLAB application package for solving optimal control problems,” *Elissar, LLC,* 2007.

[64] I. M. Ross, *A Primer on Pontryagin’s Principle in Optimal Control.* San Francisco: Collegiate Publishers, 2009.

[65] MatWeb LLC.(2012, December 4). *Material property data: Aluminum 6061* [Online]. Available: http://www.matweb.com/search/DataSheet.aspx?MatGUID=626ec8cdca604f1994be4fc2bc6f7f63&ckck=1.

[66] S. Freeder, “Andrews Space CMG assembly shop drawing,” *[Technical Manual],* September 4, 2008.

[67] Harmonic Drive LLC, “Cup type component sets & housed units: CSF & CSG series,” *[Technical Manual],* 2012.

[68] Harmonic Drive LLC, “Precision actuators, gearheads, and gearing components,” *[Technical Manual],* 2012.

[69] M. Nordin and P. Gutman. Controlling mechanical systems with backlash—a survey. *Automatica 38(10),* pp. 1633–1649. 2002.

[70] K. C. Craig and R. C. Greenheck, “Control-oriented modeling for backlash,” *Mechatronic in Design,* August 25, 2011.

[71] Allied Motion, “CP-500 series housed rotary optical encoder,” *[Technical Manual],* 2012.

[72] Anonymous. (2012, January 18). Absolute linear encoder boosts throughput, yields. [Online]. Available: http://www.mmsonline.com/products/absolute-linear-encoder-boosts-throughput-yields.

[73] Dynapar, “Series AI25: BiSS absolute encoder,” *[Technical Manual],* 2010.

[74] MOOG, “Slip rings with through-bores: SRA-73683,” *[Technical Manual],* 2012.

[75] H. P. Bloch, *Improving Machinery Reliability: Practical Machinery Management for Process Plants.* Houston, TX: Gulf Professional Publishing, 1998.

[76] V. D. Poornima, S. Adinarayana and B. V. Appa Rao, “Two plane balancing of a conical rotor driven by vertical belt system designed to reduce gyro effect,” *International Journal of Mechanical Engineering and Robotics Research,* vol. 1, October, 2012.

[77] A. M. Al-Shurafa, “Determination of balancing quality limits,” *Saudi Electricity Company- Ghazlan Power Plant,* 2003.

[78] International Organization for Standardization, “1940/1-Mechanical vibration: balance quality requirements for rotor in a constant (rigid) state,” *ISO 1940/1,* 2003.

[79] Maxon Motor, “Maxon academy: practical training with the EPOS studio,” *[Technical Manual],* 2010.

[80] Maxon Motor, “EPOS positioning controllers: application notes collection,” *[Technical Manual],* 2012.

[81] W. E. Johns. (2012, December 04) *Notes on batteries* [Online]. Available: http://www.gizmology.net/batteries.htm.

[82] A. C. Cameron and F. A. Windmeijer, “An R-squared measure of goodness of fit for some common nonlinear regression models,” *Journal of Econometrics,* vol. 77, pp. 329–342, 1997.

THIS PAGE INTENTIONALLY LEFT BLANK

INITIAL DISTRIBUTION LIST

1. Defense Technical Information Center
   Ft. Belvoir, Virginia

2. Dudley Knox Library
   Naval Postgraduate School
   Monterey, California

3. Professor I. Mike. Ross
   Naval Postgraduate School
   Monterey, California

4. Mark Karpenko
   Naval Postgraduate School
   Monterey, California

5. Knox T. Millsaps
   Naval Postgraduate School
   Monterey, California

5. Rudolf Panholzer
   Naval Postgraduate School
   Monterey, California